

# REPORT DOCUMENTATION PAGE

AFRL-SR-AR-TR-03-

data needed, and completing and reviewing this collection of information. Send comments regarding this burden estimate or any this burden to Department of Defense, Washington Headquarters Services, Directorate for Information Operations and Reports (0 4302. Respondents should be aware that notwithstanding any other provision of law, no person shall be subject to any penalty for valid OMB control number. PLEASE DO NOT RETURN YOUR FORM TO THE ABOVE ADDRESS.

ning the  
educing  
2202-  
currently

## 1. REPORT DATE (DD-MM-YYYY)

25/05/2002

## 2. REPORT TYPE

Final report

## 3. DATES COVERED (From - To)

01/03/1999-28/02/2002

## 4. TITLE AND SUBTITLE

Photorefractive materials exhibiting high performances and minimal phase separation

## 5a. CONTRACT NUMBER

## 5b. GRANT NUMBER

F49620-99-1-0055

## 5c. PROGRAM ELEMENT NUMBER

## 6. AUTHOR(S)

Professor Luping Yu

## 5d. PROJECT NUMBER

## 5e. TASK NUMBER

2303/cx

## 5f. WORK UNIT NUMBER

## 7. PERFORMING ORGANIZATION NAME(S) AND ADDRESS(ES)

University of Chicago

970 E. 58<sup>th</sup> St  
Chicago, IL 60637

## 8. PERFORMING ORGANIZATION REPORT NUMBER

## 9. SPONSORING / MONITORING AGENCY NAME(S) AND ADDRESS(ES)

AFOSR/NL

801 N. Randolph st Room 732

Arlington VA 22203-1977

Dr. Charles Lee,  
Program Manager

## 10. SPONSOR/MONITOR'S ACRONYM(S)

## 11. SPONSOR/MONITOR'S REPORT NUMBER(S)

## 12. DISTRIBUTION / AVAILABILITY STATEMENT

This document has been approved for public release and sale, its distribution is unlimited.

## 13. SUPPLEMENTARY NOTES

## 14. ABSTRACT

This report summarises the research effort for the grant period as indicated above on multifunctional photorefractive materials. New synthetic approaches and new materials with much improved photorefractive properties have been developed. Detailed discussion and description are described in this report.

20031028 136

## 15. SUBJECT TERMS

## 16. SECURITY CLASSIFICATION OF:

a. REPORT

b. ABSTRACT

c. THIS PAGE

## 17. LIMITATION OF ABSTRACT

## 18. NUMBER OF PAGES

62

## 19a. NAME OF RESPONSIBLE PERSON

Luping Yu

## 19b. TELEPHONE NUMBER (include area code)

773-702-8698

# **Final Technical Report**

To  
**Air Force Office of Scientific Research**

For Year 2002

Grant Number: F49620-99-1-0055

Prepared by

Luping Yu

The University of Chicago  
Department of Chemistry  
5737 S. Ellis Avenue  
Chicago, IL-60637

Phone Number: 773-702-8698

Fax number: 773-702-0805

e-mail address: [lupingyu@midway.uchicago.edu](mailto:lupingyu@midway.uchicago.edu)

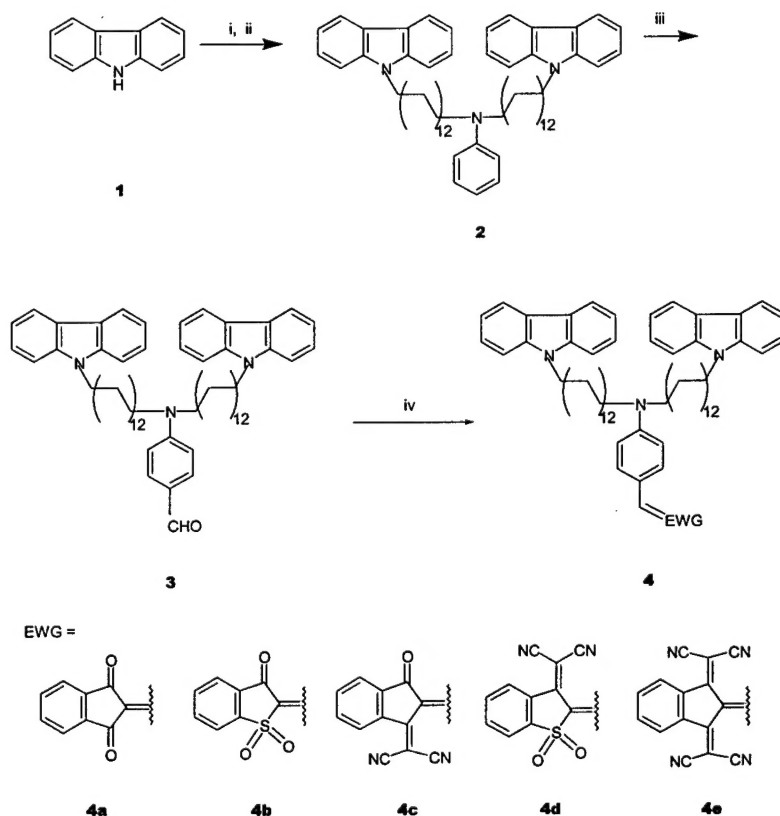
## **DISTRIBUTION STATEMENT A**

Approved for Public Release  
Distribution Unlimited

## A. A New Family of Amorphous Molecular Materials Showing Large Photorefractive Effect.

In recent years, functional molecular materials exhibiting nonlinear optical, electroluminescent, ferromagnetic and photoconducting properties have been sought for practical applications.<sup>1-4</sup> These materials possess excellent processibility, transparency and can be efficiently purified by many well-known techniques such as chromatography. The versatility of structural modification offers a unique opportunity to meet additional challenges, for example, designing multifunctional materials that could simultaneously possess several properties. Photorefractive (PR) materials are such multifunctional materials that combine photoconductivity and nonlinear optical (NLO) response to modulate the refractive index of the medium.<sup>5</sup> Due to their potential applications in holographic optical data storage and real-time optical processing, various classes of organic PR materials including polymers,<sup>6-8</sup> liquid crystals<sup>9</sup> and organic glasses<sup>10,11</sup> have been explored. Herein, we report a novel series of amorphous molecular materials based on carbazole and methine dyes, which exhibit very interesting charge-transfer complex formation and large PR responses.

The synthetic route is shown in Scheme 1, where carbazole was chosen as the photoconductive component for hole transport. Condensation of aldehyde **3** with electron withdrawing groups yielded methine dye as the NLO chromophores. The molecules synthesized (compound **4**) thus possess dual functions: photoconductivity and second-order NLO activity. The long aliphatic chain was introduced to prevent the materials



Scheme 1. Synthesis of multifunctional molecular materials containing carbazole and methine dye. Reagents and conditions: i,  $\text{Br}(\text{CH}_2)_{12}\text{Br}$ ,  $\text{NaH}$ ; ii, aniline,  $\text{K}_2\text{CO}_3$ ; iii,  $\text{POCl}_3$ , DMF; iv, EWG, ethanol.

from crystallization and help resulting compounds remain amorphous at room temperature. The thermal properties of the compounds are summarized in Table 1, which indicated the low  $T_g$  nature of the materials. These compounds were found to readily form amorphous films, as evidenced by differential scanning calorimetry (DSC), polarizing microscopy and x-ray diffraction. The amorphous films made from these compounds are very stable in an ambient atmosphere for over a year up to the present time and no crystallization phenomenon was observed even on further heating. The UV/vis spectra of compound **4** in  $\text{CH}_2\text{Cl}_2$  display two intense bands. The one at around 347 nm can be attributed to carbazole moiety, while the other one is due to the NLO chromophore. As also shown in Table 1, increasing acceptor strength by replacing carbonyl groups with sulfonyl and dicyanovinyl groups results in bathochromic shift in corresponding chromophores. It is interesting to note that in solid UV/vis spectra, new long-wavelength absorption bands were observed in addition to the peaks from chromophore and carbazole. The intensity of these new peaks varies as a function of temperature. As the temperature increases, the absorbance decreases and finally becomes zero at around 75 °C. These new bands were assigned to the formation of charge-transfer complexes (CTC) between the carbazole and electron withdrawing groups because it was observed that when compound **2** was mixed with electron acceptors in  $\text{CH}_2\text{Cl}_2$  solution, an intense coloration with new long-wavelength absorption peaks developed immediately. These new absorption bands enable us to photoexcite the materials mainly through charge-transfer complex at longer wavelength, while the absorption from the NLO chromophore could be minimized. It is worth mentioning that additional photosensitizer, such as 2,4,7-trinitro-9-fluorenone (TNF), are needed in most of reported composite PR materials containing carbazole moiety.<sup>12</sup> System reported here shows all necessary functions for PR response in a single molecules.

Table 1. The properties of carbazole containing amorphous molecules.

Compound	$T_g/^{\circ}\text{C}^{\text{a}}$	$T_d/^{\circ}\text{C}^{\text{a}}$	$\lambda_{\text{max}}/\text{nm}^{\text{b}}$	$\epsilon_{\text{max}}/\text{l mol}^{-1}\text{cm}^{-1\text{b}}$
4a	9	292	491	48,900
4b	10	282	492	59,100
4c	13	211	570	49,000
4d	7	228	602	59,300
4e	6	205	628	18,300

a) The glass transition temperature ( $T_g$ ) and the decomposition temperature ( $T_d$ ) were Determined by DSC, 10  $^{\circ}\text{C}/\text{min}$ . b) Measured in  $\text{CH}_2\text{Cl}_2$  solution.

Photocurrent measurements indicated these materials are photoconductive and second harmonic generation signal was observed as a function of an external field. The PR nature of these molecular materials was verified in two-beam coupling measurement. In this experiment, two coherent laser beams ( $p$ -polarized) intersect inside of the sample to write a holographic grating. It is known that this grating has a non-zero phase shift

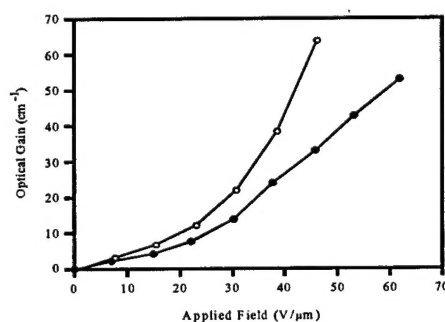


Figure 1. Photorefractive optical gain of compound 4b (o) and compound 4c (o) as a function of the applied field.

with respect to the light intensity pattern. An asymmetric energy exchange between the two beams, characterized by the two-beam coupling gain coefficient,  $\Gamma$ , can be observed.<sup>5</sup> A further note is that in this experiment, the normal of the sample surface needs to be tilted  $52^{\circ}\text{C}$  to yield a projection of grating wave vector along the poling axis. The films for PR characterization were prepared by sandwiching the melt of compounds between two glass substrates coated with indium-tin oxide. The thickness of films is about 128  $\mu\text{m}$  maintained by a polyimide spacer. Some preliminary results performed on compound 4b and 4c are presented in Figure 2. Compound 4b was measured with a He-Ne laser (632.8 nm), while compound 4c was excited by a diode laser with a wavelength of 780 nm. As the applied field increases, the intensity of one beam increased, while that of the second beam decreased. When the electric field was turned off, the intensities returned to their origin levels and no energy exchange was observed. The strong field dependence of the optical gain reflects the field dependence of both quantum yield of photogeneration of charge carriers and second-order NLO response. For compound 4b, at a field of 46  $\text{V}/\mu\text{m}$ , an optical gain value of  $65.4\text{ cm}^{-1}$  was achieved. The absorption coefficient of the material was only  $1.4\text{ cm}^{-1}$  thus giving us a net optical gain of  $64\text{ cm}^{-1}$ . For compound 4c, we have obtained a PR gain of  $53\text{ cm}^{-1}$  by applying a field of 62  $\text{V}/\mu\text{m}$ , whereas the absorption coefficient was  $4.3\text{ cm}^{-1}$ . The index grating recorded in the material were further tested by a weaker, counter-propagating probe beam ( $p$ -polarized) in the four wave mixing experiments. The diffraction efficiency,  $\eta$ , is calculated as the intensity ratio of the diffracted signal to the probe beam. It was observed that the diffraction efficiency also had a strong dependence on the applied field and reached 17% for compound 4b and 9% for compound 4c at  $E = 42\text{ V}/\mu\text{m}$ .

In summary, a new series of multifunctional amorphous molecules have been synthesized and characterized for photorefractive applications. Selecting different electron acceptor groups affords controls not only in electrooptic effect but also in charge generating characteristics of the resulting materials. This approach opens the way for an extension of PR sensitivity to near-IR or even IR regions, which is very interesting for applications in telecommunication. Moreover, the synthetic flexibility and simplicity of this molecular system offer great possibilities for structural modifications to further improve performance or match the laser wavelength for the application desired. Extensive work based on this system is now under way.

## B. Photorefraction and Complementary Grating Competition in Bipolar Transport Molecular Material

### I. INTRODUCTION



Both organic and inorganic photorefractive materials have been extensively investigated for applications in data storage and real-time information processing.<sup>1-21</sup> Organic photorefractive materials are molecular materials that exhibit weak intermolecular interactions and are typically soft amorphous solids. These characteristics distinguish organic material from inorganic materials in all of the four processes involved in the photorefractive effect. For example, charge carriers are generated through the dissociation of tightly bonded excitons, not via inter-band ionization. The photogenerated carriers are transported away under an electric field via inter-site hopping, thereby experiencing dispersed potential energy. Because of the amorphous and disorderly nature of the transporting molecular network, the depth of the traps in organic materials has a rather dispersed distribution. Furthermore, the electro-optic response is provided by an individual molecular chromophore with an electronic origin.

With the development of new organic photorefractive materials, it is frequently observed that in organic materials the grating build-up and decay does not follow a single exponential function as predicted by the standard model of photorefraction,<sup>22</sup> however, the grating formation and erasure do consist of multiple components with different time constants.<sup>23-27</sup> One of the reasons for this is the existence of a more dispersed distribution of trap levels. Two- or multi-level trap models have been proposed in which photogenerated charge carriers are redistributed in two or more levels, thereby creating superimposed in-phase gratings. Since the trap density, photoexcitation and recombination rates are generally different for each level, each grating should have different exponential time constants for build up and decay. Some phenomena, such as cancellation, revelation of the gratings<sup>28</sup> were observed in a photorefractive polymeric composite, which is composed of 40 wt. % diethylaminobenzaldehyde-diphenyl hydrazone (DEH) dissolved in Bisphenol A 4,4'-nitroaminotolane. A two-trap model with charge exchange between traps was proposed assuming that the first type of trap was highly photosensitive and the second type of trap had low photogeneration efficiencies and collects charges liberated from the first type of trap.<sup>28</sup> The movement of the charge from the first trap to the second one is responsible for the grating revelation and cancellation. The unique quasi-nondestructive reading has been observed in a photorefractive polymeric composite; poly(methyl methacrylate): 1,3-dimethyl-2,2-tetramethylene-5-nitrobenzimidazole: C<sub>60</sub>. The properties were explained by a two trap-level model in which the two levels were populated sequentially. The intensity-dependent decay rate and the transition were qualitatively mimicked.<sup>29</sup> In these models, only one type of the photogenerated carrier (hole) was involved. These special phenomena are the results of the traps' intercommunication. In another study on a photorefractive polymeric composite comprised of a methyl methacrylate copolymer with a side-chain NLO chromophore *p*-nitroaniline doped with 30 wt % DEH,<sup>30</sup> grating competition and revelation was found to be the result of the competition between two gratings with the presence of two types of charges. The primary grating was from the charged carrier hole, while the secondary grating was attributed to residual ionic motion in response to the photorefractive space-charge field.<sup>30</sup>

In this paper, we report a comprehensive investigation of the photorefractive properties of a novel glassy molecular material that exhibits both sizable photorefractive properties and competition between the complementary holographic gratings. To our knowledge, this material is the first organic compound to exhibit complementary gratings formed by simultaneous electron-hole transport, although the phenomenon has been

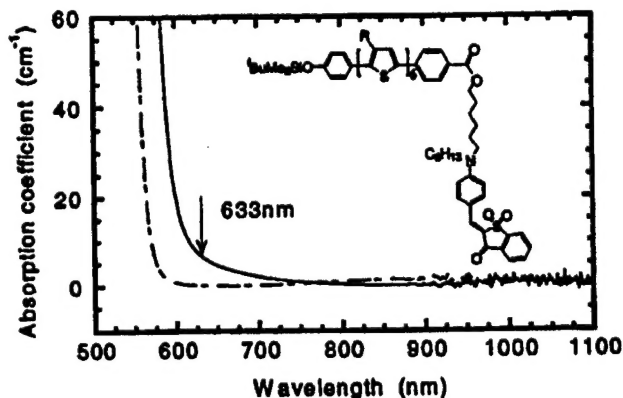


Figure 1 The structure of the photorefractive molecule containing a sexithiophene derivative and a methine dye (inset), and the absorption spectrum in solid state of the photorefractive molecule (solid line) and that of sexithiophene backbone only (dashed line).

extensively studied experimentally<sup>31-36</sup> and theoretically<sup>34,37-40</sup> in inorganic photorefractive crystals.

We will describe the preparation of materials and samples in Section II. Section III characterizes the photorefractive properties, the grating cancellation and revelation behaviors in the recording and erasing processes. Section IV provides evidence for the bipolar transport nature of the material from the mobility measurement in a time-of-flight experiment. In Section V, we propose a possible two-channel two-trap molecular model based on the molecular energy levels deduced from electrochemical measurements and known photorefractive theory. We also discuss the dynamics of complementary grating writing and erasing. Section VI summarizes our understanding of the photorefractive properties of the material.

## (1) MOLECULAR DESIGN AND SAMPLE PREPARATION

The material studied in this paper contains a sexithiophene derivative covalently linked to a nonlinear optical (NLO) chromophore, a methine dye.<sup>41</sup> The molecular structure of this compound is shown in Figure 1 and its redox potentials and band-gap are shown in Table I (Compound 1). The sexithiophene derivative was

introduced to facilitate hole transport. The free charge carriers are generated by the photoexcitation of the methine dye. This is because the molecule exhibits an absorption coefficient of  $6.42 \text{ cm}^{-1}$  at the wavelength of 633 nm with a dominant contribution from the NLO

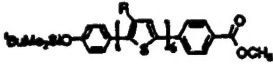
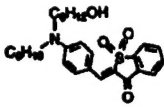
Compound number	Structure	$V_{ox}$ vs SHE (V)	$V_{red}$ vs SHE (V)	$V_{red}-V_{ox}$ ( $-\Delta E_{electrochemical}$ ) (V)	Photoabsorption edge ( $-\Delta E_{optical}$ ) (eV)
1	Photorefractive Molecule (see Figure 1)	1.02 (1.49 <sup>a</sup> )	0.92	1.94 (2.41 <sup>b</sup> )	2.30
2		1.08	—	—	2.48
3		1.43	0.94	2.37	2.30

Table I Structures, redox potentials and band-gaps of the three compounds measured by using electrochemical and photoabsorption methods.

chromophore, while the absorption coefficient of the sexithiophene segment (Compound 2 in Table I) was estimated to be less than  $0.2 \text{ cm}^{-1}$  as shown in Figure 1. Therefore, the methine dye plays multiple roles as a photogenerator, NLO chromophore and an electron transporter. The branched side-chains on the thiophene rings were introduced to prevent the materials from crystallization. The glass transition temperature,  $T_g$ , of the material is  $-3.2^\circ\text{C}$  as measured by differential scanning calorimetry (TA Instruments, Model DSC-10). It is well known that the refractive index modulation of a low  $T_g$  photorefractive material can be enhanced by the orientation of NLO chromophore in response to the space-charge field.<sup>42</sup> The refractive index of the material at 632.8 nm is 1.64 measured with a prism coupler (Metricon, Model 2010).

Samples for the volume holographic recording were prepared by applying a concentrated solution of 1 in chloroform onto two pieces of indium tin oxide (ITO) glass. After drying at  $80\sim 90^\circ\text{C}$  on a hot plate for 20 min, the samples were dried thoroughly in a vacuum oven for 16 hours at  $60\sim 70^\circ\text{C}$ . The two pieces were then pressed together with a polyimide spacer ( $125 \mu\text{m}$ ) to maintain a uniform thickness. Samples for photoconductivity and mobility measurements were prepared by the same procedures except that thinner polyimide spacers ( $25 \mu\text{m}$ ) were used. These films were compressed between either two pieces of ITO glass or one ITO glass and an aluminum plate.

## II. GRATING RECORDING EXPERIMENTS

### A. Experimental Techniques

The grating recording experiments (two-beam coupling and four wave mixing) were conducted by using a radiation of He-Ne laser (Spectra-Physics, Model 127, 632.8 nm). The two grating-writing beams were loosely focused to spots with a diameter of 860

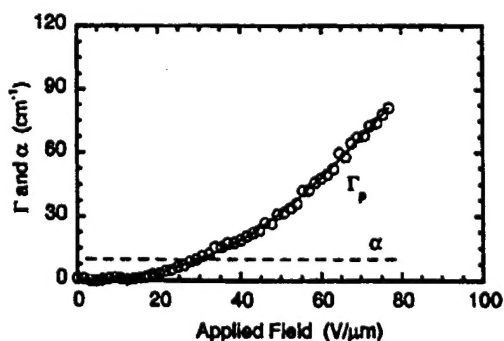


Figure 2 Photorefractive gain coefficient ( $\Gamma_p$ ) as a function of applied field. The solid line is the absorption coefficient at the laser wavelength (632.8 nm).

$\mu\text{m}$  inside of the sample by using a lens of 500mm focus length. In a two-wave-mixing experiment, two  $p$ -polarized laser beams with an equal intensity of  $830 \text{ mW/cm}^2$  were overlapped in the sample to write the index grating. The incident-crossing angle of the beams is  $7.5^\circ$  and the film normal was tilted at an angle of  $53^\circ$  with respect to the symmetric axis of the two writing beams to ensure a nonzero projection of the external field in the direction of the grating vector. The transmitted intensities of both beams were detected using two calibrated photodetectors (Newport, Model 1815-C, Photodiode, 818-SL) and were recorded with a personal computer. The photorefractive gains were calculated by using the expression,  $\Gamma = (1/L) \times \ln[\gamma/(2-\gamma)]$ , where  $L$  is the optical path for the amplified beam and  $\gamma$  is the beam coupling ratio (the ratio of the signal intensities with and without pump beam). The phase shifts of the index grating with respect to the writing intensity pattern were measured and calculated using the method described by Sutter and Günter.<sup>43</sup> In these calculations, the effect of the rewriting during the motion of the grating were taken into consideration. This is because the stage speed was slower ( $7.2 \mu\text{m/sec}$ ) than the time constant for the index grating build-up time (less than 1 second). The diffraction efficiency,  $\eta$ , which is the ratio of the intensity of diffracted light to that of the incident light, was measured in a degenerate four-wave mixing experiment. Two  $s$ -polarized laser beams with an intensity of  $760 \text{ mW/cm}^2$  were used as the writing beams, which were overlapped in the tilted sample with an incident-crossing angle of  $8.3^\circ$ . A probe beam is a weak  $p$ -polarized beam with an intensity of  $4.6 \text{ mW/cm}^2$ , counter-propagating along the direction of one of the writing beams. The spot diameter was reduced to  $620 \mu\text{m}$  with a 500 mm focus length lens. To exclude background light, the probe beam was chopped into the frequency of 317 Hz and the diffracted signal was amplified with a lock-in amplifier (Stanford Research Systems, Model SR510). All of the measurements were controlled by a personal computer (Dell, NetPlex 450/p).

### B. Photorefractive Gain Coefficient

The photorefractive gain coefficient was measured by a two-beam coupling experiment. A clear asymmetric energy transfer in two-beam coupling experiments was observed. Figure 2 shows the strong dependence of the photorefractive gain on the applied field. No gain was observed at a zero applied field. The relationship between the

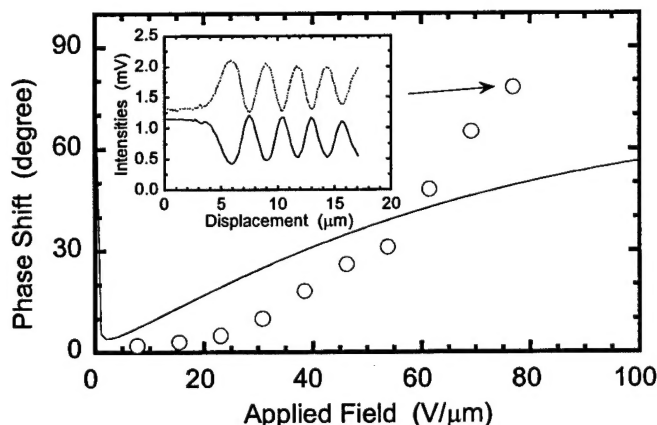


Figure 3 Phase shift as a function of applied field of steady-state refractive index grating with respect to the writing light intensity grating. The inset is a typical intensity of the two beams when the grating was moved about  $14 \mu\text{m}$  in the direction of grating vector.

photorefractive gain and the applied field is superlinear as a result of the field dependence of photogeneration quantum efficiency and mobility of charge carriers.<sup>44</sup> The largest gain obtained is  $76.9 \text{ cm}^{-1}$  at an applied field of  $77 \text{ V}/\mu\text{m}$ . Since the absorption coefficient of the material was  $6.42 \text{ cm}^{-1}$ , a net optical gain of  $70.4 \text{ cm}^{-1}$  was obtained.

The phase shift of the index grating was found to increase monotonically with the applied field starting from almost zero at a low field ( $< 30 \text{ V}/\mu\text{m}$ ) increasing to about  $78^\circ$  at  $77 \text{ V}/\mu\text{m}$  (Figure 3). The typical transmitted intensities of the two coupling beams during the translation of the grating are shown as an inset in Figure 3. Both the energy transfer and phase shift originated from the non-localization of photorefractive grating. The grating could be completely erased and rewritten with good reproducibility.

To measure the dependence of the gain coefficient on the spatial frequency of grating, the tilted angle of the sample normal was kept at  $40^\circ$  with respect to the symmetric axis of the two writing beams and the inner intersection angle of the two overlapped beams was changed from  $2.6^\circ$  to  $31^\circ$ . This experimental arrangement resulted in the grating spacing varying between  $0.4$  and  $4.4 \mu\text{m}$ , while the field component along the grating

vector remained constant under the fixed external field. The gain coefficient increases with the decrease of the spacing and the maximum is reached at about  $1\mu\text{m}$ . It then decreases steeply at a small grating space range (Figure 4).

### C. Diffraction Efficiency

The diffraction efficiency was measured with degenerate four-wave-mixing experiments and was also strongly dependent on the applied field (Figure 5). The index modulation from other mechanisms including photochemistry, thermorefraction, thermochromism, photochromism and  $\chi^3$  contribution are negligible because the index

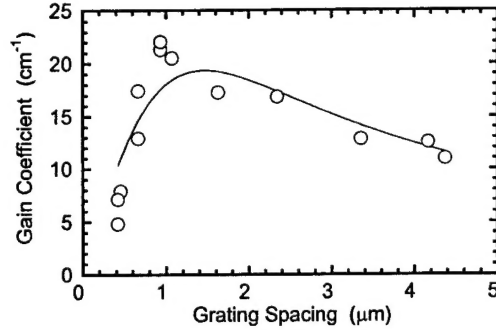


Figure 4 Gain coefficient as a function of grating spacing measured at applied field of  $66\text{ V}/\mu\text{m}$ . The circles are the experimental measurements. The solid line is the theoretical fit using Eq. (3) with  $E_{\text{eff}} = 102.6\text{ V}/\mu\text{m}$ .

modulation from these mechanisms do not depend on the applied field and some are irreversible without light treatment. A diffraction efficiency of 19.8% at an applied field of  $77\text{ V}/\mu\text{m}$  was achieved in films of  $130\text{ }\mu\text{m}$  in thickness. To investigate the influence of grating spacing on grating formation and erasure dynamics, we measured the response times at different beam-incident angles at a constant tilted angle.

### D. Photorefractive Sensitivity and Dynamic Range

The important advantage of the photorefractive all-optic modulator is its high sensitivity. A large index modulation can be achieved optically by milliwatt total power. Four definitions for the evaluation of photorefractive sensitivity are:<sup>1-4</sup>  $S_{n_1} = dn_i / dW_0 \times 1/\alpha$ ,  $S_{n_2} = dn_i / dW_0 = \alpha S_{n_1}$ ,  $S_{\eta_1} = d(\eta^{1/2}) / dW_0 \times 1/(\alpha l)$ , and  $S_{\eta_2} = d(\eta^{1/2}) / dW_0 \times 1/l = \alpha S_{\eta_1}$ , where  $n_i$  is the refractive index,  $\alpha$  is the absorption coefficient,  $W_0$  is the incident optical energy,  $\eta$  is the diffraction efficiency and  $l$  is the thickness of the hologram. Since the effective index modulation seen by a  $p$ -polarized probe beam,  $\Delta n$ , is related to the diffraction efficiency  $\eta$  by the expression:<sup>17, 42</sup>

$$\Delta n = \frac{\lambda(\cos\theta_2 \cos\theta_1)^{1/2} \sin^{-1}(\sqrt{\eta})}{\pi l \cos(\theta_2 - \theta_1)} \quad (1)$$

where  $\theta_1$ ,  $\theta_2$  are the internal propagation angles of the reading and diffracted beams in film, respectively. The relation between  $S_{n_1}$  and  $S_{\eta_1}$  is  $S_{\eta_1} = \pi \cos(\theta_2 - \theta_1) / [\lambda(\cos\theta_2 \cos\theta_1)^{1/2}] S_{n_1}$ .

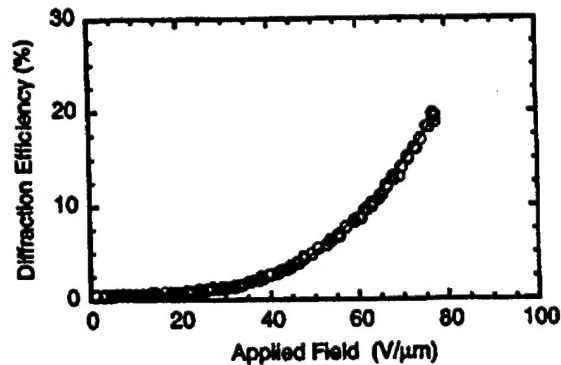


Figure 5 Dependence of diffraction efficiency on the applied field. The solid line is the theoretical fit using Eq. (3) with  $E_{eff} = 102.6 \text{ V}/\mu\text{m}$ .

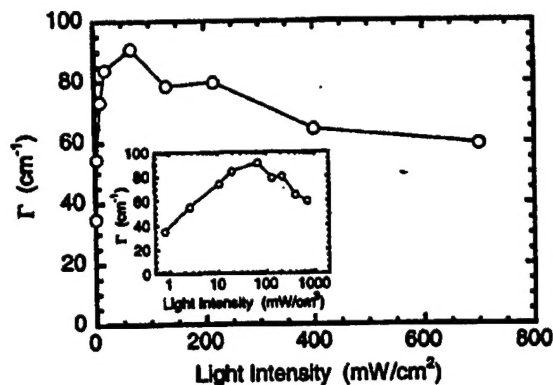


Figure 6 Photorefractive gain coefficient as a function of irradiation intensity of each writing beam (the intensity if the two beams were remained same). The inset is the same data but x-axis is in logarithmic scale.

To study the photorefractive sensitivity, we measured the two-beam coupling gain as a function of the coupling beam intensity (Figure 6). The intensities of the two beams were changed by rotating the quarter wave plate before the polarizer while equal intensities were maintained during the intensity variation. The optical gain is about  $35 \text{ cm}^{-1}$  when the light intensity is  $1 \text{ mW}/\text{cm}^2$  and increases quickly to its peak of about  $90 \text{ cm}^{-1}$  at the intensity of about  $70 \text{ mW}/\text{cm}^2$ . This is followed by a slight decrease in the high intensity region. The inset of the same figure depicts the semi-logarithmic plot to clarify the low intensity portion. The diffraction efficiency exhibited a similar trend as shown in Figure 7. The diffraction climbs fast to about 30% at the light intensity of about

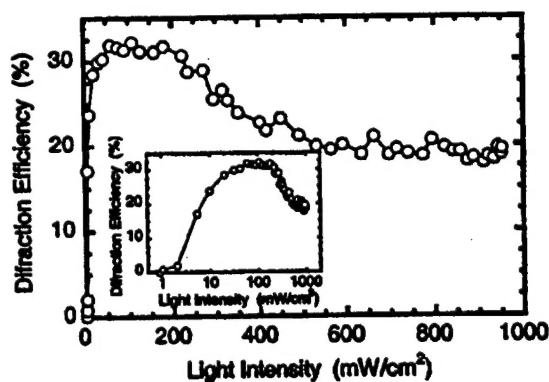


Figure 7 Diffraction efficiency as a function of irradiation intensity of each writing beam (the intensity of the two beams were remained same). The inset is the same data but horizontal axis is in logarithmic scale.



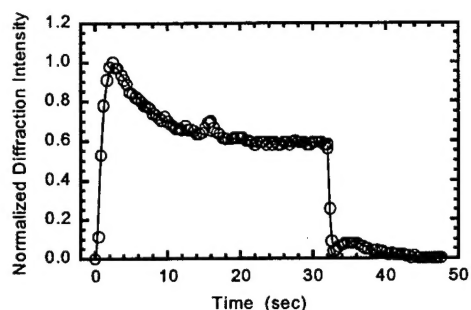


Figure 8 Diffraction efficiency as a function of time. The writing beams are turned on at  $t = 0$  and one of the writing beams is blocked at  $t = 32$  second. The solid line is a fitting of the data into a biexponential function (Eq. 4).

100 mW/cm<sup>2</sup>, and then goes down slightly as well. The details at low light intensity can be seen more clearly in the inserted semi-logarithmic figure. The diffraction efficiency around 1 mW/cm<sup>2</sup> is approximately zero in Figure 7, while the photorefractive gain of 36 cm<sup>-1</sup> at this intensity is shown in Figure 6. Since the intensity of the probe beam is comparable to those of the writing beams, the difference is caused by the erasure of the index grating by the homogeneous probe beam. Both intensity dependence behaviors of the gain and diffraction efficiency were reversible during the intensity scan. The photorefractive sensitivities of the sexithiophene derivative at the intensity of 80 mW/cm<sup>2</sup> were determined to be  $S_{n_1} = 18.7 \text{ cm}^3/\text{kJ}$ ,  $S_{n_2} = 120.1 \text{ cm}^2/\text{kJ}$ ,  $S_{n_1} = 0.34 \text{ cm}^2/\text{mJ}$ , and  $S_{n_2} = 2.2 \text{ cm}/\text{mJ}$ . The maximum refractive index modulation at this intensity was found to be 0.00075.

### E. Relaxation Processes

Figure 8 shows the diffraction efficiency variation with time measured at a grating spacing of 1.1  $\mu\text{m}$ . At  $t = 0$  sec, two writing beams were overlapped inside the sample. The diffraction signal increased rapidly to a maximum value and then decreased gradually until a steady-state diffraction efficiency was reached. At  $t = 32$  sec, the sample was illuminated only by a uniform light by blocking one of the writing beams. The diffraction efficiency decayed exponentially until it was nearly zero, appeared again for a short time, and eventually disappeared completely. In another measurement, one of the writing beams was blocked before the maximum diffraction efficiency was reached. The grating was exponentially erased as predicted by the standard photorefractive theory.

These phenomena are due to the cancellation and revelation of two types of gratings as has been observed in several inorganic crystals such as Bi<sub>12</sub>TiO<sub>12</sub>, Sn<sub>2</sub>P<sub>2</sub>S<sub>6</sub>, and Bi<sub>4</sub>Ti<sub>3</sub>O<sub>12</sub>.<sup>31, 33, 36, 45</sup> We propose that the two sets of photorefractive gratings are formed by two types of photoexcited charge carriers, electrons and holes. This is because of the bipolar transport property of this molecular photorefractive material, and the existence of two types of trap centers for the holes and electrons. The sexithiophene moieties of **1** provide a transport channel for the hole migration, while the methine dye acts as another transport channel for the electron migration because of the presence of a strong electron-withdrawing group.

When writing the gratings, a fast grating is initially built up through trapped holes because of their higher mobility (as shown later). This process results in the initial quick rise in the diffraction efficiency. Thus, the erasure of the grating at this stage shows a single exponential decay. If the grating writing continues for a longer time, the electron traps begin to fill up, thereby creating the slower complementary grating. Since the field built up by the electron traps is in the direction opposite to that by the hole-traps, cancellation of the net space-charge field and reduction in the diffraction efficiency were observed. When erasing the gratings in the period of stable diffraction, the space-charge

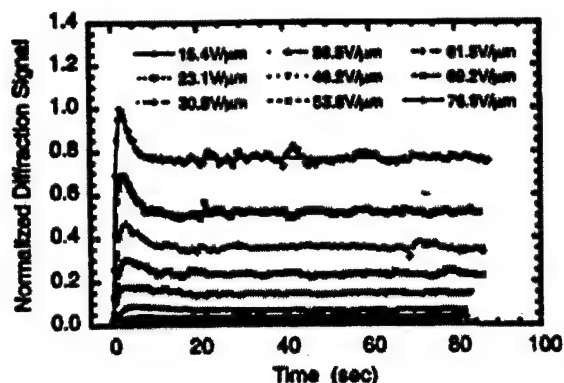


Figure 9 The temporal evolution of the normalized diffraction efficiency at different applied field. The writing intensity of each beam was  $760 \text{ mW/cm}^2$ .

field, as formed by the trapped holes, decays faster than that formed by the trapped electrons. Therefore, the net space-charge field changes signs during the erasure process. The diffraction efficiency first decreases to zero and then increases again. A revelation of the diffraction signal was thus observed.

The dynamics of the two sets of gratings were investigated by changing the applied field and irradiation intensity. Figure 9 shows the dynamic behavior of the grating formation in a four-wave mixing experiment. We examined the dynamic behavior at different applied field with a fixed intensity of  $760 \text{ mW/cm}^2$ . Obviously, an external field enhanced the formation of both types of grating. This is evidenced by the enhancement of the steady-state diffraction efficiency and the increase in the amount of the cancellation of the diffraction efficiency at a high field. Figure 10 shows the temporal change of the diffraction efficiency at different writing intensities. The experiment was carried out at a fixed applied field of  $77 \text{ V/}\mu\text{m}$ . These data indicate that the diffraction efficiency increases with the writing intensities, yet it tends to be saturated at high intensities.

## (2) HOLE AND ELECTRON TRANSPORT

### A. Time-of-Flight Experiments

As mentioned above, a crucial condition for the formation of the complementary gratings is the existence of two transporting channels: one for the migration of electrons

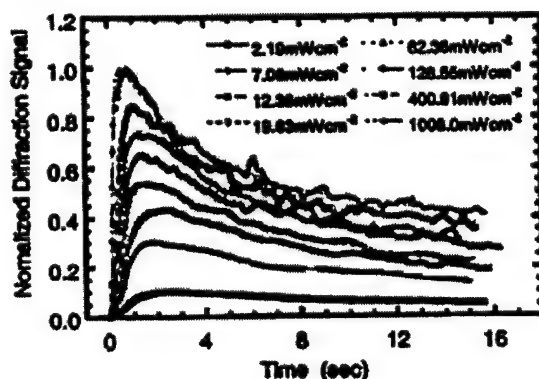


Figure 10 The temporal evolution of the normalized diffraction efficiency at different intensity of each writing beam. The applied field was  $77 \text{ V/}\mu\text{m}$



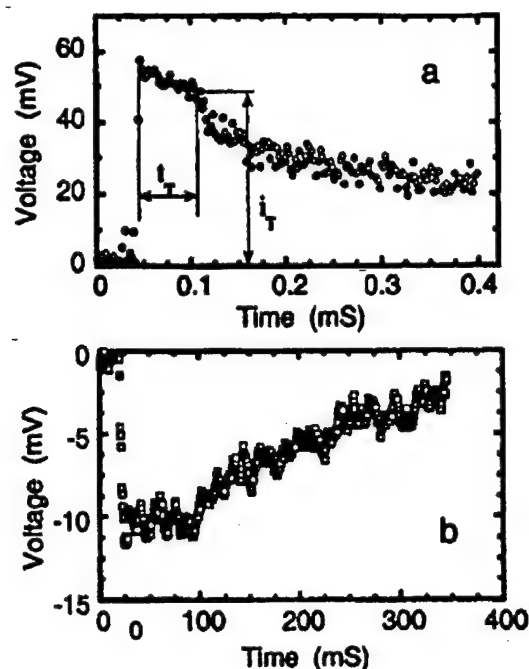


Figure 11 Two typical time-of-flight signals for hole (a) and electron (b) transport. The  $t_T$  is transit time.

and another for the migration of holes. To examine, experimentally, the coexistence of two channels for electron and hole transport, we measured the mobility and the photogeneration efficiency for holes and electrons, respectively, by time-of-flight experiments.<sup>44, 46, 47</sup>

These measurements were carried out independently as a function of an applied field. For the observation of the time-of-flight signal of holes' transport across a film, a sample of 27  $\mu\text{m}$  thick sandwiched between a piece of ITO glass and an aluminum plate was used. Frequency doubled laser pulses ( $\lambda = 532 \text{ nm}$ ) of about 40 picosecond FWHM (full width at half maximum) from a mode-locked Nd:YAG laser (Continuum, Model PY61C-10) irradiated the film from the positively charged ITO electrode, while the aluminum electrode was connected to a grounded resistor. Since the absorption coefficient of the material at the working wavelength of 532 nm is about  $7900 \text{ cm}^{-1}$ , a charge carrier sheet approximately 1.5  $\mu\text{m}$  thick was formed beneath the transparent electrode. Under the action of the external field, holes were drifted across the film to the grounded electrode. This resulted a transient current, which was measured by recording the potential drop across the resistor with a digital oscilloscope (LeCroy, Model 9354A). A typical transient current for the hole transport is shown in Figure 11a. The current pulse did not show the rectangular shape, but rather it showed a featureless decay. Since the material is a disordered solid, the generated carriers experienced a distribution of hopping times. Therefore, the carrier packet that was formed as a thin sheet at the front surface of the sample was broadened as it penetrated the bulk. The experimental transit time was determined by  $t_T$  as shown in Figure 11a.

According to the photorefractive analyses in the preceding section, electron transport is available in the materials as well. Measurement of the electron mobility confirmed this assumption. The experimental conditions for this measurement were the same as the mobility measurement of holes except that the grounded electrode was another ITO glass and the front ITO glass electrode was negatively charged. A typical transient current signal for electron transport is shown in Figure 11b. The electron transit time is much longer and the amplitude of the current is also smaller than what was observed in hole transport. This strongly suggests the existence of an electron transport channel in our molecular system.

### B. Mobility of Hole and Electron

The drift mobilities for hole and electron transport are readily calculated from the transit times  $t_T$  at different external fields using the expression:  $\mu = d^2/Vt_T$ , where  $d$  is the sample thickness and  $V$  is the applied voltage.<sup>44, 47, 48</sup> The hole and electron drift mobilities as a function of an applied field are depicted in Figure 12. Both mobilities are

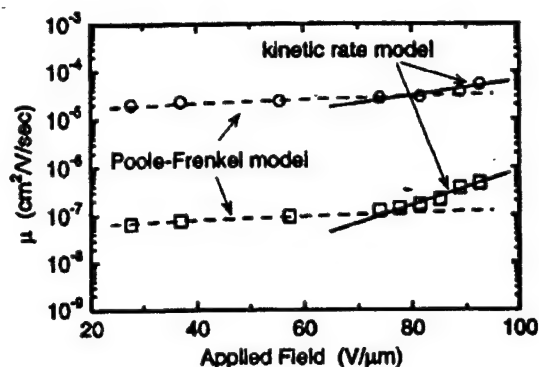


Figure 12 Hole and electron mobility (circles and squares) as functions of applied field. The dashed and solid lines are best fittings using Eqs. (5) and (6), respectively.

strongly enhanced by the applied field. This figure also shows that the enhancement of the electron mobility is more favorable than the enhancement of the hole mobility.

### C. Photogeneration Quantum Efficiencies

In the external circuit, the drifting charge is manifested as a constant current  $i = Q\mu E/d$ , where  $Q$  is the total charge injected into the sample by the incident light flash  $F$  (absorbed photons per second). Knowing the current  $i_T$  and mobility  $\mu$  (Figure 10a), the quantum efficiency, as defined as the number of carriers generated per absorbed photon, was estimated from the relation of  $\Phi = Q/eF$  where  $e$  is the electron charge. A strong dependence of the quantum efficiencies for both hole and electron carriers on the applied field was similar to those reported for the disordered materials (Figure 13). The solid lines are Onsager fittings<sup>49</sup> using the parameters listed within Figure 13.  $\Phi_0$  is the initial yield of thermalized bound pairs and is independent of field and  $r_0$  is the thermalization distance.

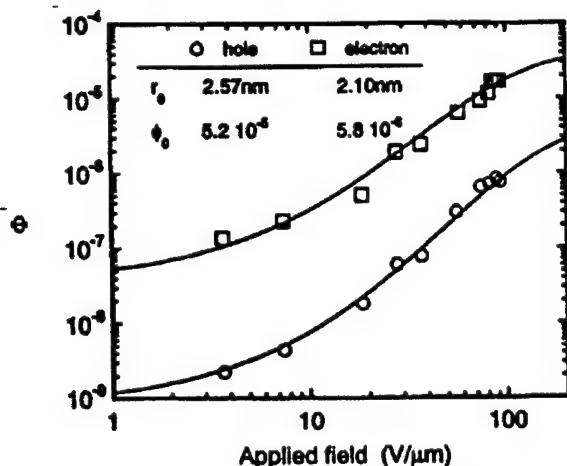


Figure 13 Photogeneration quantum efficiencies for hole and electron generation. The solid lines are Onsager theory fitting with parameters listed in the Figure.

## III. DISCUSSIONS

### A. Charged Carrier Transport Channels

Although the competition of complementary gratings explains the experimental data and the mobility measurements confirm the bipolar transport nature of the material, it was necessary to examine these phenomena at the molecular level. It is also necessary to correlate the photorefractive and charge transport data with a photorefractive model. We used cyclic voltammetry to determine the ionization potential and electron affinity of each component of the molecule in solution.<sup>50</sup> Solution electrochemical measurements can be used to describe electro-transfer reactions in the condensed phase if we assume that the differences in ionization potential and electron affinity of the component of the molecule in solution are equal to or smaller than those same energy differences in the condensed phase.<sup>51</sup>

The ionization potentials were deduced from the cyclic voltammetry measurement of the electro-active species at a concentration of  $3 \times 10^{-3}$  mol/dm<sup>3</sup> in dichloromethane solutions containing 0.1 mol/dm<sup>3</sup> tetrabutylammonium tetrafluoroborate as the supporting electrolyte.<sup>41</sup> The Ferrocene/ferrocenium-ion couple was used as an internal standard. The HOMO (highest occupied molecular orbital) and LUMO (lowest unoccupied molecular orbital) energy levels were estimated from the equations:  $E_{HOMO} = E_{ox}^0 + 4.4$  eV and  $E_{LUMO} = E_{re}^0 + 4.4$  eV, where  $E_{ox}^0$  and  $E_{re}^0$  are oxidation and reduction potentials with respect to the standard hydrogen electrode (SHE) and the value of 4.4 is the ionization potential for hydrogen in eV.<sup>52, 53</sup> We characterized the band-gaps of the three compounds spectroscopically by finding their band-edges, which are also listed in Table I.

The HOMO and LUMO energy levels of the methine dye (Compound 3 in Table I) were calculated to be -5.82 and -3.48 eV, respectively, with respect to the vacuum level from its lowest oxidation and reduction potentials. The band-gap,  $\Delta E_{electrochemical}$ , was estimated to be 2.34 eV. This value is in good agreement with the spectroscopic estimate of the band-gap  $\Delta E_{optical}$ , 2.30 eV. The HOMO energy of a sexithiophene molecule alone (Compound 2) was estimated to be -5.48 eV. Since the reduction potential of sexithiophene is out of the solvent window, the LUMO energy level (-3.00 eV) was deduced from the band-gap of the sexithiophene backbone which was estimated from the photoabsorption edge (2.48 eV). If we assume that there is no ground-

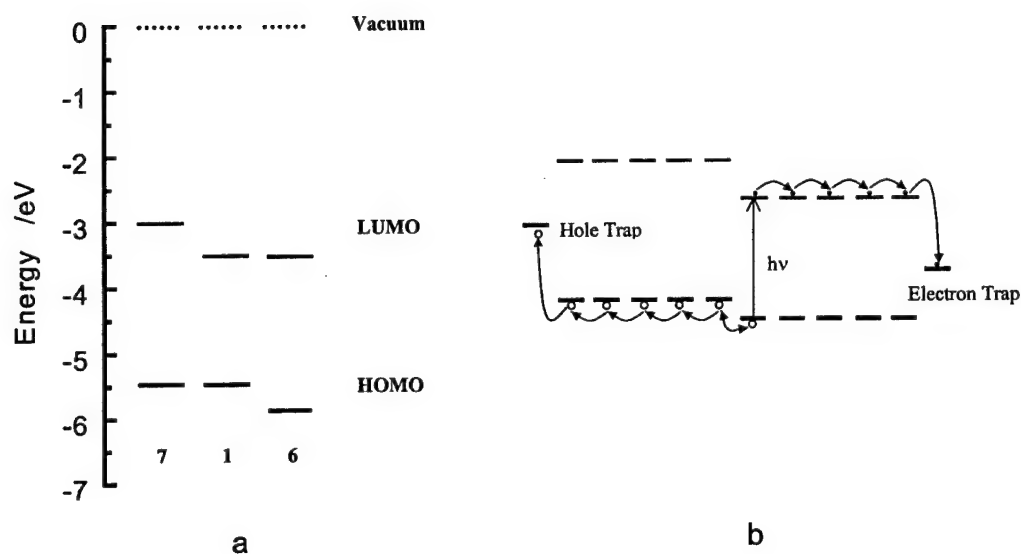


Figure 11

Figure 14 (a) Estimated energy levels of HOMO and LUMO of fully functionalized photorefractive molecule (Compound 1), sexithiophene derivative (Compound 2) and methine dye (Compound 3) with respect to the vacuum level. (b) Proposed charge carrier transport channels. See text for details.

intramolecular interaction between the sexithiophene backbone and the methine dye, the energy levels in our photorefractive molecule should remain identical to their individual components. Indeed, the HOMO and LUMO energy levels for the photorefractive molecules (Compound 1) were electrochemically determined to be -5.42 eV and -3.48 eV, respectively (Table I). These are close to those of the individual compounds. A potential energy diagram can be constructed as shown in Figure 14a. A photogeneration of charge carriers occurs upon absorption of a photon by the dye. An electron can be transported away along the LUMO of the methine dye and the hole tends to transfer to sexithiophene HOMO under the action of an external field. The

holes and electrons are further drifted away by sequential hopping to neighboring sexithiophene backbones and methine dyes and can be fixed by individual trapping centers, respectively (Figure 14b).

### B. Bipolar Two-Trap Models

There are several photorefractive models that account for the bipolar transport. A recent review on these models is provided in Ref.<sup>2</sup>. The model most consistent with our experimental results is the bipolar two-trap model, which is based on the assumption that two types of active centers are involved in simultaneous electron-hole transport.<sup>34, 37, 38</sup> This model has been used for the interpretation of the behaviors of complementary gratings in inorganic photorefractive crystals. According to this model, there are two independent systems of photoactive centers in which the prevailing carriers are electrons and holes, respectively. One of the gratings is set up by the redistribution of electrons and another is set up by the redistribution of holes. The two gratings are 180 degrees out of phase with each other and are known as complementary gratings. Since the total space-charge field is the sum of the fields created by each type of carrier caught by different traps, the net amplitude of the space-charge field is smaller than that of the contribution from the principal set of space charges. If their characteristic time constants are different, then the individual gratings can be revealed during writing and erasure.

The model predicts an expression for the steady-state space-charge field as:<sup>34</sup>

$$E_{sc} = j \frac{E_{qD} - E_{qA}}{1 + j \frac{E_{qD}}{E_0 + jE_D} - j \frac{E_{qA}}{E_0 - jE_D}} \quad (2)$$

where  $E_D = \frac{k_B T}{e} K$ ,  $E_{qD} = \frac{e}{\epsilon_s K} \frac{(N_D - N_{D0}^+) N_{D0}^+}{N_D}$ ,  $E_{qA} = \frac{e}{\epsilon_s K} \frac{(N_A - N_{A0}^-) N_{A0}^-}{N_A}$ , are the diffusion field, the trap-

limited space-charge fields of *N*-type, and *P*-type species respectively.  $N_{A0}^- = N_{D0}^+$ ,  $k_B$  is the Boltzman constant,  $T$  is the absolute temperature,  $K$  is the spatial frequency of grating,  $e$  is the charge of electron,  $\epsilon_s$  is the static dielectric permittivity,  $N_D$ ,  $N_A$ ,  $N_{D0}^+$ ,  $N_{A0}^-$  are the total concentration of donors and acceptors, and the concentration of ionized donors and acceptors respectively. The  $E_D$  value is 0.16 V/ $\mu$ m at a 1  $\mu$ m grating spacing and the room temperature, and is much smaller than the applied field in our experiments (which is the case for the most organic photorefractive films). Under the condition of  $E_0 \gg E_D$ , Eq. (2) can be expressed as

$$E_{sc} = \frac{E_{qeff}(E_0 - jE_D)}{E_D + E_{qeff} + jE_0} \quad (3)$$

where  $E_{qeff} = E_{qA} - E_{qD}$ . Eq. (3) is the same formula as the "standard model of photorefraction"<sup>22</sup> when the one species trap-limited field  $E_q$  is replaced with an effective trap-limited field  $E_{qeff}$ . Therefore, the bipolar two-trap model predicts the same steady-state photorefractive behaviors as the standard model. Eq. (3) explains the reason why the field and grating spacing dependences of the gain coefficient and the diffraction efficiency (Figures 2, 3, 4 and 5) are similar to those reported in the mono-polar polymeric and molecular photorefractive materials. Fitting Eq. (3) into the gain coefficient and the diffraction efficient data (solid lines in Figures 2, 3, 4 and 5) results in the effective trap-limited field  $E_{qeff} = 94.5 \sim 103.0$  V/ $\mu$ m. The sign of the space-charge field and, therefore, the direction of the energy transfer, depends merely on the sign of field  $E_{qeff}$ , which is determined by the relative density of the donor and acceptor traps. Varying the grating spatial frequency cannot change the sign of the steady-state space-charge fields. On the contrary, in the bipolar single-trap model, the steady-state gain coefficient can change signs with the grating period. This is because the phase of the space-charge field depends on the uncoupled response time of the electron- and the hole-transport processes<sup>54, 55</sup>. Therefore, the space-charge fields formed by trapped electrons and holes cannot be determined individually from measuring the steady-state properties; however, the time-dependent measurements can accomplish this function.

The sign of the space-charge field, and hence the direction of energy transfer in the bipolar two-trap model, can change with time during the writing and erasure of complementary gratings. The condition is that their characteristic time constants must be different. The sign of the space-charge field in the erasing process depicted in Figure 8 must change after the dip since the diffraction efficiency is proportional to the square of the space-charge field. The time for the dip was delayed when the grating spacing increased as shown in Figure 15, where dips appeared at about 2.5, 7.3 and 20.0 seconds

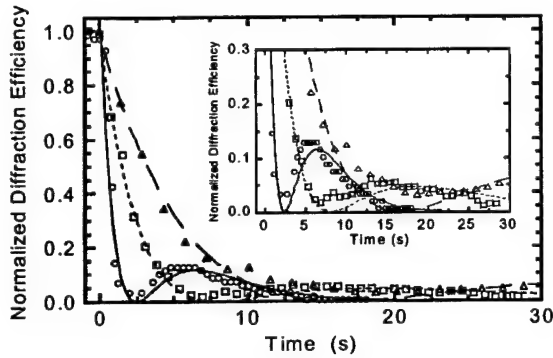


Figure 15 Normalized diffraction efficiency as a function of time during the grating erasure. The circles, squares and triangles are experimental measurements with the grating spacing of 1.1, 1.9 and 4.4  $\mu\text{m}$ , respectively, at an applied field of 77 V/ $\mu\text{m}$ . The lines are theoretical fits using a biexponential function (Eq. 4). The inset is its enlarged plot.

of erasure time for the gratings with spacing of 1.1, 1.9 and 4.4  $\mu\text{m}$ , respectively. The sign of the space-charge field did not change in the writing process in Figure 8 for two reasons: firstly, since the space-charge field contributed from the hole was dominated, and secondly, since the build-up time constant for the hole grating is faster than that for the electron grating. We also did not observe a diffraction efficiency dip during the grating writing process in the spacing range from 0.4 to 4.5  $\mu\text{m}$ . This would be possible under certain conditions, according to the bipolar two-species models, that if the response rate for electrons become smaller than the rate for holes during the variation of the grating spacing.<sup>34, 54</sup> In contrast to the case in the bipolar two-trap model, the grating formation and erasure in the one-species electron-hole competition model follow single exponential functions.<sup>54-56</sup>

The expression for the writing and erasing diffraction efficiency is:<sup>34, 37</sup>

$$\eta(t) \propto \left| E_e \left[ 1 - \exp\left(-\frac{t}{\tau_e}\right) \right] - E_h \left[ 1 - \exp\left(-\frac{t}{\tau_h}\right) \right] \right|^2, \quad \text{and} \quad \eta(t) \propto \left| E_e \exp\left(-\frac{t}{\tau_e}\right) - E_h \exp\left(-\frac{t}{\tau_h}\right) \right|^2 \quad (4)$$

where  $E_e$  and  $E_h$  are the steady-state space-charge fields built up by the trapped electrons and holes, and  $\tau_e$  and  $\tau_h$  are the time constants for the electron- and hole-transport systems. Fitting the data according to the writing and erasure processes into Eq. (4) yielded the lines in Figures 8, 15.

This model requires a zero diffraction efficiency dip during erasure due to the 180 degrees phase difference of the complementary gratings. Since the space-charge field is completely canceled at the dip, a non-zero dip can be observed only when there is a slight phase-shift in the complementary gratings. This phase-shift can be due to either the vibration during hologram recording<sup>37</sup> or to the simultaneous appearance of photochromic or absorption grating.<sup>57</sup> In our experiments, a non-zero dip was observed only when the measurements were performed under noisier conditions.

Although similar grating cancellation and revelation behavior have been observed in other photorefractive polymeric composites, it was attributed either to the trap's intercommunication or to residual ionic motion.<sup>28-30</sup> However, the complementary gratings that are reported in this paper are formed by the space-charge field of two types of *photogenerated charge carriers*.

### C. Grating Dynamics

Figure 16 shows the influence of the writing beam intensity and applied field on the build-up dynamics of the primary grating and its complementary grating ( $\tau_e$  and  $\tau_h$ ). Figure 14a shows time constants ( $\tau_e$  and  $\tau_h$ ) as a function of the writing beam intensity, and indicate that both time constants decrease with increased intensity. Figure 17 shows

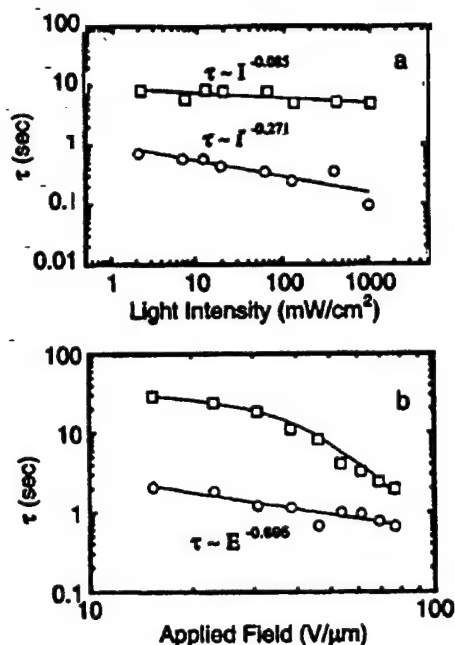


Figure 16 Time constants for build-up of a fast grating (circles) and a slow complementary grating (squares) as functions of illumination light intensity (a) and applied field (b).

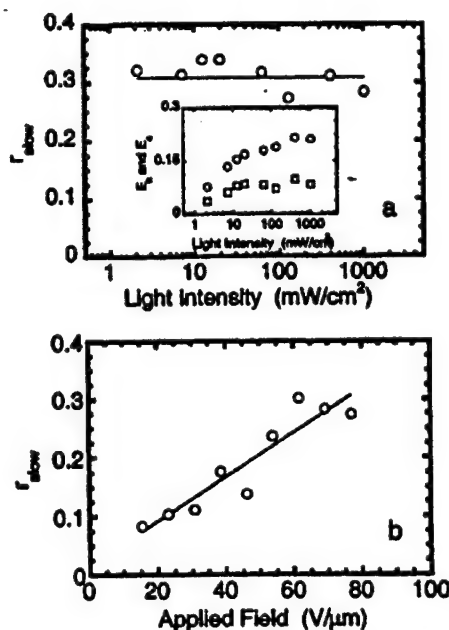


Figure 17 Magnitude fraction of slow grating  $r_{\text{slow}} = E_e / (E_e + E_h)$  as functions of illumination light intensity (a) and applied field (b). The inset in (a) is the  $E_e$  and  $E_h$  as a function of light intensity.

the relationships of the magnitude fraction of the slow component of a space-charge field, defined as  $r_{\text{slow}} = E_e / (E_e + E_h)$  with the writing beam intensity and the applied field. The  $\tau_e$ ,  $\tau_h$ ,  $E_e$  and  $E_h$  values were obtained by fitting Eq. (4) into the dynamic data in Figure 9 and Figure 10. The standard photorefractive theory predicts that the time constant is inversely proportional to the carrier mobility and the intensity of the writing beams (time constant  $\propto 1 / \text{mobility} \times \text{intensity}$ ) (Ref.<sup>11,58</sup>). However, the dependence of time constants on the light intensity of both holes and electrons is much weaker than the above relationship, and those reported in other organic and inorganic monopolar transport materials.<sup>3, 4, 14, 29, 59</sup> In this low- $T_g$  photorefractive material, the fast component of response times can be hindered by the NLO reorientation besides the space-charge field formation. This is because the NLO reorientation speed in the rubbery state of amorphous matrix is independent



of the light intensity<sup>60</sup> yet controlled by the diffusion constant.<sup>61</sup> Therefore, fast grating formation can be subjected to the hindrance from the reorientation motion of NLO chromophores. The field induced birefringence measurement shows that the time constants for the build-up of the index birefringence under the action of external fields are in the same order as the fast component of the response time of the grating formation<sup>41</sup>. Though the slow electron grating is not hindered by the NLO reorientation, it has an even weaker dependence on the light intensity than the fast grating. This slowing-down could come from the interaction between the complementary gratings. The principal space-charge field build-up by holes accelerates the migration of the slow complementary grating. As a result, the interaction force weakens the effect of the light intensity on the time constant of the slow grating. In order to understand the applied field dependence behaviors of time constants more deeply, let us consider further about the field dependence of carrier mobility shown in Figure 12. The field dependence of the mobility in disordered organic films has been described by the Poole-Frenkel effect, kinetic rate models, the Marcus theory, the dipole trap argument, and by the disordered formalism.<sup>44</sup> It was found that none of the above theories covers the whole range of the field measured. It was further noticed that in the low field range of  $E < 70$  V/ $\mu$ m, the mobilities show much weaker dependence on the field and follow the relationship predicted by the Poole-Frenkel effect. At a high field range ( $70 < E < 100$  V/ $\mu$ m), the data can be well fitted into the kinetic rate theory. This inconsistency in the mechanisms throughout the measurement range can be attributed to a quasi-morphology difference at different applied field as a result of the low- $T_g$  nature of the material. The chromophores are more randomized at a low field than at a high field. The Poole-Frenkel effect describes the reduction in the ionization energy of a carrier in a Coulomb potential by an applied field. The dependence of the mobility on a field can be expressed as<sup>44</sup>

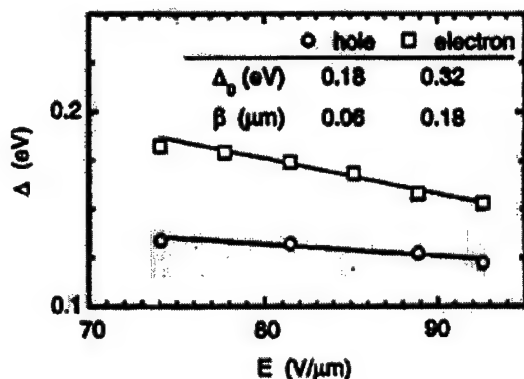


Figure 18 The activation energy for hole (squares) and (circles) electron hopping.

$$\mu = \mu_0 \exp(\beta_{PF} E^{1/2} / kT) \quad (5)$$

where  $\beta_{PF} = (e^3 / \pi \epsilon \epsilon_0)^{1/2}$ ,  $\epsilon$  is the dielectric constant at high frequency, and  $\epsilon_0$  is the permittivity of free space. The kinetic rate theory assumes that the electron and hole transports occur by hopping among the localized states, and the mobility can be adopted as:<sup>44, 47</sup>

$$\mu = 2 \frac{\rho}{E} v \exp\left(-\frac{\Delta(E)}{kT}\right) \sinh\left(\frac{\rho e E}{2kT}\right) \quad (6)$$

where  $\rho$  is the average separation of the transporting agents,  $v$  is the attempt frequency of electron-exchange between charged and uncharged localized discrete chemical species,  $\Delta(E) = \Delta_0 - \beta E$  is the activation energy for the hopping process, and  $\Delta_0$  is the zero field intercept.<sup>62</sup> The dashed and solid lines of Figure 12 are the best fitting results by using Eqs. (5) and (6), respectively. In the fitting, the dielectric constant  $\epsilon$  is assumed to be 3.0 and the average distance value,  $\rho$ , for both hole and electron transport species is 13.9 Å. It is calculated from the formula  $\rho = (M / (Ad))^{1/3}$ , where  $M$  is molecular weight of photorefractive sexithiophene (1946.16),  $d$  is the density (1.2) and  $A$  is Avogadro's number ( $6.02 \times 10^{23}$ ). The resultant zero field intercept  $\Delta_0$  and  $\beta$  values are listed as an inset in Figure 18. The activation energies for both holes and electrons are slightly dependent on the external field, but the electron has a larger  $\Delta$  value than the hole and is more strongly influenced by the external field (Figure 18). While the  $\beta$  value for electron hopping is larger than for hole hopping, the activation energy for electron hopping decreases faster with the applied field than for the hole hopping. As a result, the time constant of slow grating at a high-applied field is more sensitive to the changes in the applied field than that of



the fast grating (Figure 16). This is because the mobility follows the kinetic rate theory at a high-applied field (Figure 12). The  $r_{slow}$  value reflects the relation of the two gratings at steady-state conditions.

Figure 17a shows the  $r_{slow}$  value as a function of the intensity of the writing beam at a constant applied field ( $E_{applied} = 77 \text{ V}/\mu\text{m}$ ). It can be seen that the  $r_{slow}$  values remain almost unchanged over a variation in the intensity span almost three orders of magnitude. Meanwhile, the absolute space-charge field magnitude of the fast component,  $E_h$ , triples in value and a saturation of the space-charge fields,  $E_e$  and  $E_h$ , appears at a writing intensity of about  $I_w = 50 \text{ mW}/\text{cm}^2$  (see the inset of Figure 17a). It can be readily

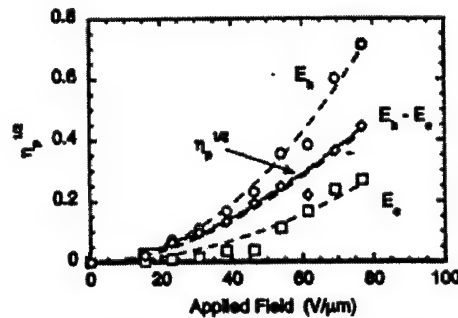


Figure 19 The  $E_e$  and  $E_h$  (squares and circles), as well as the  $E_h - E_e$  value and square root of diffraction efficient (diamonds and solid line) as a function of light intensity.

understood that  $r_{slow}$  is invariable when  $I_w > 50 \text{ mW}/\text{cm}^2$  because both space-charge field components from trapped electrons and holes reach their individual trap-limitation conditions as indicated by Eq. (2). For the case of  $I_w < 50 \text{ mW}/\text{cm}^2$ , the  $r_{slow}$  remains constant because the relation of the photoexcited electron and hole densities remains constant, and because the space-charge field built up by each carrier still depends on the density of two types of traps. On the other hand, the  $r_{slow}$  value increases when the applied field increases at a constant light intensity ( $I_w = 760 \text{ mW}/\text{cm}^2$ ) as shown in Figure 17b. This trend is consistent with Eq.(2) because under the condition of  $E_{qD} > E_{qA}$ , the trap density-limited space-charge field due to trapped electrons depends more strongly on the applied field than the trapped holes.

Equation (2) reveals that the overall space charge field is, in fact, a superposition of two space-charge fields from two types of trapped charges. Our results indeed confirm this prediction (Figure 19). Agreement is observed between  $\sqrt{\eta}$  and  $E_h - E_e$ . The dashed lines are the fitting by Eq. (3).

It is important to point out that the complementary grating observed in our sexithiophene photorefractive materials is not due to a passive motion of residual ions as described in Ref.<sup>30</sup> If the complementary grating originated from this reason, the  $r_{slow}$  value in Figure 17a could not have remained constant. The space-charge field from ions should always satisfy the trap density limitation condition since the number density of ions is independent of light intensity. This assertion was supported by photocurrent measurement results as shown in Figure 20. It is indicated that the photocurrent increases super-linearly with the applied field, while the dark current remains zero as the external field is increased up to  $90 \text{ V}/\mu\text{m}$ . The revelation effect that we observed should not be attributed to the appearance of a monopolar shallow trap<sup>63</sup> because the diffraction

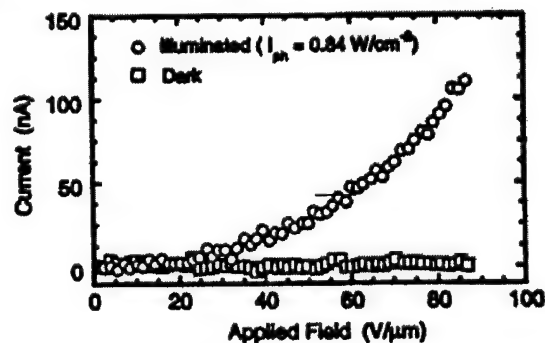


Figure 20 Photo- and dark current measured from a  $27 \mu\text{m}$  thick sample.

efficiency dipped to zero under uniform illumination. This is not the case for the shallow trap model.<sup>64</sup> An oscillation on the space-charge field in mono-polar photorefractive materials can happen at the initial stages of grating formation and erasure.<sup>65, 66</sup> The "density" gratings of the photoexcited carriers drift along the grating vector direction under the action of a high external field. If the drift length is longer than the grating space, then the rise and fall of the amplitude of the Coulomb electric field grating can be observed before significant diffusion takes place. This is caused by the movement of the carrier grating from zero to 180 degrees, and back to the in phase with the stationary grating of ionized traps<sup>65</sup>. This kind of oscillation is not complete and will be dampened due to carrier recombination. A zero dip similar to the complementary grating competition cannot be observed.

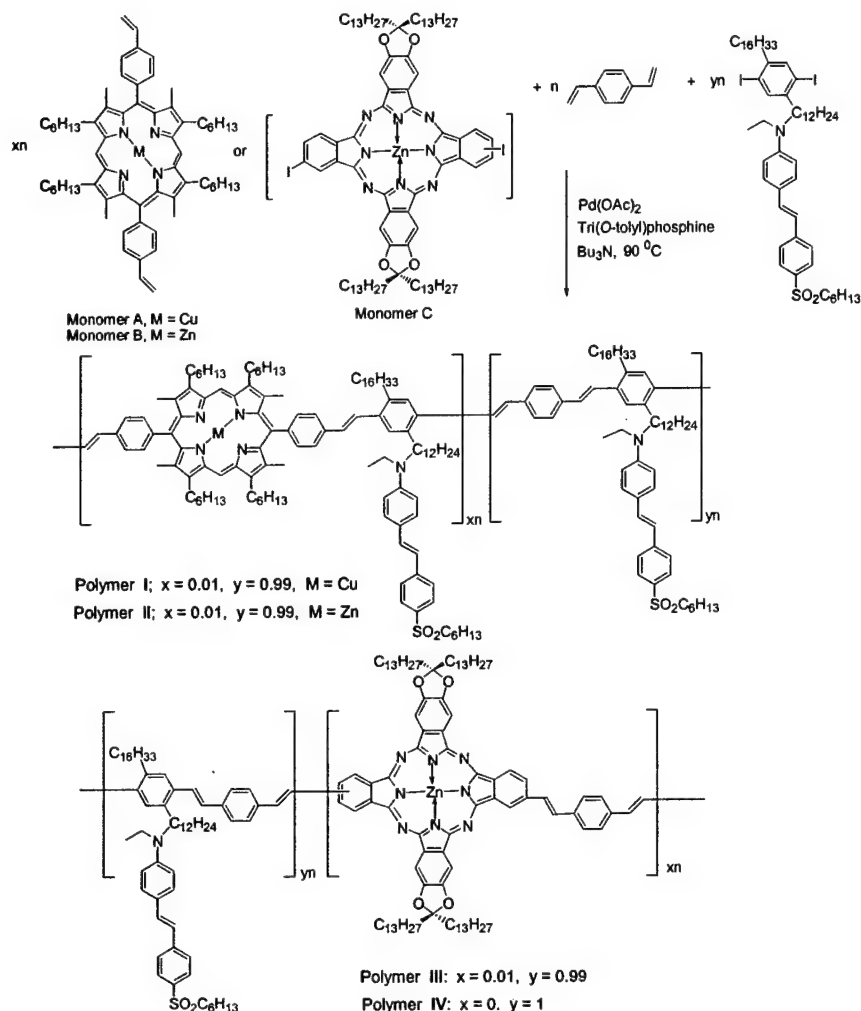
### C. Syntheses of Novel Photorefractive Polymers and Effects of the Nature of Transition Metal Phthalocyanine and Porphyrin Complexes On PR Performances

Photorefractive (PR) materials allow reversible modulation of the refractive index under the irradiation of a non-uniform light.<sup>1</sup> To manifest photorefractive effect, a polymer is required to possess photoconductivity and electro-optic response. To accomplish an efficient PR response in a material, one of the crucial issues is to establish a high space-charge field through the efficient generation, transporting and trapping of photocharge carriers. However, the quantum yield for charge generation in organic materials is usually low due to their low dielectric constant and numerous channels causing the relaxation of excited states to ground states.<sup>3</sup> Recently, we developed a hybridized strategy to address this problem. An ionic tris(bipyridyl)ruthenium complex, which has an efficient photoinduced metal-to-ligand charge transfer (MLCT) process, was introduced into a conjugated polymer with NLO chromophore side chains.<sup>4</sup> It was envisaged that the combination of the efficient MLCT process of the ruthenium complexes and the efficient charge transporting process of the conjugated backbone would lead to a high charge separation efficiency and therefore to a better PR performance. This idea was quite successful in preparing a high Tg PR polymer. A net optical gain of about 200 cm<sup>-1</sup> was achieved in a PR polymer with a Tg of 130 °C. However, in a low Tg version, no net gain was obtained because of the local field generated by the alignment of ion pairs around photocharge generation sites in response to the external field.<sup>5</sup> The investigation of such local field effect suggests that a neutral metal complex with an effective photoinduced charge generation mechanism might be utilized as a photosensitizer in low Tg PR polymers to obtain high performance PR materials. In this communication, we report synthesis of novel low Tg PR polymers containing neutral transition metal phthalocyanine and porphyrin complexes (Scheme 1).

Porphyrin and its derivatives are well-known model compounds for photosynthetic processes involving charge separation.<sup>6</sup> Metalloporphyrin and metallophthalocyanine have been extensively studied as photosensitizers for photodynamic therapy, light-harvesting materials and organic solar cells.<sup>7</sup> A high quantum yield of charge separation could be achieved in these systems. It was found that these PR polymers are the best fully functionalized PR polymers synthesized to date. It was also observed that the nature of these transition metal macrocyclic complexes significantly affect the PR performance of these polymers.

Four polymers were synthesized via the Heck polycondensation (Scheme 1). Monomers **A** and **B** were synthesized from corresponding dipyrromethane and 4-vinylbenzaldehyde followed by metallation.<sup>8</sup> Monomer **C** was prepared by coupling of diiminoisoindoline and 6/7-iodo-1,3,3-trichloroisoindolenine and subsequently zinc acetate dihydrate.<sup>9</sup> It is known that phthalocyanine (Pc) has a strong tendency for self-association due to the planar shape and aromatic nature. To obtain non-aggregating and soluble Pc, long alkyl chains were introduced through ketal linkages to the Pc (monomer **C**).<sup>10</sup> The polymerizations were carried out smoothly in DMF using a typical Heck reaction condition as indicated. Amorphous polymers, as indicated by DSC, polarizing microscopy and x-ray diffraction studies, were obtained in excellent yields and reasonably high molecular weight.<sup>11</sup> It is interesting to note that polymer **III** show especially higher molecular weight compared to polymer **I**, **II** and **IV**. Apparently, the electron-deficient Pc facilitated the oxidative addition in the palladium-catalyzed reaction. To our knowledge, this is the first example that the metal Pc was incorporated into a fully conjugated polymer backbone. DSC studies revealed Tgs of about 16 °C for all of the four polymers. The

Scheme 1. Synthesis of polymer **I** - **IV**.



$^1H$  NMR spectra of the polymers feature the chemical shifts of the NLO chromophore and the poly(phenylenevinylene) backbone. However, the presence of metal complex moieties in polymers **I-III** is manifest by the appearance of Q bands from metalloporphyrin and zinc Pc in the UV/vis spectra of the polymers (Figure 1). The Q bands in both polymer **I** and **II** are consistent with their corresponding monomer **A** and **B**, appearing at around 535, 571 nm and 540, 574 nm, respectively. On the other hand, Q bands in polymer **III** shows a significant red shift of about 19 nm with respect to those in monomer **C** (669, 684 nm). This is presumably caused by the more extensive electron delocalization between Pc and PPV backbone. The results of microanalysis also supported the structures of the polymers.<sup>9</sup>

Although these polymers have very similar structures except the small amount of photosensitizers, their physical properties exhibit interesting differences. As illustrated in Figure 1, Polymer **I, II** and **III** exhibit much higher photoconductivity than does polymer **IV**, which proves our idea that the incorporation of metalloporphyrin and zinc Pc into a conjugated backbone will enhance the photosensitivity of the resulting polymers in the visible region.<sup>12</sup> In contrast to the behavior of previous ionic ruthenium containing

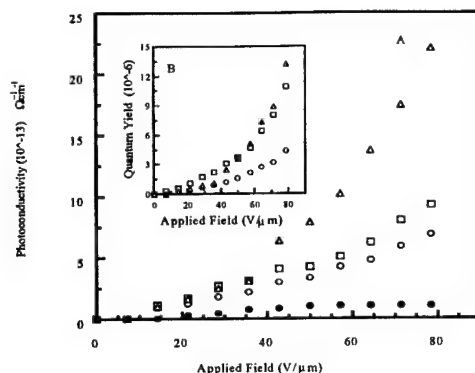


Figure 1. Photoconductivity (A) and quantum yield of photocharge generation (B) of polymers I (o), II (◊), III (Δ) and IV (●) as a function of external electric field.

polymer,<sup>5</sup> polymers I, II and III all display nonlinear field enhancement behavior in both photoconductivity and quantum yield. Polymer III shows the highest photoconductivity and quantum yield of photocharge generation. This feature can be attributed to the different electron affinity between Pc center and PPV backbone, which facilitates the charge separation once the exciton is generated. The PC center is more electron deficient than corresponding porphyrin moieties. It can also be noticed that polymers I and II exhibit a significant difference. The quantum yield of photogeneration of charge carriers in polymer II is much higher than that of polymer I. The only difference between these two polymers is that polymer II contains Zn porphyrin units and polymer I contains Cu porphyrin. It seems that the unpaired spin in the  $\text{Cu}^{2+}$  center played a crucial role. One possible reason is that the spin may facilitate the relaxation of the excited states through spin-orbital interaction. This will certainly reduce the quantum yield for the charge generation. The second reason is that the Cu porphyrin is less stable under laser light, possibly due to more facile photosensitization of single oxygen by copper porphyrin. The fact that similar behavior was observed in carefully sealed samples indicates that the spin effect may be the main effect for the differences in physical properties. The effect of metal ions was also observed on PR performances of polymers.

The PR properties of our polymers were examined by two-beam coupling (2BC) experiments, where two coherent laser beams (632.8 nm, 10 mW, *p*-polarized) intersected upon the PR sample with a cross-angle of  $7.5^\circ$  to generate a holographic grating. The unique feature of the PR effect, which distinguishes itself from many other mechanisms that may result in refractive index grating, is the nonlocal nature of the grating, *i.e.* the spatial phase shift between the incident light intensity pattern and the refractive index modulation.<sup>1, 2(a)</sup> This gives rise to an asymmetric energy exchange between the two beams, characterized by 2BC gain coefficient,  $\Gamma$ . This optical gain coefficient is proportional to the space-charge field induced by the separated charges. As shown in Fig. 2, the gain coefficients strongly depend on the applied field and exhibit trends well correlated with the photoconductivity results.<sup>12b</sup> At the field strength of 60 V/μm, gain coefficients for polymer I, II and III are 12, 65.7 and 103.5  $\text{cm}^{-1}$  respectively, while the absorption coefficient ( $\alpha$ ) was determined to be 20, 12.4 and 37  $\text{cm}^{-1}$ . Thus, net

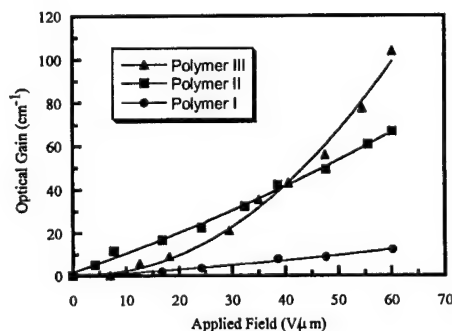


Figure 2. Field dependence of 2BC gain coefficient for polymer I – III.

optical gain coefficients ( $\Gamma\alpha$ ) of 53.3 and 66.5 cm<sup>-1</sup> were obtained in polymer **II** and **III**. For polymer **IV**, there is no sign of photorefractivity observed in 2BC experiments at 632 nm. Thus, both Zn Pc and Porphyrin complexes are good photosensitizer for PR process in these polymers. Complexes contains unpaired spins should be avoided.

The influence of photoconductivity was also reflected in the dynamic of holographic grating in degenerated four-wave mixing (DFWM) experiments, where the formation of the index grating was probed by a weak, *p*-polarized reading beam (632.8 nm). The achieved diffraction efficiencies for polymer **II** and **III** were 13.0 and 17.8 %, respectively. The response times were observed to decrease with the increase of the applied field and were determined to be 8.3, 4.7 and 0.45 s for polymer **I**, **II** and **III**, respectively, at a field strength of 60 V/ $\mu$ m and a light power of 0.83 W/cm<sup>2</sup>. This trend is consistent with the quantum yield results and is also understandable. High quantum yield means fast rate to build up a static space-charge field necessary for PR effect.

#### D. Photorefractive Effects and Structure/Property Correlation of Oligothiophenes Functionalized With Nonlinear Optical Chromophores

A photorefractive (PR) material possesses the ubiquitous ability to modulate its index of refraction under inhomogeneous illumination by low intensity light. This property can find wide applications in such areas as high-speed information processing, real-time optical data storage, three-dimensional holographic light processing and phase conjugation.<sup>1</sup> In a PR material, two types of physical properties must exist simultaneously: photoconductivity and electro-optic response. The photoinduced refractive index modulation arises from the linear electro-optic effect (Pockel effect) of the nonlinear optical (NLO) chromophore in response to the internal space-charge field within a photoconducting medium. Recently, significant effort has been devoted to the study of novel PR polymeric and oligomeric systems because of their easy processibility, versatility for structural modifications and operationally low cost compared to their inorganic counterparts.<sup>2-10</sup> Our group has a long-standing interest in the rational design and study of fully functionalized PR polymers and molecules, and has been successful in identifying novel PR materials with long-term stability and without phase separation due to incompatibility between their constituent functional components.<sup>5,6</sup> Recently, we described the PR properties of a multifunctional oligo(3-alkylthiophene) molecule containing a pendant NLO chromophore.<sup>11</sup> In this PR molecular system, conjugated oligothiophene backbone plays the role of the photoconductive component and gives rise to a photoinduced space charge field under inhomogeneous illumination. The pendant NLO chromophore was responsible for refractive index modulation.

In order to expand the scope of the methodologies available for constructing highly functionalized oligothiophene (OT) molecules and to correlate the PR properties with the conjugation chain length of the OT system, we report here a general strategy to the synthesis of a series of doubly end-capped, regioregular head-to-tail coupled oligo(3-alkylthiophenes) bearing novel NLO chromophores. One of the salient structural features of these OT molecules is the presence of  $\beta$ -branched side chains on the 3-position of each of the constituting thiophene unit, resulting in a stereo-random mixture of stereoisomers. These stereoisomers are beneficial to prepare amorphous materials possessing low  $T_g$  values that can be solution cast to provide transparent thick films with high optical quality and long-term stability. Detailed physical studies revealed their interesting features and furnished with insightful structure/property correlation.

#### Experimental Section

Unless otherwise specified, all chemicals were purchased from commercial suppliers and used without further purification. All reactions were conducted under a nitrogen atmosphere unless otherwise specified. Tetrahydrofuran (THF) was distilled over sodium/benzophenone ketyl under a nitrogen atmosphere immediately prior to use. <sup>1</sup>H NMR spectra were recorded at 400 or 500 MHz on Brüker DRX-400 or Brüker DRX-500 spectrometers, respectively. <sup>13</sup>C NMR spectra at 100 or 125 MHz were obtained on Brüker DRX-400 or DRX-500 spectrometers, respectively. CDCl<sub>3</sub> was used as the solvent to obtain all the <sup>1</sup>H and <sup>13</sup>C NMR spectra. <sup>1</sup>H chemical shift ( $\delta$ ) are reported in ppm downfield from tetramethylsilane. <sup>13</sup>C chemical shift ( $\delta$ ) are reported using the diagnostic 77.0 ppm CDCl<sub>3</sub> resonance as an internal reference. Differential scanning calorimetry was performed on a DSC-10 system from TA Instruments under a nitrogen atmosphere at a heating rate of 10 °C min<sup>-1</sup>. UV-vis spectral analysis was performed with a Shimadzu UV-2401PC spectrophotometer. Cyclic voltammetry was performed with an EG&G Princeton Applied Research model 273 potentiostat/galvanostat using a Bioanalytical electrochemical analyzer in a three-electrode cell equipped with a platinum disk working electrode, a platinum wire counter electrode and, a Ag/Ag<sup>+</sup> reference electrode. The supporting electrolyte used was 0.1 M tetrabutylammonium tetrafluoroborate (TBAB) in dichloromethane. The scan rate was adjusted to 100 mV s<sup>-1</sup> and data analysis was



accomplished by using the EG&G M270 software. All potentials were calibrated against ferrocene/ferrocenium ( $\text{Fc}/\text{Fc}^+$ ) couple after each experiment.

The films for two-beam coupling and four-wave mixing experiments were prepared by sandwiching the materials between two indium-tin oxide (ITO) covered glass substrates. The thickness of the film was maintained at 127  $\mu\text{m}$  with the help of a polyimide spacer. Two-beam coupling experiments were performed using a He-Ne  $p$ -polarized laser (632.8 nm, 30 mW) as the light source. The laser beam was split into two beams with equal intensity, which were intersected in the film with an incident-crossing angle of 7.5°. The film normal was tilted at an angle of 53° with respect to the symmetric axis of the two writing beams. The transmitted intensities of the two beams were monitored by two calibrated diode detectors and the measurements were controlled by a computer. The electric field induced birefringence and electro-optic coefficient  $r_{33}$  were measured using an ellipsometric method in a transmission mode. The sample normal was tilted at 45° with respect to the incident light. The polarization of the incident light was 45° with respect to the incident plane. A high DC voltage was applied to the film to align the NLO chromophore, while an AC voltage was coupled onto the film to modulate the phase retardation contributed from the NLO chromophore. The transmitted light consisted of a DC and an AC component. The former is a result of field birefringence, while the latter is the contribution of the NLO effect ( $r_{33}$ ). The frequency of the AC voltage was high enough to ensure that only  $\pi$ -electrons were able to follow the modulation. All the measurements were automatically controlled by a computer. Diffraction efficiency was measured by DFWM experiment. In a DFWM experiment, two  $s$ -polarized laser beams (632.8 nm) of comparable intensities intersected in the film to write the index grating, and a weak  $p$ -polarized beam (probe beam) counter-propagating to one of the writing beams was used to read the index grating formed in the material. The diffracted light intensity of the probe beam was detected with a lock-in amplifier, and the diffraction efficiency,  $\eta$ , was calculated as the ratio of the intensities of the diffracted beam to the incident reading beam.

**3-(2'-Ethylhexyl)-2-trimethylsilylthiophene (1c).** To a stirred solution of 2-bromo-3-(2'-ethylhexyl)thiophene **1b** (27.53 g, 100.02 mmol) in dry  $\text{Et}_2\text{O}$  (225 mL) at -78 °C was added dropwise a solution of  $n$ -BuLi (2.5 M in hexanes, 48.00 mL, 120.00 mmol) over 30 min. The resulting yellow solution was stirred at -78 °C for a further 20 min and chlorotrimethylsilane (22.85 mL, 180.04 mmol) was added dropwise over 10 min and the mixture was warmed to room temperature over 1.5 h. The resulting mixture was poured into water (400 mL) and extracted with  $\text{Et}_2\text{O}$  ( $2 \times 100$  mL). The combined organic extracts were washed with brine (100 mL), dried ( $\text{Na}_2\text{SO}_4$ ), filtered and the filtrate concentrated under reduced pressure. The residual liquid was purified by distillation under high vacuum to afford trimethylsilyl thiophene **1c** (18.80 g, 70.01 mmol, 70%) as a colorless liquid (b.p. 130-134 °C/1 mmHg).  $^1\text{H}$  NMR (500 MHz,  $\text{CDCl}_3$ ):  $\delta$  0.33 (s, 9 H), 0.86 (t,  $J = 7.4$  Hz, 6 H), 1.21-1.28 (m, 8 H), 1.60-1.64 (m, 1 H), 2.60 (d,  $J = 7.4$  Hz, 2 H), 7.02 (d,  $J = 4.7$  Hz, 1 H), 7.44 (d,  $J = 4.7$  Hz, 1 H).

**4,3'-Di(2'-ethylhexyl)-5-trimethylsilyl-2,2'-bithiophene (2a).** To a stirred solution of **1c** (6.837 g, 25.46 mmol) and  $N,N,N',N'$ -tetramethylethylenediamine (TMEDA, 3.842 mL, 25.46 mmol) in dry THF (25 mL) at 25 °C was added dropwise a solution of  $n$ -BuLi (2.5 M in hexanes, 11.20 mL, 28.00 mmol) over 20 min. The resulting mixture was heated under reflux for 45 min and stirred at room temperature for a further 30 min. The solution was transferred via cannula into a solution of anhydrous  $\text{ZnCl}_2$  (3.817 g, 28.00 mmol) in dry THF (8 mL) at 25 °C over 25 min. The resulting mixture was stirred at room temperature for 1 h and the solution transferred via cannula into a mixture of **1b** (6.372 g, 23.15 mmol) and  $\text{Pd}(\text{PPh}_3)_4$  (0.295 g, 0.255 mmol) in dry THF (5 mL) over 25 min. The resulting mixture was heated under reflux for 24 h. Upon cooling to room temperature, the reaction mixture was hydrolyzed with water (50 mL), diluted with  $\text{Et}_2\text{O}$  (70 mL) and filtered through a pad of Celite. The aqueous layer was extracted with  $\text{Et}_2\text{O}$  ( $2 \times 50$  mL) and the combined organic extracts were washed with brine (30 mL), dried ( $\text{Na}_2\text{SO}_4$ ) and filtered. The filtrate was concentrated under reduced pressure and the residual liquid filtered through a pad of silica gel (hexanes, 150 mL) and distilled under high vacuum to remove unreacted starting materials **1b** and **1c** to afford **2a** (55%; contaminated with 8% of 2,5-bis(trimethylsilyl)bithiophene **2b**) as a yellow liquid.  $^1\text{H}$  NMR (500 MHz,  $\text{CDCl}_3$ ):  $\delta$  0.34 (s, 9 H), 0.84 (t,  $J = 7.4$  Hz, 6 H), 0.88 (t,  $J = 7.4$  Hz, 6 H), 1.23-1.34 (m, 16 H), 1.57-1.63 (m, 2 H), 2.57 (d,  $J = 7.5$  Hz, 2 H), 2.69 (d,  $J = 7.3$  Hz, 2 H), 6.88 (d,  $J = 5.2$  Hz, 1 H), 7.01 (s, 1 H), 7.13 (d,  $J = 5.2$  Hz, 1 H);  $^{13}\text{C}$  NMR ( $\text{CDCl}_3$ )  $\delta$  0.6, 10.7, 11.0, 14.1, 23.1, 25.7, 25.8, 28.7, 28.9, 32.6, 32.7, 33.3, 35.9, 40.3, 40.8, 123.1, 129.7, 130.6, 131.6, 133.7, 138.4, 139.8, 149.6.

**3,4'-Di(2'-ethylhexyl)-5-tributylstannyl-5'-trimethylsilyl-2,2'-bithiophene (2c).** To a stirred solution of **2a** (90% purity, 5.787 g, 11.25 mmol) and TMEDA (1.868 mL, 12.38 mmol) in dry THF (16 mL) at 0 °C was added dropwise a solution of  $n$ -BuLi (2.5 M in hexanes, 6.30 mL, 15.75 mmol) over 5 min. The resulting solution was stirred at 0 °C for 20 min and warmed to room temperature over 30 min. The mixture was cooled to 0 °C and tributyltin chloride (4.425 mL, 16.31 mmol) was added dropwise over 2 min. The resulting mixture was stirred at 0 °C for 10 min, warmed to room temperature over 20 min, poured into water (50 mL) and extracted with  $\text{Et}_2\text{O}$  (50 mL). The combined organic extracts were washed with saturated  $\text{NH}_4\text{Cl}$  ( $2 \times 40$  mL), dried ( $\text{Na}_2\text{SO}_4$ ), filtered and the filtrate concentrated under reduced pressure to afford organostannane **2c** (100%) as a yellow liquid. This crude product was dried under vacuum and directly used in the Stille coupling reaction without further purification.

**General procedure for the Stille cross-coupling reactions of bromides or iodide with organostannane (2c).**

**3,4'-Di(2'-ethylhexyl)-5-[( $p$ -methoxycarbonyl)phenyl]-5'-trimethylsilyl-2,2'-bithiophene (3a).** A mixture of the crude organostannane bithiophene **2c** (16.24 g, 21.60 mmol), methyl 4-iodobenzoate (4.92 g, 18.78 mmol),  $\text{Pd}(\text{PPh}_3)_2\text{Cl}_2$  (0.198 g, 0.282 mmol) and triphenylphosphine (0.148 g, 0.564 mmol) in toluene (120 mL) was heated at 120-125 °C for 8 h. Upon cooling to room temperature, excess solvent was removed under reduced pressure and the residue purified by flash chromatography on silica gel (hexanes/toluene = 80/1 gradient to 2/1) to afford ester **3a** (10.09 g, 16.90 mmol, 90%) as a yellow liquid.  $^1\text{H}$  NMR (500 MHz,  $\text{CDCl}_3$ ):  $\delta$  0.36 (s, 9 H), 0.86 (t,  $J = 7.3$  Hz, 6 H), 0.88 (t,  $J = 7.2$  Hz, 6 H), 1.26-1.36 (m, 16 H), 1.64-1.68 (m, 2 H), 2.58 (d,  $J = 7.4$  Hz, 2 H), 2.72 (t,  $J = 6.5$  Hz, 2 H), 3.93 (s, 3 H), 7.08 (s, 1 H), 7.22 (s, 1 H), 7.65 (d,  $J = 8.3$  Hz, 2 H), 8.03 (d,  $J = 8.2$  Hz, 2 H);  $^{13}\text{C}$  NMR (100 MHz,  $\text{CDCl}_3$ ):  $\delta$  0.6, 10.7, 11.0, 14.1, 23.1, 23.1, 25.7, 25.8, 28.7, 28.9, 32.5, 32.7, 33.6, 35.9, 40.2, 40.8, 52.1, 125.0, 128.1, 128.5, 129.8, 130.2, 132.9, 134.3, 138.5, 139.3, 139.5, 139.7, 149.8, 166.8.

**General procedure for the bromination of trimethylsilyl-substituted oligothiophene esters.**

**5-Bromo-3',4-Di(2''-ethylhexyl)-5'-[(p-methoxycarbonyl)phenyl]-2,2'-bi-thiophene (3b).** To a stirred solution of trimethylsilyl bithiophene **3a** (10.39 g, 17.40 mmol) in chloroform-acetic acid (1/1, 60 mL) at 0 °C was added *N*-bromosuccinimide (3.034 g, 17.05 mmol, 0.98 equiv) in one portion. The resulting mixture was stirred at 0 °C for 1 h and warmed to room temperature and stirred for a further 3 h. The mixture was poured into water (75 mL) and washed with 5% aqueous NaHCO<sub>3</sub> solution (2 × 50 mL), dried (Na<sub>2</sub>SO<sub>4</sub>) and filtered. The filtrate was concentrated under reduced pressure and the residue purified by flash chromatography on silica gel (hexanes/toluene = 25/1 gradient to 2/1) to afford bromo bithiophene ester **3b** (10.10 g, 16.73 mmol, 98%) as a yellow liquid. <sup>1</sup>H NMR (400 MHz, CDCl<sub>3</sub>): δ 0.86 (t, *J* = 7.2 Hz, 6 H), 0.89 (t, *J* = 7.2 Hz, 6 H), 1.25-1.34 (m, 16 H), 1.64-1.68 (m, 2 H), 2.50 (d, *J* = 7.2 Hz, 2 H), 2.66 (t, *J* = 7.3 Hz, 2 H), 3.93 (s, 3 H), 6.82 (s, 1 H), 7.21 (s, 1 H), 7.63 (d, *J* = 8.5 Hz, 2 H), 8.03 (d, *J* = 8.5 Hz, 2 H); <sup>13</sup>C NMR (100 MHz, CDCl<sub>3</sub>): δ 10.7, 10.8, 14.1, 23.0, 25.7, 28.6, 28.8, 32.5, 33.5, 33.7, 39.9, 40.2, 52.1, 109.7, 125.1, 127.8, 127.8, 128.7, 130.2, 131.7, 135.0, 138.2, 140.3, 140.5, 141.7, 166.7.

**Trimethylsilyl quaterthiophene ester (4a).** Following the general procedure described for the synthesis of **3a**, a mixture of **2c** (15.66 g, 20.83 mmol), bromo bithiophene **3b** (10.48 g, 17.36 mmol) and Pd(PPh<sub>3</sub>)<sub>4</sub> (0.201 g, 0.174 mmol) in toluene (100 mL) at 120-125 °C for 8 h provided quaterthiophene ester **4a** (12.15 g, 12.33 mmol, 71%) as a viscous yellow liquid. <sup>1</sup>H NMR (500 MHz, CDCl<sub>3</sub>): δ 0.36 (s, 9 H), 0.85-0.90 (m, 24 H), 1.27-1.37 (m, 32 H), 1.62-1.68 (m, 4 H), 2.58 (d, *J* = 7.4 Hz, 2 H), 2.72-2.78 (m, 6 H), 3.93 (s, 3 H), 6.93 (s, 1 H), 6.97 (s, 1 H), 7.05 (s, 1 H), 7.23 (s, 1 H), 7.65 (d, *J* = 8.4 Hz, 2 H), 8.04 (d, *J* = 8.4 Hz, 2 H); <sup>13</sup>C NMR (100 MHz, CDCl<sub>3</sub>): δ 0.6, 10.7, 11.0, 14.1, 23.1, 25.7, 25.8, 28.7, 28.9, 32.6, 32.6, 32.7, 33.5, 33.6, 33.7, 35.9, 40.2, 40.8, 52.1, 125.0, 128.1, 128.6, 129.5, 129.6, 129.8, 130.3, 131.6, 131.8, 132.4, 133.1, 133.3, 133.9, 138.3, 138.6, 138.9, 139.4, 139.9, 149.7, 166.7.

**Bromo quaterthiophene ester (4b).** Following the general procedure described for the synthesis of **3b**, a mixture of trimethylsilyl quaterthiophene **4a** (9.60 g, 9.74 mmol) and *N*-bromosuccinimide (1.73 g, 9.72 mmol, 1.00 equiv) in chloroform-acetic acid (1/1, 60 mL) at 0 °C provided bromo quaterthiophene ester **4b** (8.70 g, 8.77 mmol, 90%) as a viscous yellow liquid. <sup>1</sup>H NMR (500 MHz, CDCl<sub>3</sub>): δ 0.85-0.91 (m, 24 H), 1.27-1.34 (m, 32 H), 1.60-1.70 (m, 4 H), 2.50 (d, *J* = 7.2 Hz, 2 H), 2.65 (d, *J* = 7.3 Hz, 2 H), 2.70-2.74 (m, 4 H), 3.93 (s, 3 H), 6.79 (s, 1 H), 6.92 (s, 1 H), 6.97 (s, 1 H), 7.23 (s, 1 H), 7.65 (d, *J* = 8.3 Hz, 2 H), 8.04 (d, *J* = 8.3 Hz, 2 H).

**Bromo quaterthiophene carboxylic acid (4c).** A mixture of the ester **4b** (2.08 g, 2.10 mmol) and aqueous sodium hydroxide (1 M, 3.25 mL) in ethanol (18 mL) and THF (14 mL) was heated at 95 °C for 6 h. After cooling to room temperature, excess solvent was removed under reduced pressure and the residue was cooled to 0 °C, acidified with 1 M hydrochloric acid (5.0 mL) and extracted with chloroform (2 × 30 mL). The combined organic extracts were dried (Na<sub>2</sub>SO<sub>4</sub>), filtered and the filtrate concentrated under reduced pressure. The residue was purified by flash chromatography on silica gel (hexanes/ethyl acetate = 8/1 gradient to 2/1) to provide acid **4c** (1.351 g, 1.38 mmol, 66%) as a viscous yellow liquid. <sup>1</sup>H NMR (400 MHz, CDCl<sub>3</sub>): δ 0.85-0.91 (m, 24 H), 1.27-1.34 (m, 32 H), 1.60-1.70 (m, 4 H), 2.50 (d, *J* = 7.2 Hz, 2 H), 2.65 (d, *J* = 7.3 Hz, 2 H), 2.70-2.74 (m, 4 H), 6.79 (s, 1 H), 6.92 (s, 1 H), 6.97 (s, 1 H), 7.23 (s, 1 H), 7.69 (d, *J* = 8.4 Hz, 2 H), 8.11 (d, *J* = 8.4 Hz, 2 H).

**NLO chromophore-containing bromo quaterthiophene (4d).**

A mixture of acid **4c** (1.351 g, 1.38 mmol), chromophore **7** (0.708 g, 1.51 mmol) and triphenylphosphine (0.543 g, 2.07 mmol) in dry THF (16 mL) at 0 °C was added dropwise a solution of diisopropyl azodicarboxylate (DIAD, 0.408 mL, 2.07 mmol) in dry THF (2 mL) over 3 min. After stirring at 0 °C for 5 min, the resulting mixture was warmed to room temperature and stirred for a further 1.5 h. The mixture was concentrated under reduced pressure and the residue purified by flash chromatography on silica gel (hexanes/ethyl acetate = 8/1 gradient to 6/1) to provide NLO chromophore-containing quaterthiophene **4d** (1.79 g, 1.25 mmol, 91%) as a viscous red liquid. <sup>1</sup>H NMR (500 MHz, CDCl<sub>3</sub>): δ 0.84-0.93 (m, 27 H), 1.24-1.38 (m, 42 H), 1.54-1.70 (m, 10 H), 2.50 (d, *J* = 7.2 Hz, 2 H), 2.65 (d, *J* = 7.3 Hz, 2 H), 2.72 (m, 4 H), 3.38-3.44 (m, 4 H), 4.35 (t, *J* = 6.5 Hz, 2 H), 6.73 (d, *J* = 9.2 Hz, 2 H), 6.79 (s, 1 H), 6.92 (s, 1 H), 6.96 (s, 1 H), 7.22 (s, 1 H), 7.65 (d, *J* = 8.4 Hz, 2 H), 7.77 (dd, *J* = 7.3 Hz, 7.8 Hz, 1 H), 7.84 (dd, *J* = 7.5 Hz, 7.8 Hz, 1 H), 7.92 (s, 1 H), 8.02 (d, *J* = 9.4 Hz, 2 H), 8.00-8.07 (m, 2 H), 8.04 (d, *J* = 8.4 Hz, 2 H).

**Trimethylsilyl sexithiophene ester (5a).** Following the general procedure, a mixture of **2c** (2.44 g, 3.24 mmol), bromo quaterthiophene **4b** (1.787 g, 1.80 mmol) and Pd(PPh<sub>3</sub>)<sub>4</sub> (0.052 g, 0.045 mmol) in toluene (16 mL) at 115-120 °C for 15 h provided sexithiophene ester **5a** (1.51 g, 1.10 mmol, 61%) as a viscous yellow liquid. <sup>1</sup>H NMR (500 MHz, CDCl<sub>3</sub>): δ 0.36 (s, 9 H), 0.85-0.91 (m, 36 H), 1.27-1.38 (m, 48 H), 1.62-1.70 (m, 6 H), 2.58 (d, *J* = 7.4 Hz, 2 H), 2.72-2.75 (m, 10 H), 3.93 (s, 3 H), 6.93 (s, 1 H), 6.94 (s, 1 H), 6.95 (s, 1 H), 6.98 (s, 1 H), 7.05 (s, 1 H), 7.23 (s, 1 H), 7.65 (d, *J* = 8.4 Hz, 2 H), 8.04 (d, *J* = 8.4 Hz, 2 H); <sup>13</sup>C NMR (100 MHz, CDCl<sub>3</sub>): δ 0.6, 10.8, 11.0, 14.2, 22.6, 23.1, 23.1, 25.7, 25.8, 28.8, 28.9, 31.6, 32.6, 32.7, 33.5, 33.6, 33.7, 35.9, 40.2, 40.8, 52.1, 125.0, 128.1, 128.6, 129.5, 129.6, 129.8, 130.3, 131.3, 131.4, 131.7, 132.4, 133.2, 133.4, 133.4, 133.9, 138.3, 138.6, 138.9, 139.0, 139.0, 139.4, 140.0, 149.7, 166.7.

**Bromo sexithiophene ester (5b).** Following the general procedure, a mixture of trimethylsilyl sexithiophene **5a** (3.696 g, 2.69 mmol) and *N*-bromosuccinimide (0.464 g, 2.61 mmol, 0.97 equiv) in chloroform-acetic acid (1/1, 40 mL) at 0 °C provided bromo sexithiophene ester **5b** (3.53 g, 2.56 mmol, 95%) as a viscous orange-yellow liquid. <sup>1</sup>H NMR (400 MHz, CDCl<sub>3</sub>): δ 0.84-0.92 (m, 36 H), 1.29-1.38 (m, 48 H), 1.60-1.75 (m, 6 H), 2.50 (d, *J* = 7.2 Hz, 2 H), 2.65 (d, *J* = 7.3 Hz, 2 H), 2.70-2.75 (m, 8 H), 3.93 (s, 3 H), 6.79 (s, 1 H), 6.92 (s, 1 H), 6.93 (s, 1 H), 6.94 (s, 1 H), 6.98 (s, 1 H), 7.23 (s, 1 H), 7.65 (d, *J* = 8.5 Hz, 2 H), 8.04 (d, *J* = 8.5 Hz, 2 H).

**Bromo sexithiophene carboxylic acid (5c).** A mixture of the ester **5b** (3.372 g, 2.44 mmol) and aqueous sodium hydroxide (1 M, 6.10 mL) in ethanol (25 mL) and THF (25 mL) was heated under reflux for 16 h. After cooling to room temperature, excess solvent was removed under reduced pressure and the residue was cooled to 0 °C, acidified with 1 M hydrochloric acid (11 mL) and extracted with chloroform (2 × 40 mL). The combined organic extracts were dried (Na<sub>2</sub>SO<sub>4</sub>), filtered and the filtrate concentrated under reduced pressure. The residue was purified by flash chromatography on silica gel (hexanes/ethyl acetate = 8/1 gradient to 2/1) to provide acid **5c** (3.00 g, 2.19 mmol, 90%) as a viscous orange-yellow liquid. <sup>1</sup>H NMR (500 MHz, CDCl<sub>3</sub>): δ 0.86-0.91 (m, 36 H), 1.27-1.36 (m, 48 H), 1.60-1.75 (m, 6 H), 2.50 (d, *J* = 7.2 Hz, 2 H), 2.65 (d, *J* = 7.3 Hz, 2 H), 2.71-2.76 (m, 8 H), 6.79 (s, 1 H), 6.92 (s, 1 H), 6.94 (s, 1 H), 6.95 (s, 1 H), 6.99 (s, 1 H), 7.26 (s, 1 H), 7.69 (d, *J* = 8.4 Hz, 2 H), 8.11 (d, *J* = 8.4 Hz, 2 H).



**NLO chromophore-containing bromo sexithiophene (5d).** A mixture of acid **5c** (3.00 g, 2.19 mmol), chromophore **7** (1.20 g, 2.56 mmol) and triphenylphosphine (0.863 g, 3.29 mmol) in dry THF (20 mL) at 0 °C was added dropwise a solution of diethyl azodicarboxylate (DEAD, 0.55 mL, 3.49 mmol) in dry THF (3 mL) over 3 min. After stirring at 0 °C for 5 min, the resulting mixture was warmed to room temperature and stirred for a further 30 min. The mixture was concentrated under reduced pressure and the residue purified by flash chromatography on silica gel (hexanes/ethyl acetate = 8/1 gradient to 6/1) to provide NLO chromophore-containing sexithiophene **5d** (3.11 g, 1.71 mmol, 78%) as a viscous red liquid. <sup>1</sup>H NMR (400 MHz, CDCl<sub>3</sub>): δ 0.86-0.91 (m, 39 H), 1.24-1.36 (m, 58 H), 1.60-1.75 (m, 12 H), 2.50 (d, *J* = 7.2 Hz, 2 H), 2.65 (d, *J* = 7.3 Hz, 2 H), 2.71-2.75 (m, 8 H), 3.38-3.42 (m, 4 H), 4.35 (t, *J* = 6.4 Hz, 2 H), 6.73 (d, *J* = 9.2 Hz, 2 H), 6.79 (s, 1 H), 6.92 (s, 1 H), 6.94 (s, 1 H), 6.94 (s, 1 H), 6.97 (s, 1 H), 7.23 (s, 1 H), 7.66 (d, *J* = 8.5 Hz, 2 H), 7.77 (ddd, *J* = 1.0 Hz, 7.5 Hz, 7.5 Hz, 1 H), 7.84 (ddd, *J* = 1.1 Hz, 7.5 Hz, 7.5 Hz, 1 H), 7.92 (s, 1 H), 8.01-8.07 (m, 2 H), 8.02 (d, *J* = 9.2 Hz, 2 H), 8.04 (d, *J* = 8.5 Hz, 2 H).

**Trimethylsilyl octithiophene ester (6a).** Following the general procedure, a mixture of **2c** (2.18 g, 2.90 mmol), bromo sexithiophene **5b** (2.50 g, 1.81 mmol) and Pd(PPh<sub>3</sub>)<sub>4</sub> (0.052 g, 0.045 mmol) in toluene (20 mL) at 115-120 °C for 10 h provided octithiophene ester **6a** (1.69 g, 0.96 mmol, 53%) as a viscous orange-yellow liquid. <sup>1</sup>H NMR (400 MHz, CDCl<sub>3</sub>): δ 0.36 (s, 9 H), 0.87-0.90 (m, 48 H), 1.26-1.39 (m, 64 H), 1.62-1.72 (m, 8 H), 2.58 (d, *J* = 7.4 Hz, 2 H), 2.69-2.76 (m, 14 H), 3.94 (s, 3 H), 6.92 (s, 1 H), 6.93 (s, 1 H), 6.94 (s, 2 H), 6.95 (s, 1 H), 6.98 (s, 1 H), 7.05 (s, 1 H), 7.24 (s, 1 H), 7.65 (d, *J* = 8.5 Hz, 2 H), 8.04 (d, *J* = 8.5 Hz, 2 H); <sup>13</sup>C NMR (125 MHz, CDCl<sub>3</sub>): δ 0.6, 10.8, 11.0, 14.1, 14.2, 22.7, 23.1, 23.1, 25.8, 25.9, 28.8, 28.9, 31.6, 32.6, 32.6, 32.7, 33.5, 33.6, 33.7, 35.9, 40.2, 40.2, 40.8, 52.1, 125.1, 128.1, 128.6, 129.5, 129.5, 129.6, 129.8, 130.3, 131.1, 131.2, 131.4, 131.7, 132.4, 133.2, 133.4, 133.5, 133.9, 138.3, 138.6, 138.9, 139.0, 139.0, 139.1, 139.1, 139.4, 140.0, 140.0, 149.7, 166.7.

**Fully functionalized (10).** Following the general procedure, a mixture of **4d** (2.20 g, 1.54 mmol), organostannane **8b** (2.18 g, 2.46 mmol) and Pd(PPh<sub>3</sub>)<sub>4</sub> (0.053 g, 0.046 mmol) in toluene (20 mL) at 110-115 °C for 10 h provided the fully functionalized **10** (1.80 g, 0.92 mmol, 60%) as an amorphous red solid. <sup>1</sup>H NMR (500 MHz, CDCl<sub>3</sub>): δ 0.24 (s, 6 H), 0.88-0.92 (m, 39 H), 1.00 (s, 9 H), 1.21-1.40 (m, 58 H), 1.55-1.71 (m, 12 H), 2.58 (d, *J* = 7.2 Hz, 2 H), 2.74 (d, *J* = 7.0 Hz, 10 H), 3.39-3.45 (m, 4 H), 4.36 (t, *J* = 6.5 Hz, 2 H), 6.74 (d, *J* = 9.2 Hz, 2 H), 6.88 (d, *J* = 8.5 Hz, 2 H), 6.95 (s, 2 H), 6.96 (s, 1 H), 6.97 (s, 1 H), 6.98 (s, 1 H), 7.24 (s, 1 H), 7.32 (d, *J* = 8.5 Hz, 2 H), 7.66 (d, *J* = 8.4 Hz, 2 H), 7.77 (dd, *J* = 7.5 Hz, 7.6 Hz, 1 H), 7.84 (dd, *J* = 7.5 Hz, 7.5 Hz, 1 H), 7.93 (s, 1 H), 8.02 (d, *J* = 9.2 Hz, 2 H), 8.02-8.07 (m, 2 H), 8.04 (d, *J* = 8.4 Hz, 2 H); <sup>13</sup>C NMR (100 MHz, CDCl<sub>3</sub>): δ -4.5, 10.7, 10.7, 14.0, 14.1, 14.1, 22.6, 23.0, 23.1, 25.6, 25.6, 25.7, 25.9, 26.6, 26.7, 27.3, 28.6, 28.7, 28.7, 31.5, 32.5, 33.5, 33.5, 33.7, 40.1, 40.4, 51.1, 51.3, 64.7, 111.9, 117.9, 120.0, 120.9, 122.6, 124.1, 125.0, 127.4, 128.1, 128.7, 129.3, 129.4, 129.5, 129.7, 130.2, 130.6, 131.2, 131.4, 131.6, 132.3, 133.0, 133.0, 133.1, 133.3, 133.4, 133.5, 135.2, 137.5, 137.6, 138.2, 138.5, 138.5, 138.8, 138.9, 139.0, 139.9, 143.7, 144.8, 152.6, 155.1, 166.2, 178.6.

**Fully functionalized (11).** Following the general procedure, a mixture of **5d** (2.50 g, 1.37 mmol), organostannane **8b** (1.94 g, 2.19 mmol) and Pd(PPh<sub>3</sub>)<sub>4</sub> (0.047 g, 0.041 mmol) in toluene (18 mL) at 110-115 °C for 10 h provided the fully functionalized **11** (2.05 g, 0.88 mmol, 64%) as an amorphous red solid. <sup>1</sup>H NMR (500 MHz, CDCl<sub>3</sub>): δ 0.24 (s, 6 H), 0.86-0.90 (m, 51 H), 1.00 (s, 9 H), 1.21-1.43 (m, 74 H), 1.55-1.75 (m, 14 H), 2.58 (d, *J* = 7.1 Hz, 2 H), 2.74 (d, *J* = 7.0 Hz, 14 H), 3.39-3.45 (m, 4 H), 4.36 (t, *J* = 6.5 Hz, 2 H), 6.73 (d, *J* = 9.2 Hz, 2 H), 6.88 (d, *J* = 8.5 Hz, 2 H), 6.94 (s, 4 H), 6.96 (s, 1 H), 6.97 (s, 1 H), 6.98 (s, 1 H), 7.23 (s, 1 H), 7.32 (d, *J* = 8.5 Hz, 2 H), 7.66 (d, *J* = 8.5 Hz, 2 H), 7.77 (dd, *J* = 7.5 Hz, 7.6 Hz, 1 H), 7.84 (dd, *J* = 7.5 Hz, 7.5 Hz, 1 H), 7.92 (s, 1 H), 8.01-8.06 (m, 2 H), 8.02 (d, *J* = 9.2 Hz, 2 H), 8.04 (d, *J* = 8.4 Hz, 2 H); <sup>13</sup>C NMR (125 MHz, CDCl<sub>3</sub>): δ -4.4, 10.7, 10.7, 13.6, 14.0, 14.1, 14.1, 14.1, 17.2, 17.5, 18.2, 22.6, 23.0, 23.1, 25.6, 25.7, 25.7, 25.9, 26.6, 26.7, 26.7, 26.8, 27.3, 27.3, 27.8, 28.2, 28.6, 28.7, 28.7, 31.5, 32.5, 32.6, 33.5, 33.6, 33.7, 40.2, 40.4, 51.2, 51.4, 64.7, 111.9, 118.0, 120.0, 120.9, 122.7, 124.2, 125.0, 127.5, 128.1, 128.8, 128.8, 129.3, 129.4, 129.4, 129.5, 129.5, 129.8, 130.2, 130.6, 131.1, 131.2, 131.2, 131.4, 131.6, 132.3, 133.0, 133.1, 133.1, 133.4, 133.5, 133.6, 135.2, 137.6, 137.6, 138.3, 138.5, 138.5, 138.9, 138.9, 139.0, 139.0, 139.0, 140.0, 143.7, 144.9, 152.6, 155.1, 166.2, 178.7.

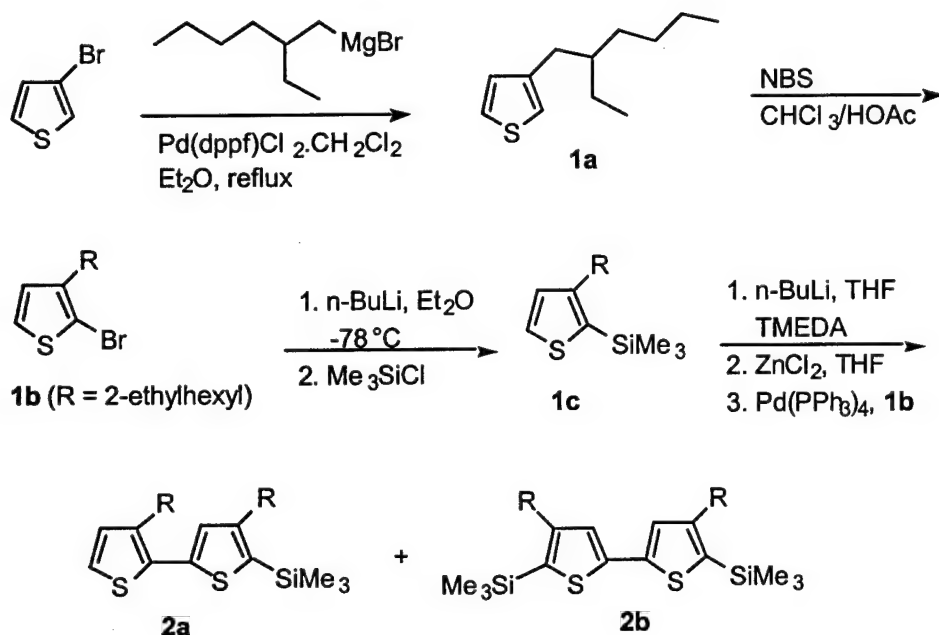
**Fully functionalized (12).** Following the general procedure, a mixture of **5d** (2.8 g, 1.54 mmol), organostannane **9b** (3.14 g, 2.46 mmol) and Pd(PPh<sub>3</sub>)<sub>4</sub> (0.053 g, 0.046 mmol) in toluene (18 mL) at 110-115 °C for 10 h provided the fully functionalized **12** (2.31 g, 0.85 mmol, 55%) as an amorphous red solid. <sup>1</sup>H NMR (500 MHz, CDCl<sub>3</sub>): δ 0.23 (s, 6 H), 0.87-0.94 (m, 63 H), 1.01 (s, 9 H), 1.20-1.45 (m, 90 H), 1.56-1.70 (m, 16 H), 2.56 (d, *J* = 7.1 Hz, 2 H), 2.73 (d, *J* = 6.7 Hz, 18 H), 3.39-3.44 (m, 4 H), 4.36 (t, *J* = 6.5 Hz, 2 H), 6.73 (d, *J* = 9.1 Hz, 2 H), 6.87 (d, *J* = 8.5 Hz, 2 H), 6.94 (s, 7 H), 6.96 (s, 1 H), 6.97 (s, 1 H), 7.23 (s, 1 H), 7.31 (d, *J* = 8.5 Hz, 2 H), 7.66 (d, *J* = 8.4 Hz, 2 H), 7.77 (dd, *J* = 7.4 Hz, 7.6 Hz, 1 H), 7.84 (dd, *J* = 7.4 Hz, 7.6 Hz, 1 H), 7.92 (s, 1 H), 8.02 (d, *J* = 9.1 Hz, 2 H), 8.04 (d, *J* = 8.5 Hz, 2 H), 8.02-8.07 (m, 2 H); <sup>13</sup>C NMR (100 MHz, CDCl<sub>3</sub>): δ -4.5, 10.7, 14.0, 14.0, 14.1, 22.6, 22.9, 23.1, 25.5, 25.6, 25.6, 25.7, 25.9, 26.6, 27.2, 28.6, 28.7, 31.5, 32.5, 33.5, 33.5, 33.7, 40.1, 40.4, 51.1, 51.3, 64.7, 111.8, 117.9, 120.0, 120.8, 122.7, 124.1, 124.9, 127.4, 128.1, 128.7, 128.7, 129.3, 129.4, 129.5, 129.7, 130.1, 130.5, 131.0, 131.0, 131.1, 131.1, 131.3, 131.6, 132.3, 133.0, 133.0, 133.1, 133.4, 133.5, 135.1, 137.5, 137.5, 138.2, 138.4, 138.8, 138.9, 138.9, 139.9, 143.7, 144.7, 152.5, 155.1, 166.1, 178.5.

## Results and Discussion

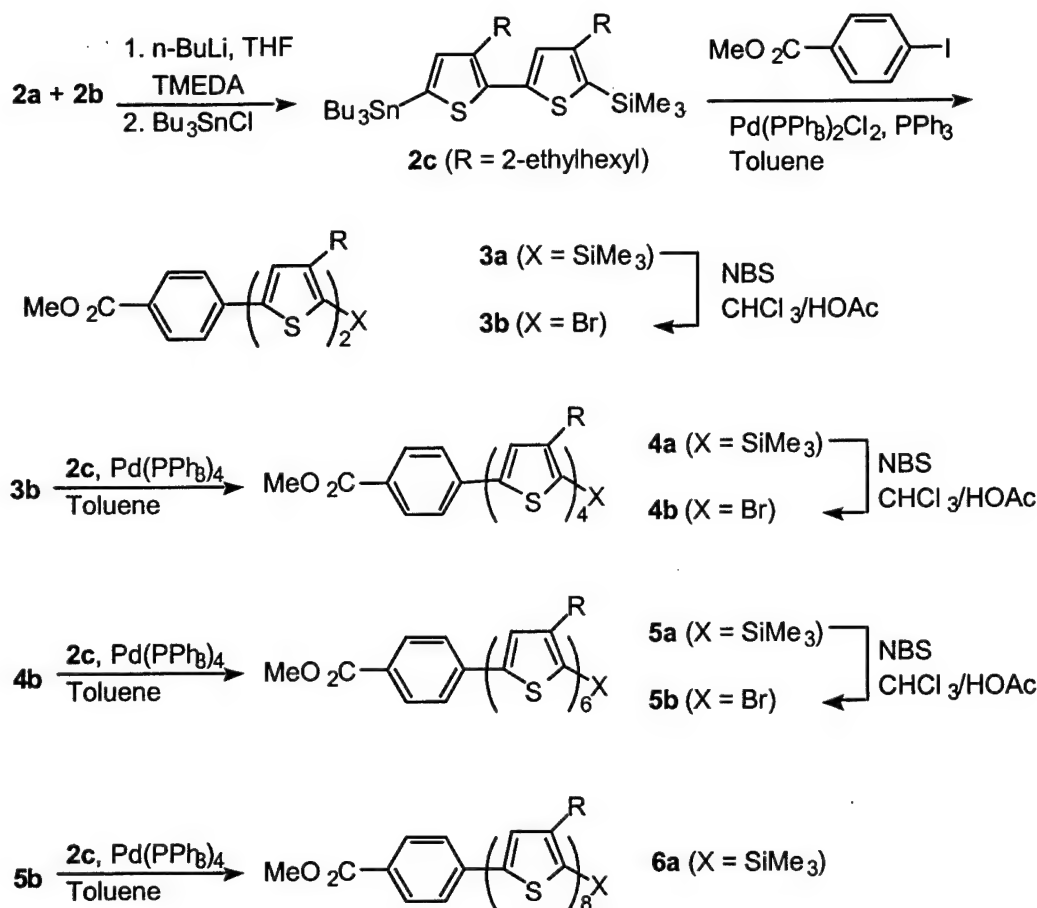
**Synthesis of Molecules.** It is now well established that the high regioregularity of the adjacent thiophene units in poly(3-alkylthiophenes) (PTs) substantially increases the conjugation length of the polymers due to minimization of steric interactions among the monomeric thiophene rings.<sup>12</sup> For instance, regioregular head-to-tail coupled PTs exhibit substantially higher electrical conductivities than that of the regiorandom analogues. Efficient methodologies for the preparation of highly regioregular head-to-tail

coupled PTs have been developed.<sup>13-16</sup> A few recent reports also documented the synthesis of regioregular head-to-tail coupled oligo(3-alkylthiophenes) in which chain growth involved stepwise addition of one or two thiophene units to the open terminal of an end-capped thiophene moiety employing either bromination-Stille coupling or iodination-Suzuki coupling reaction sequences.<sup>17-23</sup> In our target fully functionalized PR oligothiophene molecules, 10-12, both termini of the oligothiophene unit were capped with functionalized phenyl groups, thus allowing for the introduction of a NLO chromophore by standard coupling methodology. Disconnection of the target molecules reveals the convergent assembly of two complementary oligothiophene units through palladium-catalyzed cross-coupling reactions. The Stille reaction is utilized as the coupling method because of its remarkable tolerance for a variety of acid-base sensitive functional groups in the NLO chromophore. Efficient synthesis of the OT series necessitates the use of functionalized bithiophenes as the building molecule. The key building block, 5-trimethylsilyl-3',4-di(2''-ethylhexyl)-2,2'-bithiophene, **2a**, was prepared from the palladium-mediated Negishi cross-coupling of 2-bromo-3-(2'-ethylhexyl)thiophene **1b** with the organozinc reagent derived from 2-trimethylsilyl-3-(2'-ethylhexyl)thiophene **1c** (Scheme 1). The selective installation of a versatile

Scheme 1.

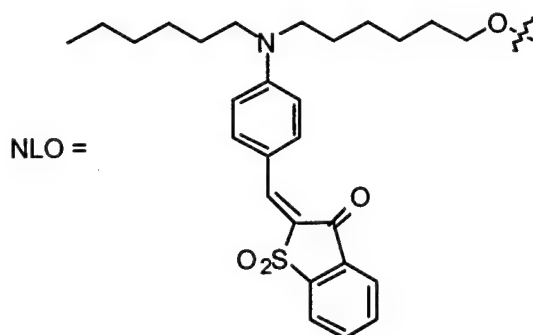
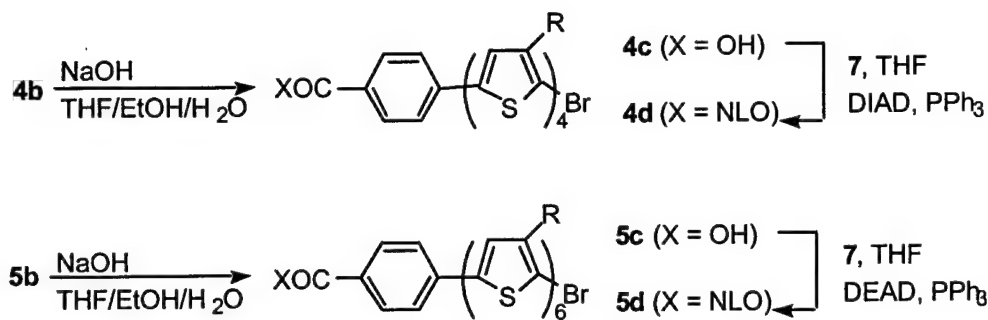


Scheme 2.

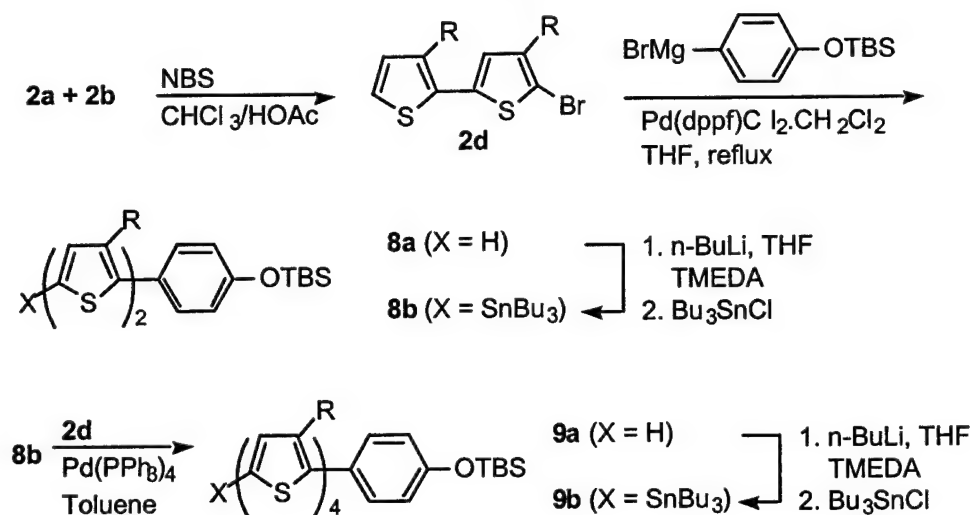


trimethylsilyl substituent on the reactive 5-position of **2a** proves to be critical in achieving complete regiocontrol in the buildup of the regioregular OT series. It is noted that the purified building block **2a** was accompanied by 5-8% of the symmetrical 5,5'-bis(trimethylsilyl)-4,4'-di(2''-ethylhexyl)-2,2'-bithiophene **2b**. The compound **2b** arises from homocoupling of the organometallic partner and is characterized by its diagnostic singlet absorption peak in the aromatic region at  $\delta$  7.00 ppm in the  $^1H$  NMR spectrum. Changing the catalytic system from  $Pd(PPh_3)_4$  to  $PdCl_2(dppf)$  or  $PdCl_2(PPh_3)_2/PPh_3$  met with little success as the coupling yield dropped dramatically. Selective functionalization of **2a** was readily achieved by lithiation-stannylation (*n*-BuLi, TMEDA, THF;  $Bu_3SnCl$ , 0 °C, 1 h) and the resulting organostannane **2c** was immediately subjected to the Stille coupling condition, thereby **2b** was removed by  $SiO_2$  chromatography after the coupling reaction. To construct an ester-capped OT series, organostannane **2c** was cross-coupled with methyl 4-iodobenzoate to provide bithiophene ester **3a** in 90% yield with >99% regiochemical purity as evidenced by  $^1H$  NMR spectroscopy (Scheme 2). The remarkably high stability of the terminal trimethylsilyl blocking group in the OT series was noted since no desilylation was observed during usual work-up and subsequent silica gel chromatographic purification. Presumably the electron-withdrawing nature of the ester moiety exerts a charge-destabilizing effect against proto-desilylation under a slightly acidic condition. The versatility of the TMS group was further exemplified by its ease of removal under mild conditions. For example, TMS-terminated **3a** was transformed into bromide **3b** (NBS,  $CHCl_3$ -HOAc), which on treatment with **2c** in the presence of a catalytic amount of palladium complex furnished trimethylsilylated quaterthiophene ester **4a** in overall 70% yield.

Scheme 3.



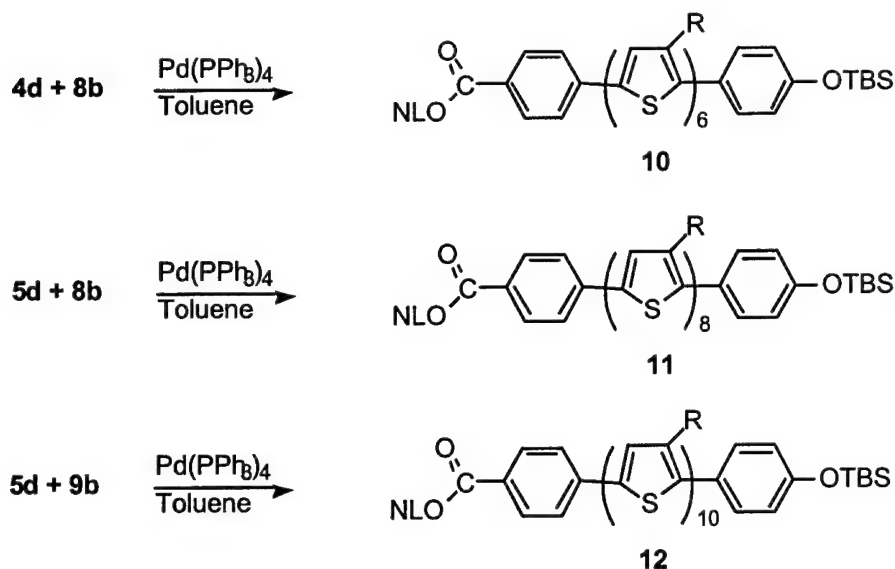
Scheme 4.



When the same bromination-Stille coupling reaction sequence was applied to **4a**, the desired sexithiophene **5a** was obtained in overall 55% yield. In a similar fashion, octithiophene **6a** capped with a terminal TMS group was also prepared in overall 50% yield from **5a**. Saponification of the brominated esters **4b** and **5b** (NaOH, THF-EtOH-H<sub>2</sub>O) proceeded cleanly to give intermediate bromo acids **4c** and **5c**. They were smoothly condensed with hydroxy functionalized NLO chromophore **7** under the Mitsunobu condition (DEAD, PPh<sub>3</sub>) to provide the fully functionalized NLO chromophore-containing quater- and sexithiophene, **4d** and **5d**, respectively, in overall 60 to 70% yield (Scheme 3).

To prepare the complementary OT series, bromo bithiophene **2d** (NBS, CHCl<sub>3</sub>-HOAc) was synthesized in moderate yield (60%) from a mixture of **2a** and **2b** (Scheme 4). A Kumada coupling between the Grignard reagent derived from the *tert*-butyldimethylsilyl ether of 4-bromophenol and **2d** provided the corresponding TBS ether substituted phenyl-capped bithiophene **8a** in 70% yield (Scheme 4). Elongation of **8a** was readily achieved by a lithiation-stannylation sequence followed by Stille coupling with **2d** to furnish quaterthiophene **9a** in 65% yield. Assembly of the two complementary OT series was implemented by the Stille coupling of **4d** and **5d** with tributylstannylated bithiophene **8b** to provide phenyl-capped sexithiophene **10** and octithiophene **11**. In a similar fashion, fully functionalized decithiophene **12** was accessible by cross-coupling **5d** with quaterthiophene organostannane **9b** (Scheme 5).

## Scheme 5.



solids and exhibit excellent solubility in most common organic solvents such as hexanes, toluene, chloroform and THF. The thermal transition behavior of these functionalized materials was studied by differential scanning calorimetry (DSC) at a heating rate of  $10\text{ }^{\circ}\text{C min}^{-1}$  under a nitrogen atmosphere. The amorphous nature of these functionalized materials was confirmed by the observation of low glass transition temperatures:  $T_g = -3.2$ ,  $-2.6$  and  $-1.8\text{ }^{\circ}\text{C}$  for **10**, **11** and **12**, respectively. These remarkably low  $T_g$  values originates from the large number density of the branched alkyl side chains on the thiophene rings, creating a highly disordered environment for molecular packing and effectively preventing crystallization of the bulk materials. The low- $T_g$  characteristics of these materials bear important consequences in the optimization of the PR performance through reorientation of the dipole of the NLO chromophore in response to a local space charge field (orientational enhancement effect).

**Optical Properties.** The optical properties of the trimethylsilyl-terminated OT esters **3a-6a** and the fully functionalized PR materials **10-12** were studied by UV-vis absorption spectroscopy and the data are summarized in Table 1. For the trimethylsilylated ester-capped OT series, broad and featureless absorption bands that can be ascribed to the  $\pi$ - $\pi^*$  transition of the conjugated oligothiophene backbone are observed (Figure 1). This transition shows a red-shifting from  $\lambda_{\text{max}} = 367\text{ nm}$  for bithiophene ester **3a** to  $397\text{ nm}$  for quaterthiophene **4a**, to  $408\text{ nm}$  for sexithiophene **5a** and finally to  $416\text{ nm}$  for octithiophene **6a** with simultaneous increase in molar absorptivity upon successive addition of a conjugated bithiophene unit. As the conjugation chain length increases, the  $\lambda_{\text{max}}$  gradually reaches a plateau starting from eight thiophene repeating units. This is in agreement with the findings of Bäuerle that the effective conjugation was attained at around eight thiophene repeating units for a similar ester-capped oligo(3-alkylthiophene) series.<sup>17</sup> This rather rapid saturation of the conjugation length can be attributed to the reduced coplanar conformation of the conjugated OT chains in solution state due to the presence of a sterically encumbered, bulky branched alkyl side-chain on each thiophene unit. The UV-vis spectra of NLO chromophore **7** and fully functionalized **10-12** are shown in Figure 2. The spectrum of **7** consists of an intense absorption band at  $\lambda_{\text{max}} = 492\text{ nm}$ , which is assignable to the charge transfer transition of the dipolar chromophore. The spectra of the fully functionalized OTs show two major peaks: an intense lower energy transition band (ca.  $490\text{ nm}$ ) with a tail extending to  $\sim 600\text{ nm}$ , as well as a large shoulder in the higher energy region of  $420\text{--}440\text{ nm}$ , which is due to the absorption of the conjugated OT backbone. The appearance of the

**Thermal Properties.** All of the functionalized NLO-containing oligothiophene molecules were obtained as amorphous soft red

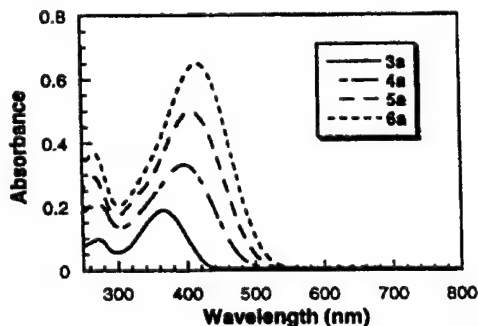


Figure 1. UV-vis spectra of trimethylsilyl oligothiophenes **3a-6a** in chloroform ( $c = 1 \times 10^{-5}\text{ mol L}^{-1}$ ).

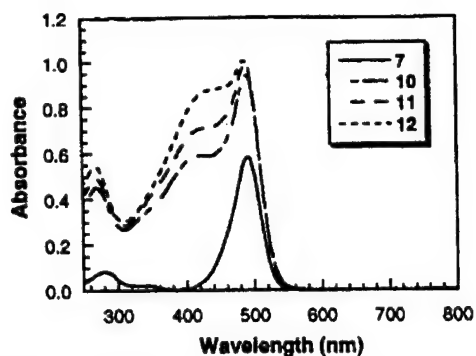


Figure 2. UV/vis spectra of NLO chromophore **7** and fully functionalized oligothiophenes **10-12** in chloroform ( $c = 1 \times 10^{-5} \text{ mol L}^{-1}$ ).

Table 1. UV/vis spectral data of trimethylsilyl oligothiophenes **3a-6a**, NLO chromophore **7**, and fully functionalized oligomers **10-12** in  $\text{CHCl}_3$  ( $c = 1 \times 10^{-5} \text{ mol L}^{-1}$ ).

	$\lambda_{\text{max}}$ (nm)	$E_{\text{abs}}$ (eV)	$\epsilon$	$\log \epsilon$
<b>3a</b>	367	3.38	1.891	4.277
<b>4a</b>	397	3.12	3.319	4.521
<b>5a</b>	408	3.04	4.982	4.697
<b>6a</b>	416	2.98	6.497	4.813
<b>7</b>	492	2.52	5.837	4.766
<b>10</b>	491	2.53	9.409	4.974
<b>11</b>	489	2.54	9.839	4.993
<b>12</b>	487	2.55	10.057	5.002

Table 2. Cyclic voltammetry data of oligothiophenes **3a-6a**, chromophore **7**, and functionalized oligomers **10-12** in  $\text{CH}_2\text{Cl}_2$  with  $0.1 \text{ mol L}^{-1} \text{ Bu}_4\text{NBF}_4$  as the supporting electrolyte at a scan rate of  $100 \text{ mV s}^{-1}$ . All potentials are calibrated against  $\text{Fc}/\text{Fc}^+$ .

	$E_1^\circ$ (V)	$E_2^\circ$ (V)	$E_3^\circ$ (V)	$E_4^\circ$ (V)
<b>3a</b>	0.72	1.16		
<b>4a</b>	0.44	0.71	1.19 <sup>a</sup>	
<b>5a</b>	0.33	0.51	1.10	
<b>6a</b>	0.25	0.38	0.77	0.96

7	0.71			
10	0.28	0.45	0.71 <sup>a</sup>	0.96 <sup>a</sup>
11	0.25	0.35	0.70	0.84 <sup>a</sup>
12	0.23	0.29	0.66	0.82

<sup>a</sup> irreversible redox process

large shoulder is due to a linear superposition of the absorption of both the conjugated backbone and chromophore moiety. It is clear that the intensity of the lower energy band correlates well with the concentration of the NLO chromophore unit. As the conjugation chain length increases, not only the ratio of backbone to chromophore absorption intensity increases, but also the centers of the shoulder peaks show consecutive red shifts of ~5 nm. The absorption behavior of these fully functionalized OTs can be considered a linear combination of the individual functional components.

**Redox Properties.** The redox properties of the TMS-terminated OTs and fully functionalized OTs were characterized by cyclic voltammetric studies. As the number of thiophene units increases, not only do the number of reversible redox processes increase, but also the redox transition becomes increasingly facile with oxidation potentials shifted to less positive values. It was noticed that no significant decrease in peak intensities was detected upon repeated cycling between 0 and +2.0 V, suggesting the high redox stability of these OT materials upon electrochemical cycling. Thus, two redox processes were observed for the bithiophene ester **3a**, clearly indicating successive removal of one and two electrons from the conjugated system to form a stable radical dicationic species. On the other hand, the number of redox transitions

Table 3. Selected photorefractive data of oligomers **10–12** at a light wavelength of 632.8 nm and applied field of 78 V  $\mu\text{m}^{-1}$ .

	10	11	12
$\alpha$ ( $\text{cm}^{-1}$ ) <sup>a</sup>	9.74	10.3	25.7
$\Gamma_p$ ( $\text{cm}^{-1}$ ) <sup>b</sup>	76.9	94.7	30.7
$\Phi$ ( $^\circ$ ) <sup>c</sup>	90	88	72
$\eta_p$ (%) <sup>d</sup>	18.9	25.1	10
$r_{33}$ ( $\text{pm V}^{-1}$ ) <sup>e</sup>	1.70	1.59	0.958
$\Delta n_{\text{fi}}$ ( $10^{-4}$ ) <sup>f</sup>	8.06	7.57	4.02
$\Delta n_{\text{sc}}$ ( $10^{-4}$ ) <sup>g</sup>	8.07	9.40	4.32
$r_n$ <sup>g</sup>	1.00	1.24	1.17

<sup>a</sup>  $\alpha$  is absorption coefficient,

<sup>b</sup>  $\Gamma_p$  is the PR gain coefficient for two *p*-polarized beam coupling,

<sup>c</sup>  $\Phi$  is a phase shift between index and intensity gratings,

<sup>d</sup>  $\eta_p$  is the diffraction efficiency for a *p*-polarized light,

<sup>e</sup>  $r_{33}$  is the electro-optic coefficient,

<sup>f</sup>  $\Delta n_{\text{fi}}$  is the applied field induced birefringence,

<sup>g</sup>  $\Delta n_{\text{sc}}$  is the index modulation by the space-charge field, and  $r_n = \Delta n_{\text{sc}}/\Delta n_{\text{fi}}$ .

increases to three for the longer OTs **4a** and **5a** along with decreasing potentials, underlying the accessibility of multiple stable redox states in this oligomer series. For the extended octithiophene ester **6a**, up to four oxidation waves were determined. This trend is comparable to a similar oligothiophene series reported by Bäuerle.<sup>17</sup> As evident from Table 2, the first, second and third redox potentials all show a gradual decrease with increasing thiophene rings, indicating an increase in conjugation length of the system. Detailed examinations of these potential changes revealed a leveling-off starting from the octithiophene **6a**, which is consistent with the onset of saturation of the conjugation length as suggested by the UV-visible absorption behavior. The fully functionalized materials exhibit similar electrochemical behavior and four redox transitions with increasing reversibility were observed. As the NLO chromophore is also electroactive (+0.71 V vs.  $\text{Fc}/\text{Fc}^+$ ), the third redox potentials for **10** and **11** were partially overlapped with the electrochemical response due to the NLO moiety. The general trend of decreasing redox potentials with increasing conjugation length is also observed but the changes are relatively small compared to the TMS-terminated OT series as the saturation length is reached.

**Photorefractive Properties.** Because of the amorphous nature of the materials, high-quality transparent thick films can be conveniently cast from solution. Typically, a filtered solution of the material in chloroform was dripped on two pieces of ITO glass



placed on a hot plate maintained at  $\sim 80^\circ\text{C}$ , and subsequently dried at  $60^\circ\text{C}$  in a vacuum oven for 16 h. The two glass substrates were then pressed together with a polyimide spacer to provide a transparent film with a thickness of  $127\ \mu\text{m}$ . Their photorefractive properties were determined by two-beam coupling and degenerated four-wave mixing (DFWM) experiments and the results are summarized in Table 3. In the two-beam coupling experiment, two coherent  $633\ \text{nm}$   $p$ -polarized He-Ne laser beams with identical intensity of  $0.83\ \text{W cm}^{-2}$  overlapped in the PR sample with an incident-crossing angle of  $7.5^\circ$  to generate the refractive index grating. The film normal was tilted at an angle of  $53^\circ$  with respect to the symmetric axis of the two writing beams to provide a non-zero projection of the grating wave vector along the poling axis. The photorefractive nature of these materials is unambiguously established by the observation of clear asymmetric energy exchange (two-beam coupling) between the two incident writing beams: one beam gained energy and the other lost energy. The amount of energy exchange is characterized by the two-beam coupling gain coefficient ( $\Gamma$ ):

$$\Gamma = (1/L)\ln[(1 - \alpha)/(1 - \beta\alpha)]$$

where  $\alpha$  is the intensity modulation of the signal beam ( $\Delta I_s/I_s$ ),  $\beta$  is the intensity ratio of the two incident writing laser beams ( $I_s/I_q$ ), and  $L$  is the optical path length of the beam with gain.

Of the three PR molecular materials examined, the highest PR optical gain coefficient ( $\Gamma = 94.7\ \text{cm}^{-1}$ ) was achieved with octithiophene **11** at an applied field of  $78\ \text{V } \mu\text{m}^{-1}$  and a wavelength of  $632.8\ \text{nm}$ . This result is translated into a large net optical gain of  $84.4\ \text{cm}^{-1}$  as the gain exceeds the absorption coefficient ( $\alpha = 10.3\ \text{cm}^{-1}$ ). This is directly comparable to the value in our previously reported photorefractive oligothiophene system in which a net gain of  $83\ \text{cm}^{-1}$  was obtained at  $E = 70.6\ \text{V } \mu\text{m}^{-1}$ . It is believed that index modulation benefits greatly from the high orientational (rotational) mobility of the NLO chromophore in response to the local electric field due to the orientational enhancement effect, as commonly observed in other amorphous low- $T_g$  organic PR polymers.<sup>2,4</sup> It was observed that as the electric field was switched off, the two-beam coupling gain and loss signals disappeared immediately and their original intensities were restored quickly. Thus, complete erasure and rewriting of the grating could be performed with good reversibility and reproducibility. This observation points to the photorefractive origin of index grating formation and excludes the possibility of beam coupling due to either thermal or absorption grating.

It is of great interest to correlate the PR properties with the conjugation length of the oligomers **10-12**. As expected, sizable optical gain was also observed for the other two oligomers in this series:  $\Gamma = 76.9$  and  $30.7\ \text{cm}^{-1}$  for sexi-**10** and decithiophene **12**, respectively. This yields a net two-beam coupling gain of  $67.2$  and  $5.0\ \text{cm}^{-1}$  for the two oligomers at an applied field of  $78\ \text{V } \mu\text{m}^{-1}$  (the absorption coefficients are  $9.74$  and  $25.7\ \text{cm}^{-1}$ , respectively). The dependence of two-beam coupling gain for oligomers **10-12** on the applied electric field follows a super-linear behavior typical of most PR systems (Figure 3). As the electric field increases, the gain initially increases slowly and then gradually increases to a maximum value limited by the accessible applied field. Apparently, no saturation of the PR gain was observed at a high field. The phase shift of the index grating with respect to the intensity grating (illumination pattern) was observed to increase with the applied field and was determined to be  $90$ ,  $88$  and  $72^\circ$  for the oligomers **10-12**, respectively at the highest applied field of  $78\ \text{V } \mu\text{m}^{-1}$ . Thus, the nearly  $90^\circ$  phase shift observed at high applied fields points to the non-local nature of the index grating formation, a unique property of the photorefractive effect of the materials. The variation of phase shift with the applied electric field for sexithiophene **10** is shown in Figure 4.

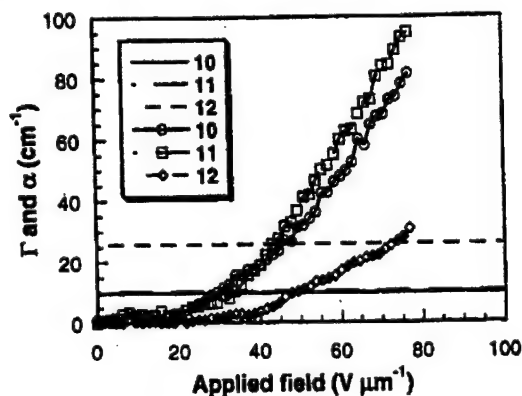


Figure 3. PR two-beam coupling gain and absorption coefficients of oligomers **10-12** as a function of applied field.

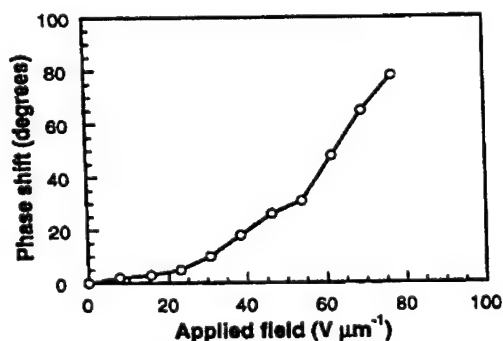


Figure 4. Phase shift of the index grating with respect to the intensity grating for functionalized oligomer **10**.

Degenerate four-wave mixing experiments were performed to yield further information on the PR properties of the oligomers. The influence of conjugation chain length on the diffraction efficiency follows a trend similar to that of PR optical gain. Whereas decithiophene 12 is associated with the longest chain length, it shows a smaller diffraction efficiency (10.0%) than that of either sexi- (18.9%) or octithiophene (25.1%) at a field of  $78 \text{ V } \mu\text{m}^{-1}$ . As expected, the diffraction efficiency increases super-linearly with increasing applied field and no saturation is observed. This similarity between the diffraction efficiency and PR gain confirms the assertion that a non-local index grating due to the photorefractive effect is mainly responsible for both the asymmetric energy exchange in two-beam coupling experiment and diffraction of the reading beam in DFWM experiment. The strong dependence of both the two-beam coupling gain or diffraction efficiency on the applied electric field and that no optical gain or diffraction signal was observed at zero applied field lends further support to the unique photorefractivity of the materials.

This somewhat anomalous dependence of PR properties on conjugation length could be rationalized on the basis of changes in the following parameters. Moving from sexithiophene 10 to decithiophene 12, an increase in photoconductivity is anticipated due to the combined effect of increasing absorption strength and photocharge carrier hopping rate. Thus, an increase in photocharge generation efficiency and enhancement of the space-charge field is expected upon lengthening the oligothiophene chain. On the other hand, the number density of NLO chromophore drops as the number of thiophene rings increases, resulting in a retardation of the index modulation. Also of importance is the change in number density of the trapping sites as the number of thiophene rings changes, however its influence on the space-charge field is most

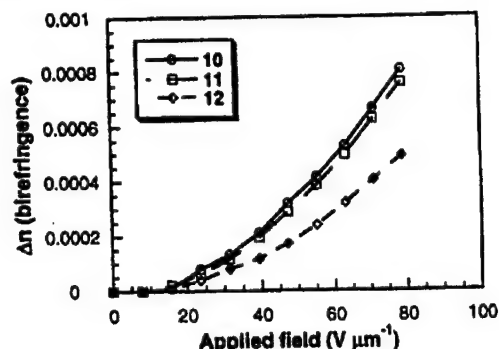


Figure 5. Field-induced birefringence of oligomers 10-12 as a function of applied field.

difficult to predict because there is uncertainty as to the exact nature and distribution of the trapping sites. Based on these reasonings, it can be envisaged that the initial increase in PR optical gain and diffraction efficiency between the sexi- and octithiophene materials could be attributed to the enhancement in space-charge field resulting from a change in photoconductivity. On the contrary, as the number of thiophene rings changes from eight to ten, the decreasing NLO chromophore density results in a reduction of index modulation and leads to a diminished optical gain and diffraction efficiency. The latter is supported by measurement of the birefringence of the materials. A unique feature of the present PR system is the large field-induced birefringence associated with the novel NLO chromophore (Figure 5). It is reasonable to assume that the birefringence is mainly induced by orientation of the nonlinear chromophore in response to an external field in a low- $T_g$  PR system. The birefringence shows a field enhancement behavior similar with that of PR gain and diffraction efficiency and maximum values were detected at an applied field of  $78 \text{ V } \mu\text{m}^{-1}$ :  $\Delta n_{\text{fi}} = 8.06, 7.57$ , and  $4.02 \times 10^{-4}$  for oligomers 10-12, respectively. In our oligothiophene PR system, it is found that contribution of the linear electro-optic effect to the index modulation is relatively small in comparison to that of the birefringence. The space-charge field induced index modulations were also determined for the three oligomers, which exhibits an initial increase followed by a decrease going from 10 to 12. The applied field dependence of index modulation follows a trend similar to that of the field-induced birefringence (Figure 5).

In order to compare the strength of the space-charge field among the three materials under the same applied field, it is necessary to normalize the contribution of the number density of the NLO chromophore for the three oligomers. Assuming the phase shift of the index grating is  $90^\circ$  in comparison to the illumination pattern, and the local field effect is the same for the three PR materials, the index modulation by the space charge field can be approximated by  $\Delta n_{\text{sc}} = r_n \Delta n_{\text{fi}} \sim n_{\text{fi}} \Delta n_{\text{fi}} (r_e^2 + 2r_e \cos \theta + 1) E_{\text{appl}}^2$ , where  $r_n = \Delta n_{\text{sc}} / \Delta n_{\text{fi}}$ ,  $r_e$  is the ratio of the magnitude of the space charge field to the externally applied field ( $E_{\text{sc}} / E_{\text{appl}}$ ),  $n_{\text{fi}}$  is the refractive index and  $\theta$  is the angle between the grating wave vector and film normal. Under identical applied field conditions, the index modulation by space-charge field depends linearly on the term  $\Delta n_{\text{fi}}$  and quadratically on the space-charge field. The term  $n_{\text{fi}} \Delta n_{\text{fi}}$  is proportional to the number density of the NLO chromophore. As a result, the parameter  $r_n$  defined in this manner eliminates the effect of the NLO chromophore. The variation of  $r_n$  as a function of number of thiophene rings in the oligomers 10-12 is shown in Table 3. The initial increase in  $r_n$  contributes markedly to the increase in PR gain and diffraction efficiency, despite the slight decrease in birefringence going from 10 to 12. However, as the number of thiophene rings further increases from eight to ten, there is a substantial decrease in both terms  $\Delta n_{\text{sc}}$  and  $\Delta n_{\text{fi}}$ , resulting in a smaller value of  $r_n$ , consistent with the decreasing NLO chromophore density.

## E. Conjugated Polymers Containing Mixed-ligand Ruthenium(II) Complexes. Synthesis, Characterization and Investigation of Photoconductive Properties

Hybrid polymers containing both organic and inorganic components have recently been pursued by many groups for a variety of applications.<sup>1-3</sup> One of the most attractive system is the conjugated polymers containing transition metal complexes.<sup>1</sup> Introduction of transition metal ions into  $\pi$ -conjugated polymers provides enormous opportunities to tune the physical properties of the resulting materials. From the strong interaction between transition metal complexes and conducting polymers, unique photophysical, photochemical and electrochemical properties are expected to evolve, leading to materials with a wide range of interesting physical properties, such as photorefractive effects, photoconductivity and novel redox property.<sup>1-3</sup> Ruthenium(II) polypyridine complexes are among the most studied molecules due to their rich and well-characterized photophysics and redox chemistry.<sup>4</sup> The polymers derived from these complexes have been demonstrated promising potential for applications in solar energy conversion, sensor, polymer supported electrode, nonlinear optics, photorefractive and electroluminescence.<sup>1, 5</sup>

Our research group has interests in these hybrid materials for a long time.<sup>1</sup> We want to utilize the rich photochemical and photophysical phenomenon in these metal-containing conjugated polymers for photorefractive applications and for harvesting light energy.<sup>6</sup> Therefore, poly(*p*-phenylenevinylene) (PPV) functionalized with various transition metal complexes such as tris(bipyridyl)ruthenium and tris(bipyridyl)osmium,<sup>1</sup> metalloporphyrin and metallophthalocyanine were synthesized.<sup>7</sup> The resulting polymers have shown enhanced photoconductivity and higher quantum yield of photocharge generation than those without metal complexes.

The most attractive feature that these systems offer is the flexibility in fine-tuning the optical and electronic properties of resultant materials. Simple change in the transition metal centers or the ligands can lead to the significant modulation of the physical properties of resulting polymers. However, to achieve this flexibility is a synthetic challenge, requiring synthesis of proper monomers and suitable polymerization methods. For example, ruthenium complexes of polypyridine such as 2,2'-bipyridine (bpy), 2,2':6',2''-terpyridine (tpy) have been the favored complexes for polymerization because they are compatible with Pd-catalyzed coupling and electrochemical coupling. There are far fewer investigations of the effect of ligand modification. In order to extend the chemistry of the well-known polypyridine ligands, we report the synthesis of a series of novel ruthenium complexes containing  $\beta$ -diketonate and hydroxyquinoline ligands and the integration of them into PPV main chains. It was found that the redox and optical properties of the resulting materials depends significantly on the structure of the ligands. These polymers have also been demonstrated to be photoconductive over a wide range of composition.

### Experimental Section

**Materials.** Tetrahydrofuran (THF) was distilled from Na<sup>+</sup> / benzophenone Ketyl. The *p*-divinylbenzene was separated from a mixture of *p*-divinylbenzene and *m*-divinylbenzene according to the literature procedure.<sup>8</sup> All of the other chemicals were purchased from the Aldrich Chemical Co. and used without further purification unless otherwise noted. The ligands used in this study are acetylactone (acac), 1,1,1-trifluoroacetylactone (tfac), 1,1,1,5,5,5-hexafluoroacetylactone (hfac), 4,4,4-trifluoro-1-phenyl-1,3-butanedione (tfpc) and 8-hydroxyquinoline (hyqu).

**Synthesis of Monomers.** Compound 1 and 3 were prepared by methods described previously.<sup>1c</sup>

**Compound 2a.** A solution of 0.103 g of compound 1 (0.131 mmol) in 15 mL of methoxyethanol was heated to 80 °C. *Cis*-dichlorobis(2,2'-bipyridine)ruthenium (II) hydrate (0.063 g, 0.131 mmol) in ethanol (10 mL) was added. The ethanol was then evaporated, and the resulting solution was stirred at 140 °C for 4 h. After cooling to room temperature, the solution was added into an (NH<sub>4</sub>)PF<sub>6</sub> (0.213 g, 1.30 mmol) aqueous solution. The solid precipitated out and was purified by chromatography (silica gel, dichloromethane/methanol (20:1)) to yield 0.135 g (54%) of red-orange solid. <sup>1</sup>H NMR (CDCl<sub>3</sub>, 400 MHz)  $\delta$  8.41 (m, 6H), 8.38 (d, 2H, *J* = 8.79 Hz), 7.95 (d, 4H, *J* = 8.37 Hz), 7.76 (dd, 4H, *J* = 5.10 Hz), 7.63 (s, 2H), 7.56 (s, 2H), 7.46 (m, 4H), 7.42 (s, 2H), 7.30 (d, 2H, *J* = 16.42 Hz), 6.79 (d, 2H, *J* = 16.42 Hz), 2.53-2.64 (m, 8H), 1.18-1.48 (m, 64H), 0.85 (t, 12H, *J* = 6.54 Hz). Elemental Anal. calcd. for C<sub>86</sub>H<sub>114</sub>N<sub>6</sub>I<sub>2</sub>P<sub>2</sub>F<sub>12</sub>Ru: C, 55.04; H, 6.07; N, 4.48; I, 13.52; Ru, 5.39. Found: C, 55.08; H, 6.12; N, 4.47; I, 13.60; Ru, 5.27.

**General Procedure for compound 2b-f.** To a solution of compound 1 in 10 mL of chloroform was added 2 equiv. hydrated ruthenium trichloride in 3 mL of ethanol. The resulting reddish brown solution was heated at 60 °C for 4 h and the color of the solution turned dark green. After removal of the solvent, the residue was separated by filtration chromatography (silica gel, dichloromethane/methanol (100:3)) to give a greenish solid. This greenish solid, triethylamine (1 equiv.), and acetylactone (4 equiv.) were then combined in 8 mL of THF and heated at 60 °C for 3 h, after which time the resulting mixture was poured into water. The mixture was extracted with dichloromethane. The combined organic layer was washed with water and dried over MgSO<sub>4</sub>. The solvent was removed by rotary evaporation, and the residue was chromatographed on neutral alumina (Brockmann activity IV) with hexane/dichloromethane (2:1) as eluent to afford the desired compound.

**Compound 2b:** 42% of green-brown solid. <sup>1</sup>H NMR (CDCl<sub>3</sub>, 400 MHz)  $\delta$  8.91 (s, 2H), 7.90 (d, 2H, *J* = 8.48 Hz), 7.63 (s, 2H), 7.56 (d, 2H, *J* = 7.81 Hz), 7.39 (s, 2H), 7.31 (d, 2H, *J* = 16.10 Hz), 6.94 (d, 2H, *J* = 16.09 Hz), 5.37 (s, 2H), 2.62-2.70 (m, 8H), 2.22 (s, 6H), 1.71 (s, 6H), 1.25-1.52 (m, 64H), 0.88 (m, 12H). Elemental Anal. calcd. for C<sub>76</sub>H<sub>112</sub>N<sub>2</sub>I<sub>2</sub>O<sub>4</sub>Ru: C, 62.02; H, 7.61; N, 1.90; I, 17.25; Ru, 6.87. Found: C, 61.86; H, 7.57; N, 1.84; I, 17.14; Ru, 6.75.

**Compound 2c:** 51% of green solid.  $^1\text{H}$  NMR ( $\text{CDCl}_3$ , 400 MHz)  $\delta$  8.72 (s, 2H), 7.80 (d, 2H,  $J = 8.42$  Hz), 7.61 (m, 4H), 7.37 (s, 2H), 7.31 (d, 2H,  $J = 16.11$  Hz), 6.93 (d, 2H,  $J = 16.09$  Hz), 5.78 (s, 2H), 2.60-2.67 (m, 8H), 2.29 (s, 6H), 1.25-1.52 (m, 64H), 0.86 (m, 12H). Elemental Anal. calcd. for  $\text{C}_{76}\text{H}_{106}\text{N}_2\text{I}_2\text{O}_4\text{F}_6\text{Ru}$ : C, 57.78; H, 6.71; N, 1.77; I, 16.07; Ru, 6.40. Found: C, 57.90; H, 6.80; N, 1.78; I, 16.13; Ru, 6.30.

**Compound 2d:** 47% of brown solid.  $^1\text{H}$  NMR ( $\text{CDCl}_3$ , 400 MHz)  $\delta$  8.67 (s, 2H), 8.06 (d, 2H,  $J = 8.46$  Hz), 7.89 (d, 2H,  $J = 8.45$  Hz), 7.66 (s, 2H), 7.45 (d, 2H,  $J = 16.49$  Hz), 7.41 (s, 2H), 6.96 (d, 2H,  $J = 16.10$  Hz), 6.17 (s, 2H), 2.63-2.71 (m, 8H), 1.26-1.54 (m, 64H), 0.86 (m, 12H). Elemental Anal. calcd. for  $\text{C}_{76}\text{H}_{100}\text{N}_2\text{I}_2\text{O}_4\text{F}_{12}\text{Ru}$ : C, 54.08; H, 5.92; N, 1.66; I, 15.04; Ru, 5.99. Found: C, 53.87; H, 5.78; N, 1.60; I, 14.92; Ru, 5.88.

**Compound 2e:** 40% of green-brown solid.  $^1\text{H}$  NMR ( $\text{CDCl}_3$ , 400 MHz)  $\delta$  8.79 (s, 2H), 8.01 (m, 6H), 7.73 (d, 2H,  $J = 8.40$  Hz), 7.57 (s, 2H), 7.50 (m, 2H), 7.41 (m, 4H), 7.32 (s, 2H), 7.29 (d, 2H,  $J = 16.16$  Hz), 6.87 (d, 2H,  $J = 16.10$  Hz), 6.46 (s, 2H), 2.63 (t, 4H,  $J = 7.80$  Hz), 2.47 (t, 4H,  $J = 7.64$  Hz), 1.25-1.52 (m, 64H), 0.87 (m, 12H). Elemental Anal. calcd. for  $\text{C}_{86}\text{H}_{110}\text{N}_2\text{I}_2\text{O}_4\text{F}_6\text{Ru}$ : C, 60.62; H, 6.46; N, 1.64; I, 14.90; Ru, 5.93. Found: C, 60.49; H, 6.37; N, 1.62; I, 14.81; Ru, 5.85.

**Compound 2f:** 53% of green solid.  $^1\text{H}$  NMR ( $\text{CDCl}_3$ , 400 MHz)  $\delta$  10.40 (s, 2H), 8.13 (d, 2H,  $J = 8.48$  Hz), 7.95 (d, 2H,  $J = 9.21$  Hz), 7.75 (d, 2H,  $J = 9.19$  Hz), 7.63 (s, 2H), 7.55 (s, 2H), 7.51 (m, 6H), 7.34 (d, 2H,  $J = 16.10$  Hz), 7.19 (s, 2H), 7.01 (d, 2H,  $J = 16.09$  Hz), 6.59 (d, 2H,  $J = 15.37$  Hz), 2.59-2.68 (m, 8H), 1.24-1.41 (m, 64H), 0.86 (m, 12H). Elemental Anal. calcd. for  $\text{C}_{84}\text{H}_{110}\text{N}_4\text{I}_2\text{O}_2\text{Ru}$ : C, 64.60; H, 7.04; N, 3.59; I, 16.25; Ru, 6.47. Found: C, 64.43; H, 7.07; N, 3.68; I, 15.98; Ru, 6.52.

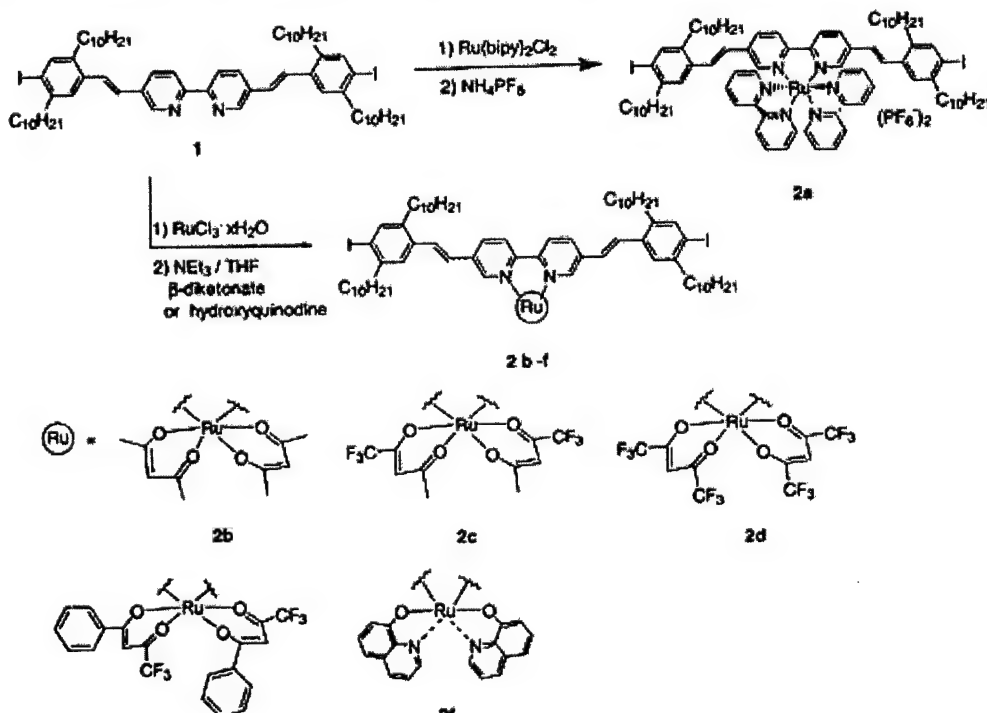
**Polymerization.** A typical polymerization procedure follows: Tri-*n*-butylamine (0.16 mL, 0.67 mmol) was added to a mixture of compound 2a (0.03 g, 0.016 mmol), compound 3 (0.112 g, 0.144 mmol), *p*-divinylbenzene (0.0208 g, 0.160 mmol), palladium acetate (1.4 mg, 0.0062 mmol), and tri-*o*-tolylphosphine (9.7 mg, 0.032 mmol) in 4 mL of DMF. The reaction mixture was stirred at 90 °C for 5 h under a nitrogen atmosphere and then poured into methanol. The precipitate was collected, redissolved in chloroform, and filtered to remove the catalyst residue. The filtrate was concentrated and precipitated into methanol, followed again by filtration and reprecipitation. The resulting polymer was further purified by extraction in a Soxhlet extractor with methanol for 24 h and then dried under a vacuum overnight.

**Characterization.** The  $^1\text{H}$  NMR spectra were collected on a Bruker 400 MHz FT NMR spectrometer. The FTIR spectra were recorded on a Nicolet 20 SXB FTIR spectrometer. A Shimadzu UV-2401PC spectrometer and a Shimadzu RF-5301 PC spectrofluorophotometer were used to record the absorption and emission spectra. The cyclic voltammetry was measured on an EG&G Princeton Applied Research potentiostat interfaced to a personal computer. The experiment was carried out with platinum disk working electrode, a platinum wire counter electrode and an Ag/Ag<sup>+</sup> reference electrode. The supporting electrolyte used was 0.1 M tetrabutylammonium perchlorate in dried dichloromethane. The half-wave potential was calculated using the equation  $E_{1/2} = (E_{p,a} + E_{p,c})/2$ , where  $E_{p,a}$  and  $E_{p,c}$  are the peak anodic and peak cathodic potentials, respectively. Thermal analyses were performed by using the DSC-10 system from TA Instruments with a heating rate of 10 °C/min under a nitrogen atmosphere. Elemental analyses were performed by Atlantic Microlab, Inc. and Galbraith Laboratories, Inc. Molecular weights were measured with a Water GPC system using polystyrene as the standard and THF as the eluent. The photoconductivity was studied by measuring the voltage drop across a 1 M $\Omega$  resistor resulting from a photocurrent running through the sample.<sup>9</sup> A He-Ne laser (632.8 nm), diode laser (690 nm) and semiconductor laser (780 nm) were used as the light sources, respectively.

## Results and Discussion

**Monomer Synthesis.** Scheme 1 outlines the approach for syntheses of these mixed-ligand ruthenium complexes. Compound 1 (L) was heated with hydrated ruthenium (III) trichloride in chloroform/ethanol to generate intermediate ruthenium complex -  $\text{RuLCl}_3$ . After filtration chromatography, the residue was placed in THF with an excess amount of ligand and triethylamine, and refluxed for several hours. The triethylamine serves both as a reducing agent toward the  $\text{RuLCl}_3$  and as a

deprotonating agent for the  $\beta$ -diketone and hydroxyquinoline.<sup>10</sup> The desirable product was purified by column chromatography on neutral alumina with hexane/dichloromethane as the eluent. Bipyridyl ruthenium complex (2a) was also synthesized for the purpose of comparison. The purity of these metal complexes was confirmed by elemental analysis.





## Scheme 1. Synthesis of Complexes 2a-f

**Structural Characterization.** The structures of these complexes were characterized both spectroscopically and analytically. The results from combustion analysis are consistent with all of the expected structures. It should be noted that the complexes with unsymmetrical ligands such as tfac and tfpc have geometrical isomers. However, discrimination between  $\text{trans}(\text{CF}_3)\text{-cis}(\text{CH}_3)\text{-}\{\text{RuL}\}$  and  $\text{cis}(\text{CF}_3)\text{-trans}(\text{CH}_3)\text{-}\{\text{RuL}\}$ ,  $\text{trans}(\text{CF}_3)\text{-cis}(\text{C}_6\text{H}_5)\text{-}\{\text{RuL}\}$  and  $\text{cis}(\text{CF}_3)\text{-trans}(\text{C}_6\text{H}_5)\text{-}\{\text{RuL}\}$  are not possible from the NMR spectra, since both are of  $\text{C}_2$  symmetry. Only one signal from the methine protons of tfac<sup>-</sup> and tfpc<sup>-</sup> ligands in their  $^1\text{H}$  NMR spectra was observed for both complexes 2c and 2e.

The FTIR spectra of ruthenium acetylacetonato complexes (2b-e) show very strong, characteristic absorption peaks corresponding to the C=O stretching mode, appearing around the  $1526 - 1592\text{ cm}^{-1}$  region depending on the substituents (Table 1).<sup>11</sup> For the complexes having trifluoromethyl substituents, the frequencies of the absorption peaks are higher than for the others. Such a trend is explained in term of the stronger electron-withdrawing power of the trifluoromethyl group relative to  $\text{CH}_3$  group, and the consequent strengthening of the C=O bonding.<sup>12</sup>

The UV/vis spectra of these complexes are presented in Figure 1. The  $\pi\text{-}\pi^*$  transition at 374 nm, observed in compound 1, was red-shifted upon coordination to a metal ion ( $\lambda_{\text{max}} = 395 - 423\text{ nm}$  for complexes 2a-f). This shift is normally observed for  $\pi$ -conjugated systems and is ascribed to the effect of the positive charge on the energy levels of bpy. In complex 2a, a ligand-centered transition due to the bpy exists at around 285 nm. The absorption due to the metal-to-ligand charge transfer (MLCT) transition overlaps with that of the  $\pi\text{-}\pi^*$  transition. We can tentatively assign that the  $\pi\text{-}\pi^*$  transition at 423 nm and the MLCT transition at about 450 nm.<sup>1,4</sup> In complexes 2b-f, the intensities of the bands arising from bpy-centered transition decreased dramatically. The MLCT bands further red-shifted toward lower energy ( $\lambda_{\text{max}} = 551 - 708\text{ nm}$ ) due to the reduction of the ligand-field strength. This is presumably due to a decreasing  $\text{M}\rightarrow\text{L}$   $\pi$ -interaction, which corresponds to an increase in the energy of the  $\text{Ru}(\text{d}\pi)$  orbital. Acetylacetonate and phenolate groups are poor  $\pi$ -acceptors compared to the bpy as a ligand. Variation of the ligands results in a range of MLCT energies. The complexes 2a-f do not show luminescence at room temperature, although compound 1 exhibits strong emission peaks at 426 and 448 nm, a feature typical for dialkyl substituted PPVs. It seems that the emission process is quenched after the Ru complexes are incorporated.

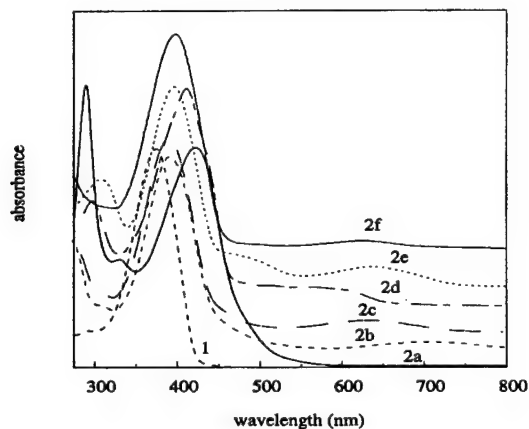


Figure 1. UV/vis spectra of compound 1 and complexes 2a – f in chloroform

**Polymer Synthesis and Characterization.** From our previous studies and the work of other groups, the Heck coupling reaction was found to be versatile in synthesizing functional conjugated polymers due to its mild condition.<sup>1, 13</sup> In this study, ruthenium complexes bearing diiodofunctional groups were copolymerized with 1,4-divinylbenzene and 1,4-diiodo-2,5-dihexadecanebenzene 3 in different stoichiometric ratio under the standard Heck reaction condition (Scheme 2). Dimethylformamide (DMF) was used as the solvent and the catalyst system was composed of palladium acetate (4 mol-%), tributylamine (2.5 equiv.), and tri-*o*-tolylphosphine (20 mol-%). All the ruthenium complexes except 2f are able to survive in the polymerization condition. A series of PPV type polymers with different ruthenium loading ranging from 0 to 50 percent were prepared and some of their physical properties are summarized in Table 2.

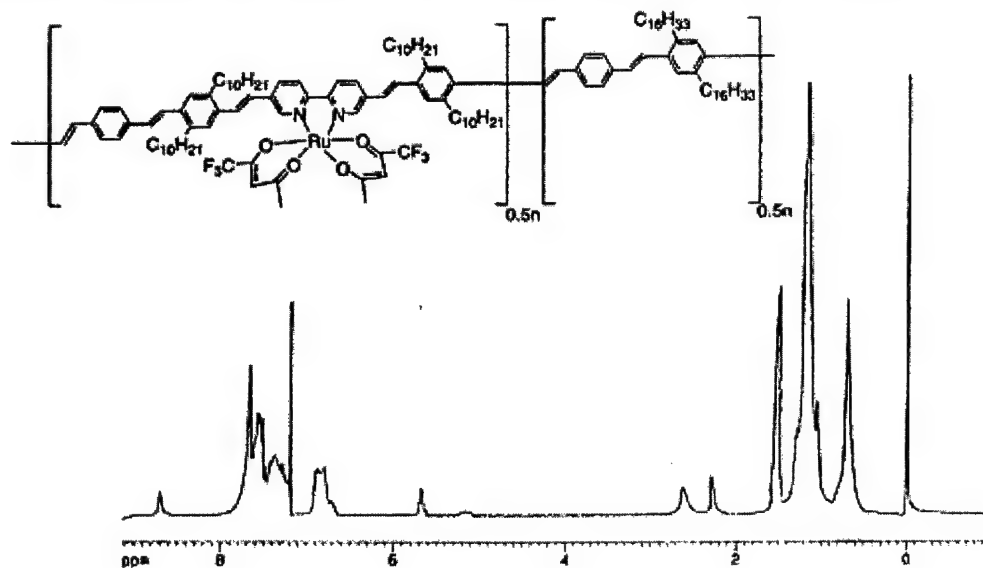
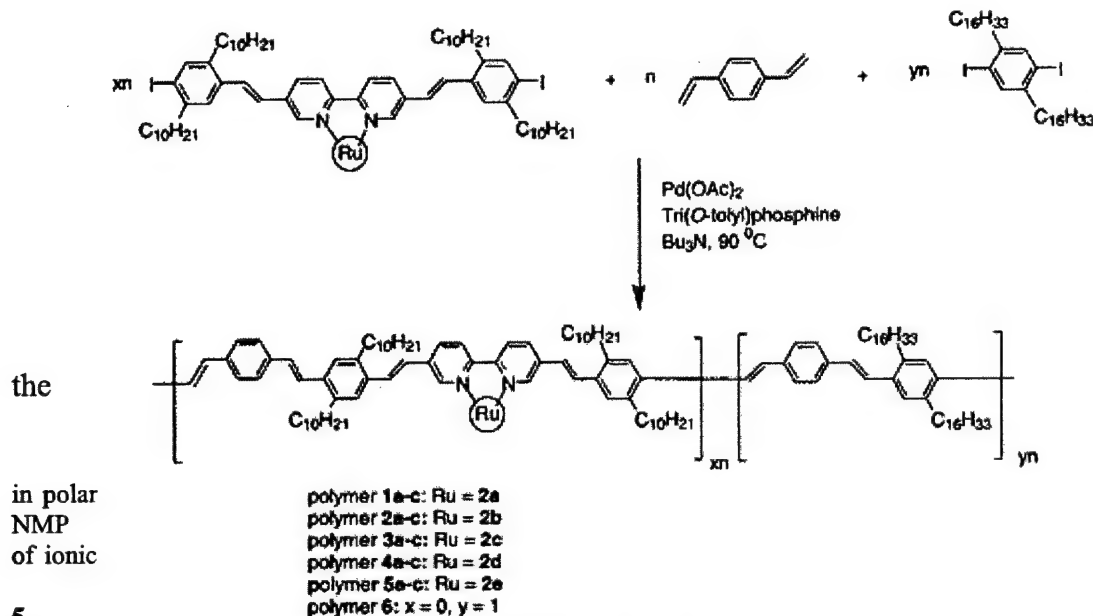


Figure 2 The  $^1\text{H}$  NMR spectrum of polymer 3c.

Absorption spectra of these polymers feature a strong band with  $\lambda_{\text{max}} \approx 400$  nm which is assigned to the  $\pi$ - $\pi^*$  transition of the polymer backbone. The presence of the ruthenium metal complexes is manifest by the appearance of a lowest-energy MLCT band associated with different metal complexes. The delocalized nature of the  $\pi^*$  acceptor orbital in the polymers is evident by about 12 – 50 nm red shift of the MLCT transition relative to the position in the corresponding monomer. The intensity of the MLCT band increases (relative to the  $\pi$ - $\pi^*$  transition) with the increase of the ratio of the complex. This is a useful feature to control the polymer's optical properties. The absorption strength of the polymers at longer wavelengths can be adjusted by controlling the ratio of the monomers.



FTIR spectra of the polymers **2** – **5** show C=O bands at 1520 – 1600  $\text{cm}^{-1}$ , further confirming that the diketonate ruthenium complexes were incorporated into polymers. The polymers **1a-c** exhibit a typical absorption bands of pyridine moieties at 1620  $\text{cm}^{-1}$  (triple absorption bands) and at 760  $\text{cm}^{-1}$ . The intensities of these peaks are well correlated to the ruthenium complex composition. The intense band at 965  $\text{cm}^{-1}$  for polymers **1- 6** is ascribed to the out-of-plane bending vibration of the trans-substituted vinylene group.

The thermal properties of these polymers were examined by differential scanning calorimetry (DSC) (Table 2). All of these polymers show a rather low glass transition temperature presumably due to the existence of long greasy side chain and the bulky metal complexes. It was found that the decomposition temperature of the polymers decreases as the ratio of metal complexes increases. The presence of the bulky ruthenium complexes may distort the packing of polymer chains and reduce the thermal stability of the polymer.

**Cyclic Voltammetry.** The redox properties of these complexes were studied by cyclic voltammetry in  $\text{CH}_2\text{Cl}_2$  solution. Examination of the electrochemistry data reveals a number of interesting features. For complex **2a**, the reversible wave of the Ru(III/II) couple occurs at  $E_{1/2} = 1.13$  V vs.  $\text{Ag}^+/\text{Ag}$  in 0.1 M  $\text{Bu}_4\text{NClO}_4$  / dichloromethane (Table 1). Under the same condition, the reversible waves of the Ru(III/II) couple for complexes **2b-f** require much smaller voltage, ( $E_{1/2}$  between 0.012 - 0.58 V). Replacement of  $\pi$ -acidic pyridyl ligands by  $\sigma$ -donating diketonate and phenolate ligands results in a decrease in redox potential of the Ru(III/II) couple (and hence stabilization of the high oxidation state) by 1.118 – 0.55 V. The anionic  $\beta$ -diketonate and phenolate groups also reduce the charge of the complex cation from +2 to 0, which results in additional electrostatic stabilization of the oxidation state. This is in agreement with the shift of the MLCT (metal oxidation) bands to lower energy by electron donation from acetylacetonate and phenolate group in UV/vis studies. The electrochemical data presented in Table 1 also suggest that the electron density of the ruthenium center is strongly influenced by the electron-donating/withdrawing nature of the substitutes on  $\beta$ -diketonate ligands. The Ru(III/II) redox potentials shift in the anodic direction with the  $\beta$ -substituent on diketonate ligand in the following order:  $\text{Me} < \text{Ph} < \text{CF}_3$ . Hammett constant,  $\sigma_m$ , can provide an approximate measure of substituent inductive effect.<sup>14</sup> The linear relationship between  $E_{1/2}$  for the Ru(III/II) couples and the sum of the Hammett constants ( $\Sigma\sigma_m$ ) for substituents on the  $\beta$ -diketonate ligands indicates that the influence of the substituents is largely inductive.<sup>15</sup> Holm<sup>16</sup> and Takeuchi<sup>17</sup> and their co-workers have also reported linear relationships for  $E_{1/2}$  vs.  $\Sigma\sigma_m$  with ruthenium tri- $\beta$ -diketonate complexes. Hence, the redox potentials of these complexes can be fine-tuned by varying the ligand substituents.

The cyclic voltammograms of the polymers **1** – **5** clearly showed the reversible metal-centered oxidation processes (Fig. 2). It was found that the polymerization did not significantly alter the redox properties of the complex moieties compared to their corresponding monomers. However, the redox peaks corresponding to the conjugated backbone shift after the incorporation the transition metal complexes. The irreversibility cathodic peaks shift from -1.78 V in polymer **6** to about -1.54 V in polymers **1** – **5**. The irreversible anodic peaks appear around 1.42 V in polymers **1** – **5** while it appears at 1.58 V in polymer **6**. The irreversibility of these redox processes was also observed in other metal containing conjugated polymers and may be due to the charge trapping in the polymer during the doping process.<sup>18</sup>

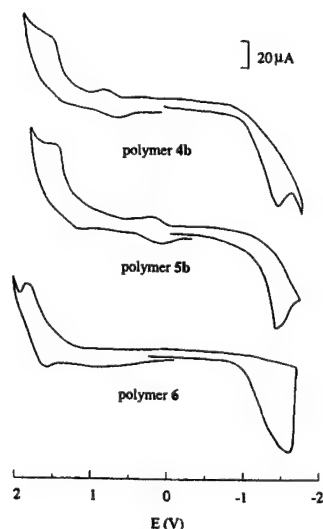


Figure 3. Cyclic voltammograms of polymers 4b, 5b and 6.

**Photoconductivity.** Photoconductivity is one of the most informative phenomena for many organic semiconductors.<sup>19</sup> The MLCT process in the ruthenium complexes enables us to excite the polymers at longer wavelengths. Information about photogeneration, recombination and transport processes of the charge carries can be obtained. Upon excitation in the region of the MLCT transition of the ruthenium complex, electrons will be injected into the polymer backbone (equivalent of n-doping of PPV), and transport away through either intrachain migration or interchain hopping. It is also well-known that oxidation or reduction (doping) of conjugated polymer backbones results in a highly conducting state of polymers.<sup>20</sup> Thus, the charge separation efficiency and photoconductivity can be greatly improved by the combination of efficient photocharge generator and charge transporter. The samples for photoconductivity measurement were prepared by casting a polymer solution onto an indium-tin-oxide (ITO) glass. A thin layer of gold electrode (150 Å) was coated onto the polymer film by vacuum deposition. The typical thickness of the polymer film was approximately 1 µm. The photocurrent was measured by monitoring the voltage drop on a resistor that is in series with the film capacitor. Based on their different MLCT bands, the polymers were excited by different wavelengths of the light sources. For example, the polymer 1a and 6 were excited by a He-Ne laser (632.8 nm). The polymer 4a was shone by a diode laser (690 nm), while polymer 2a, 3a and 5a were illuminated by a semiconductor laser (780 nm). As shown in Figure 4, the photoconductivity

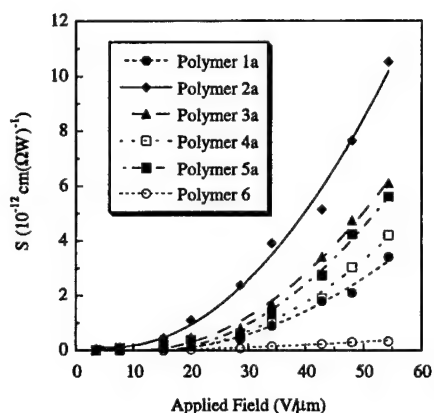


Figure 4. Photoconductive sensitivity of polymers 1a – 6 as a function of the applied field. Polymers 1a and 6 were excited at 632.8 nm. Polymer 4a was excited at 690 nm. Polymers 2a, 3a and 5a were excited at 780 nm.

and quantum yield of photocharge generation strongly depend on the applied field and exhibit trends well correlated with the cyclic voltammetry results of the complexes. The lower oxidation potential of the complex, the higher photoconductivity and quantum yield of photocharge generation the polymer will have. Compared to the polymer 6, polymers with ruthenium complexes exhibit much higher photoconductivity at long wavelengths. The photoconductivity of the polymers also appears to be dependent on the ruthenium content in the polymer. Under the same electric field strength, the conductivity increases as the ruthenium content is increased (Fig. 5). The photoconductivity of the polymers at different wavelength resembles their MLCT absorption spectra (Fig. 6). The above results clearly confirm that the ruthenium complexes extend the photosensitivity of the polymers to the region of longer wavelengths through the presence of their lowest-energy MLCT band.

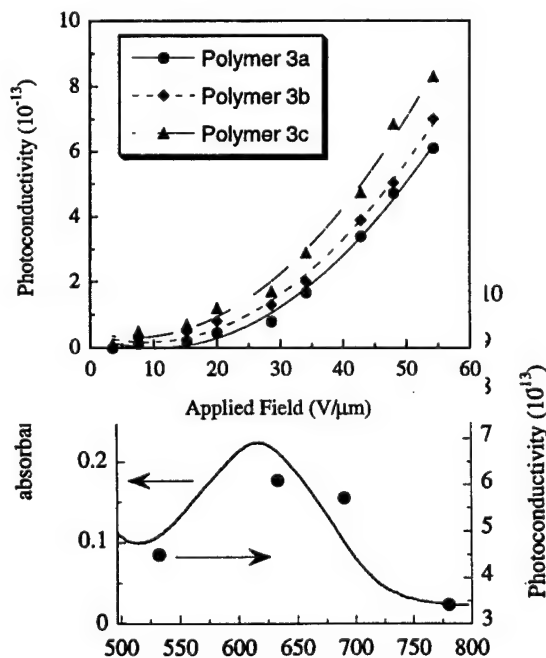


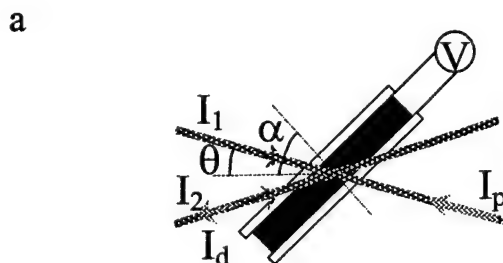
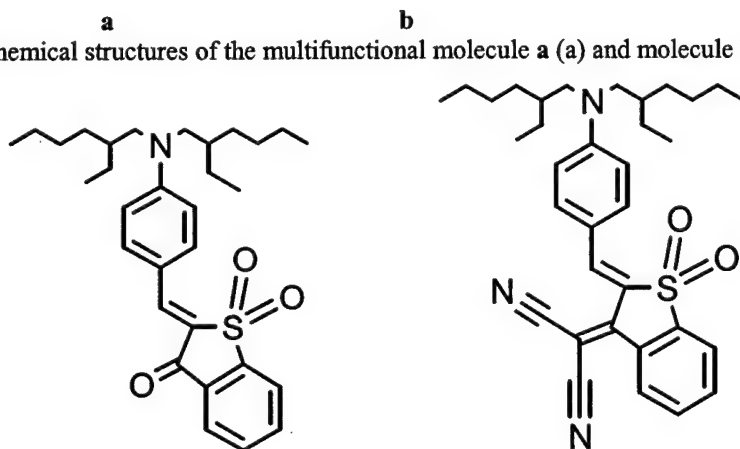
Figure 5. Dependence of photoconductivity on the applied field for polymers 3a – c at 780 nm.

Figure 6. Photoconductivity and absorption spectrum of polymer 3a in the visible region.

#### F. The Simpler, The Better--- Molecular Photorefractive Materials Based On Methine Dyes

Four functional species are needed to show the photorefractive (PR) effect in a polymeric material. They are charge generating, transporting, trapping and electro-optic components.<sup>1,2</sup> Therefore, a paradigm exists in the preparation of photorefractive polymeric materials particularly that multi-component composite materials were prepared and multifunctional polymers synthesized.<sup>3</sup> It is exciting to note that the photorefractive properties in some of these polymeric materials have surpassed many inorganic counterparts. The optical gain coefficients of more than  $200 \text{ cm}^{-1}$ , diffraction efficiencies near 100 % on  $\sim 100 \mu\text{m}$  thin films<sup>4</sup>, and a video frequency response time (6ms) have been achieved<sup>5</sup>. However, the composite materials need a delicate formulation of different components, and are thermodynamically unstable (phase separation). The syntheses of multifunctional polymers are tedious and slow in the generation of new materials. Is this paradigm necessary for searching or designing good organic PR materials? Our photorefractive results on the materials composed of the molecular as shown in Figure 1a and 1b (herein molecule a and b) seems to be no. Methine dyes are well studied as near infrared dyes<sup>6</sup> and for their second-order nonlinear optical effects<sup>7,8</sup>. Recently, we discovered complementary grating competition in a fully functionalized photorefractive material that was composed of a methine dye linked covalently to a sexithiophene derivative<sup>9,10</sup>. It was demonstrated that these methine dyes are electronic photoconductive materials.<sup>10</sup> We then recognized that methine dye molecules possess the four functionalities necessary for manifesting the photorefractive effect. In order to study their PR effect, molecules a and b were designed and synthesized (Figures 1a and 1b).<sup>9</sup> To ensure that the materials obtained would be amorphous,

Figure 1. Chemical structures of the multifunctional molecule a (a) and molecule b (b)



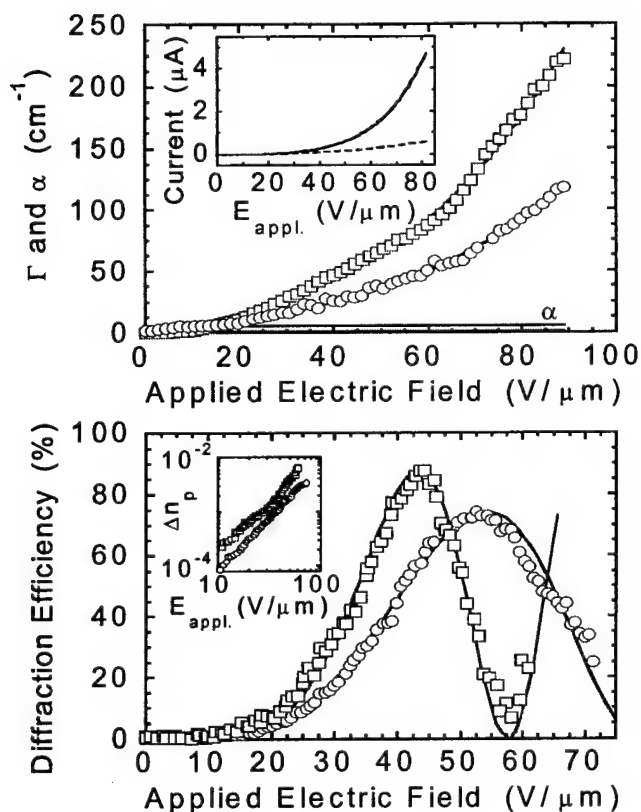


**Figure 2.** (a). The set-up geometry for grating recording experiments. All of the optical measurements for the samples made of molecule **a** were carried out with a He-Ne laser (633 nm) and for those of molecule **b** with a Diode laser (780 nm). For a two-wave-mixing experiment, two laser beams are *p*-polarized to write the grating. Beam 1 refers to the amplified beam, 2 the attenuated one. For the sample made of molecule **a**,  $\beta = 54^\circ$ ,  $\theta = 9.9^\circ$ ,  $I_1 = 1.38 \text{ W/cm}^2$  and  $I_2 = 1.35 \text{ W/cm}^2$ . For the sample made of molecule **b**,  $\beta = 53^\circ$ ,  $\theta = 9.6^\circ$ ,  $I_1 = 2.89 \text{ W/cm}^2$ ,  $I_2 = 0.765 \text{ W/cm}^2$ . The gain coefficient is calculated by using the expression,  $\Gamma = (1/L) \times \ln[\beta\gamma/(1+\beta-\gamma)]$ , with  $L = nd/[n^2 \sin^2(\alpha + \theta)]^2$ ,  $\beta = I_1/I_2$ , where  $\gamma$  is the beam coupling ratio that is defined as the ratio of the signal intensities with and without pump beam of  $I_1$ ,  $d$  is film thickness,  $n$  is the refractive index of the sample, as determined using a prism coupler. The refractive index of sample of molecule **a** is 1.64 at the wavelength of 633 nm, and that of molecule **b** is 1.68 at 780 nm. Two writing laser beams for a degenerate four-wave mixing experiment are *s*-polarized and the probe beam is *p*-polarized. For the sample of molecule **a**,  $\beta = 54^\circ$ ,  $\theta = 9.9^\circ$ ,  $I_1 = 1.43 \text{ W/cm}^2$  and  $I_2 = 1.46 \text{ W/cm}^2$ . For sample of molecule **b**,  $\beta = 53^\circ$ ,  $\theta = 9.6^\circ$ ,  $I_1 = 1.56 \text{ W/cm}^2$ ,  $I_2 = 1.43 \text{ W/cm}^2$ . The diffraction efficiency is defined as the intensity ratio of diffracted beam *d* and the transmitted beam without writing beams 1 and 2. (b). optical gain and absorption coefficients as a function of applied field for sample of molecule **a** (circles) and **b** (squares). The solid lines are theoretical fitting according to the "Kukhtarev model".<sup>12</sup> The inset is a typical photo-/dark current dependence on the applied field on the sample of molecule **b** (27  $\mu$ m sandwiched between an ITO glass and an aluminum plate). The light has a wavelength of 780nm with an irradiation intensity of 128 mW/cm<sup>2</sup> (c). diffraction efficiency of the sample of molecule **a** and **b**, respectively, as a function of applied field at the wavelength of 633nm and 780nm (circles and squares). The inset is index modulations as a function of applied field, calculated according to  $\Delta n = \lambda(\cos\theta_2 \cos\theta_1)^{1/2} \sin^{-1} \sqrt{\eta / \pi d \cos(\theta_2 - \theta_1)}$ .

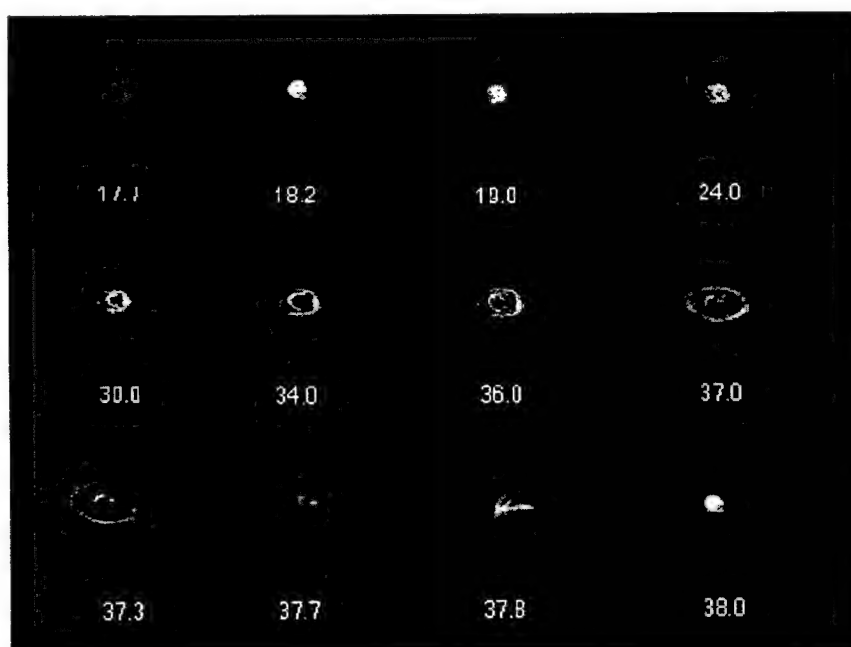
Two branched alkyl chains bearing chiral carbons were attached to the amino group. Films exhibiting excellent optical quantity can be easily prepared from these materials and their optical transparency is stable for a long-term. Wide angle X-ray diffraction experiments confirmed the amorphous nature of the materials. The glass transition temperatures ( $T_g$ ) for the molecules **a** and **b** is ca 6 and 26 °C, respectively, determined with a differential scanning calorimeter. The low  $T_g$  values benefit the photoinduced index modulation through the orientational enhancement.<sup>11</sup> Solution electro-chemistry measurements indicated that the molecules have low reduction potentials (0.83 and 0.41V with respect to the standard hydrogen electrode for molecule **a** and **b**, respectively) and act as an electronic photoconductor (See Figure 2b). Photocurrent measurements indicated that these materials are indeed photoconductive.

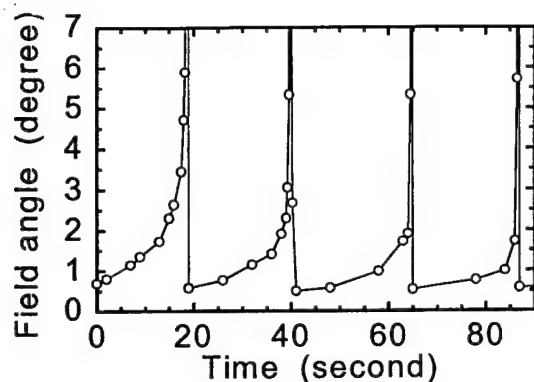
To study the PR effect, films with a thickness of 130µm were sandwiched between two pieces of glass coated with indium tin oxide. A polyimide film was used as the spacer to maintain the uniformity of the resulting films. The photorefractive optical gains were measured using a two-beam coupling experiment as shown in Figure 2a. Figure 2b shows the dependence of the gain coefficients on the external field for samples made of molecules **a** and **b**. Large gain values of 117.7 and 221.4 cm<sup>-1</sup>, were observed for materials **a** and **b**, respectively, at an external field of 89 V/µm. Since the absorption coefficients of the two samples at the working wavelength (780 and 633nm) are 1.64 and 5.54 cm<sup>-1</sup>, net optical gains of 116.1 and 215.9 cm<sup>-1</sup> were achieved. The latter value is one of the highest gain coefficients reported for organic photorefractive materials. The photo-induced index modulations were determined with degenerated four wave mixing experiments as shown in Figure 2a. The diffraction efficiencies reached the maximum of 74.3 % for material **a** at 633 nm at the applied field of 53 V/µm ( $E_{\pi/2}$ ) and 87.6 % for materials **b** at 780 nm and 44 V/µm (Figures 2c). The solid lines in the figures represent the theoretical fitting of the field-dependencies of the diffraction efficiency with the standard photorefractive model.<sup>12</sup> The inset of the Figure 2c is a plot of index modulations as a function of applied field calculated from the diffraction efficiency. The maximum index modulations  $\Delta n_p$  of 0.0034 and 0.0063 for samples of molecule **a** and **b**, respectively. The index modulations at which the diffraction efficiencies reach their first maximum satisfy the relation:

$$\Delta n_{\pi/2} = \lambda(\cos\theta_2 \cos\theta_1)^{1/2} / 2d \cos(\theta_2 - \theta_1).$$

Because of the large photo-induced index modulations and the high optical qualities, these materials are readily used as the medium for holographic information storage. The grating were reversible and could be completely erased and rewritten with good reproducibility.<sup>1,4</sup> It was also found that the dynamics of the grating formation did not follow a single-exponential function; rather it followed a bi-exponential one. For the molecule **b** at an external field of 84 V/µm, the index change of 52% has been formed with a time constant of 16.6 ms and the remaining 48% has a time constant of 1.2 sec.

The large index modulation also led to a large self-defocusing of light beams. The intensity distribution and the propagation dispersion of the output beam can dramatically be changed. The near-field pattern of the output beam is characterized as a series of bright and dark rings. With the increase of the applied field, the size of the first bright ring increased monotonously. When the applied field surpassed a threshold, which is a function of light intensity, the self-defocusing underwent a periodical pulsation. The size of the rings expanded with time in an accelerating fashion until a dramatic expansion occurred, followed by a collapse to its original (no defocusing) pattern. A typical sequence of the image of one pulsation is shown in Figure 3a. Figure 3b shows the four cycles of the field angle of the first ring as a function of time. The self-defocusing of light beams is the consequence of the self-modulation of the

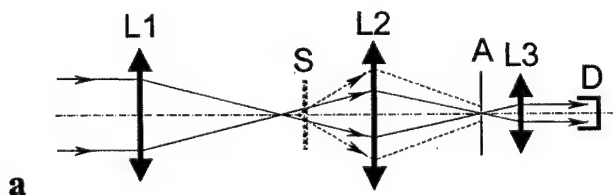




**Figure 3** (a). a sequence of the near field patterns variation. Parallel 780nm light with intensity of  $2.87 \text{ W/cm}^2$  irradiated on the sample of molecule **b** with a spot size of diameter of  $850\mu\text{m}$  and incident angle of  $43^\circ$ . The patterns were projected on a screen that placed 151mm away after sample. The numbers underneath each spot is the time that we start to count. (b). time-dependence of field angle of the first bright ring for the first four pulsation.

refractive index by the optical field via the non-local photorefractive effect. The external field aligns the dipolar molecules in the direction of film normal. The photoexcited mobile electrons diffuse and drift downward along the intensity gradient to the outside of the beam spot, and form a space-charge field pointing radially outward. This space-charge field can make the molecule re-oriented in the radial axis and change the refractive index accordingly. The on-axis index remains a minimum and a doughnut shape index distribution is formed. The beam is thus defocused due to diffraction by the light-induced index ring. If the phase difference between the center portion and the wing portion of the beam is about  $2\pi$ , the first intensity ring appears. A rough estimation gives the index modulation at the first ring,  $\Delta n_1 = \lambda \cos \theta / d$ , where  $d$  the thickness of the film, and  $\theta$  is the inner angle of the beam with respect to the film normal. The two rings that we observed are corresponding to a refractive index modulation,  $\Delta n \sim 0.0093$ . Since the field component perpendicular to the beam favors the charged carrier drift along one direction because of the tilted geometry, and the near-field pattern is elliptic (Figure 3a). As the applied field increases, the formation of the index ring becomes faster and the ring size becomes larger because the photorefractive index modulation is enhanced by the applied field (Figure 2c). The maximum size of the ring is reached when the charge separation and recombination reach equilibrium. If the field is high enough (about  $91 \text{ V}/\mu\text{m}$  in this condition), the index ring can grow quickly into a large size. This, in turn, defocuses the light and lowers the light intensity in the beam spot of the sample. The density of photogenerated electron was reduced and the equilibrium was broken. A sudden disappearance of the space-charge field occurs, and dipolar molecules flip back to the direction of external field. The transmitted light suddenly returns back to its original distribution and then another round of periodical pulsation starts. It can be seen that this instability has limited the gain coefficient. The maximum gain coefficient of a sample of molecule **b** shown in Figure 2b was achieved at lower field before the unstable threshold.

The large self-defocusing effect suggests interesting applications as the self-focusing, self-trapping and spatial soliton wave under the designated conditions.<sup>13,14</sup> Optical switching, optical limiting and transverse optical bistability<sup>15</sup> can also be accomplished. Figure 4 demonstrates preliminary results on the optical limiting, carried out with the experimental set-up





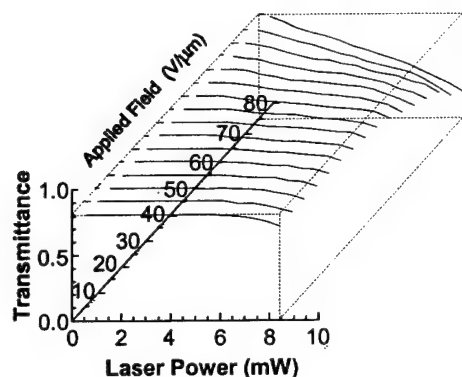


**Figure 4** (a). a set-up for the demonstration of optical limiting performance on the sample of molecule **b** with a CW diode laser at wavelength of 780nm. L1 to L3 are positive lenses, S is sample that is the same as photorefractive experiment. A is an aperture and D is photodiode detector. (b). The transmittance, which defined as the power ratio of the incident light with the detected but excluding the loss of optics and the reflection from the sample interfaces, as function of applied field and the incident light intensity.

shown in Figure 4a. The sample was placed a little bit after the focal point of lens L1. Lenses L2, L3 and aperture A form a spatial filter. The size of the aperture was adjusted to ensure 90% transmission of the small signal under a zero external field. As the external field applied and/or the light intensity increased, the light beam was defocused into the larger field angles (as shown by the dashed lines) and was blocked by the aperture. The transmittance of the device at high intensity decreases with the incident intensity. Figure 4b shows the transmittance as the functions of light intensity and the applied field. The small signal transmittance in the film of 130 $\mu$ m thick without applied field is 92% (after excluding the 5% average reflection at the inter-faces of the ITO glasses with sample and air). The transmitted laser power at a fixed applied field deviated from the small signal transmittance line (83%) and became leveled off. The higher the applied field, the lower the transmitted power. The transmitted power lowered even more with the increase of the input light at a high-applied field. These kinds of optical limiting devices exhibit a large response to continuous wave lasers in the power range of milliwatt to microwatt, and even to nanowatt. The response wavelengths are in near IR range, and can be extended into the infrared region, which is the wavelength region of semiconductor lasers. The desired transmitted light intensity is adjustable by applying a suitable external field. Since the semiconductor lasers have found a wide application in the telecommunication and biological technologies, this kind of optical limiting devices can be used to protect the human eyes and fragile detectors<sup>16</sup>.

In conclusion, rationally designed, simple methine dyes can form amorphous materials, which exhibit an efficient photorefractive performance rivalry with the best polymeric or inorganic materials. These single-molecular materials are easy to be synthesized and processed. Delicate formulation and tedious syntheses are not required. Interesting phenomenon, such as self-defocusing and optical limiting, were observed in these materials. Applications based on these materials and effects can be expected.

conductivity, and electric current density must be accurately described by the species conservation equations. In the present approach, the species continuity equation for a three-component plasma model is based on the drift-diffusion theory. The present formulation, the instantaneous species concentration is calculated by the dynamic balance in a control volume from the contributions directly from the charge particle mobility, flux densities and ionization and recombination processes.

$$\begin{aligned}\frac{\partial n_e}{\partial t} + \nabla \cdot \Gamma_e &= \alpha |\Gamma_e| - \beta n_e n_+ \\ \frac{\partial n_+}{\partial t} + \nabla \cdot \Gamma_+ &= \alpha |\Gamma_+| - \beta n_e n_+\end{aligned}$$

where

$$\begin{aligned}\Gamma_e &= -D_e \nabla n_e - n_e \mu_e E \\ \Gamma_+ &= -D_+ \nabla n_+ - n_+ \mu_+ E\end{aligned}$$

The above differential system contains a total of eight dependent variables and 5 explicit constitutive relations. In a stationary frame of reference, this set boundary conditions degenerate to the familiar relationships that the tangential components of electric field strength  $E$ , and the normal components of magnetic flux density  $B$ , are continuous across the boundary. The discontinuity of the tangential components of magnetic field strength  $H$  is equal to the surface current density  $J$ . Finally the surface charge density  $\rho$ , balances the difference between normal components of the electrical displacement  $D$ , across the interface.

Two distinct numerical procedures were developed in the present research program. For preliminary formulation to model a previously unknown and uncertain physics, the reliable temporally fourth-order and spatially third-order accurate MUSCL scheme was used. After a complete validation process, the system of governing equations was solved by the spectral-like, high-resolution scheme with high-order, low-pass filter to suppress the parasitic spurious Fourier components contained in the numerical solution.

The first accomplishment of the present effort is documented for the fact that when a plasma field surround an object, the global refracting and dispersing property of a microwave can be dramatically altered. The charged particle number density of the plasma determines the plasma frequency, in turn, controlling the attenuation of the incident microwave that is emitted by a wave generator such as the radar transmitter. The reflected electromagnetic energy in the far field from the scattering object can be completely suppressed when the plasma frequency matches perfectly with the incident microwave.

The comparison of the scattered electrical field from a perfect electrically conducting (PEC) sphere in a free space and amid a plasma field is depicted in Figure 1. The numerical result is generated on a (73×60×96) mesh system and used the characteristic-based formulation. The incident microwave is propagated along the Z-axis at a frequency of 256 mHz. On the left hand side of the composite graph, the electric intensity in the free space is presented. On the right hand side of the graph, the counter part in a plasma

medium is given and the electric conductivity is computed based on an electron number density of  $10^{12}$  per cubic centimeter and an electron temperature of 10,000 K. In the scattered variable formulation, the microwave scatterer appears as a transmitter. The reflected electromagnetic wave is almost completely attenuated in the plasma medium; only wave fringes adjacent to the scatterer are barely visible. According to theory, the microwave, when propagating in plasma, will exhibit a frequency shift. For the first time, the phase shift of the electric field intensity in a reflected microwave in plasma is correctly simulated.

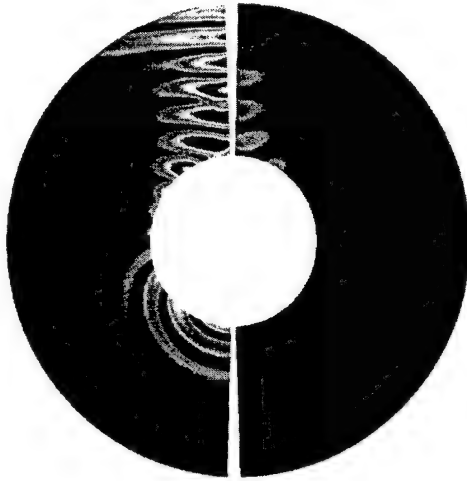


Figure 1. The scattered electromagnetic wave in free space and plasma

The comparison of the computed results in free space and in plasma is presented in Figure 2. The bistatic radar cross-sections (RCS) in a horizontal polarity are measured in dB per wavelength square (dBsw). In plasma this value reduces by a factor of 2.47 over most the viewing angles in comparison with the value in a free space.

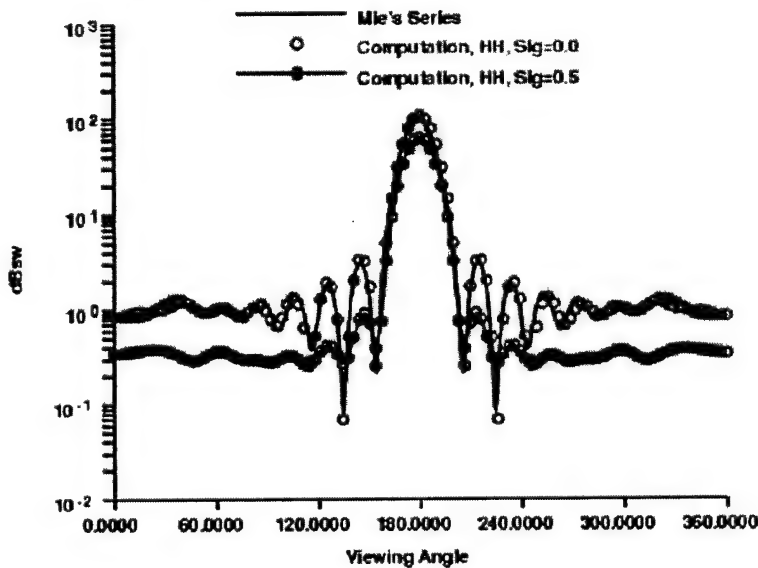


Figure 2. Bistatic RCS in free space and Plasma, HH Polarity

The identical comparison of the bistatic RCS now is given in the polar coordinate of the viewing angles. In this presentation, the significant RCS reduction is easily appreciated. Equally important, the most pronounced signature suppression takes place in the main loop of the observable pattern.

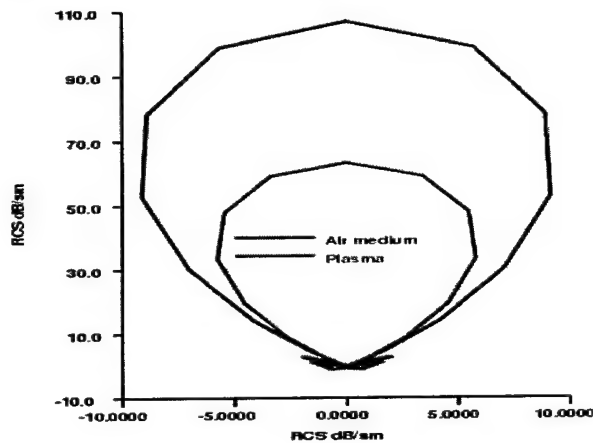


Figure 3. Comparison of bistatic RCSs in polar coordinate of viewing angles

The present research in electromagnetic wave scattering simulation has shown when the incident microwave frequency approaches that of the plasma frequency; the reflected wave is substantially suppressed. This result strongly suggests that a few strategically placed plasma generators at dominant reflection points of a electric object can become an effective active RCS suppression mechanism.

The second accomplishment is in the development of plasma diagnostic capability. In spite of the over thirty years of effort in determining the transport property of plasma for hypersonic and propulsion application, the non-intrusive microwave absorption still has an uncertain band of one order-of-magnitude. The fundamental difficulty arises from complications of the interlocking wave movement as it moves from one control device to another. The microwave system includes the transverse microwave transmission in waveguide, wave columniation by pyramidal horn, the wave reflection at the media interface, and finally, the microwave energy absorption by a non-uniform moving plasma field. The theoretic base for microwave propagation through a media interface and the attenuation in a lossy medium has been established. The ability of accurately simulating the wave pattern in waveguide and especially in pyramidal horn is accomplished by the present effort.

Figure 4 presents the comparison of the magnitude of the Poyting vector in a rectangular waveguide. In the electromagnetic field, this quantity measures the rate of energy flow per unit area at that point and the direction of energy flux is perpendicular to both the electric and magnetic intensity. For the transverse electrical wave  $TE_{1,1}$ , three different mesh systems were used, and the numerical results are essentially grid independent solving by the high-resolution scheme. The numerical results are validated by the theoretical expression derived by the present effort. Over a range of the parameters  $\sigma/\omega\epsilon$ ,

from the value of 0.0 (free-space) to 0.10 (weakly ionized gas), an excellent agreement is reached between the numerical and theoretical results.

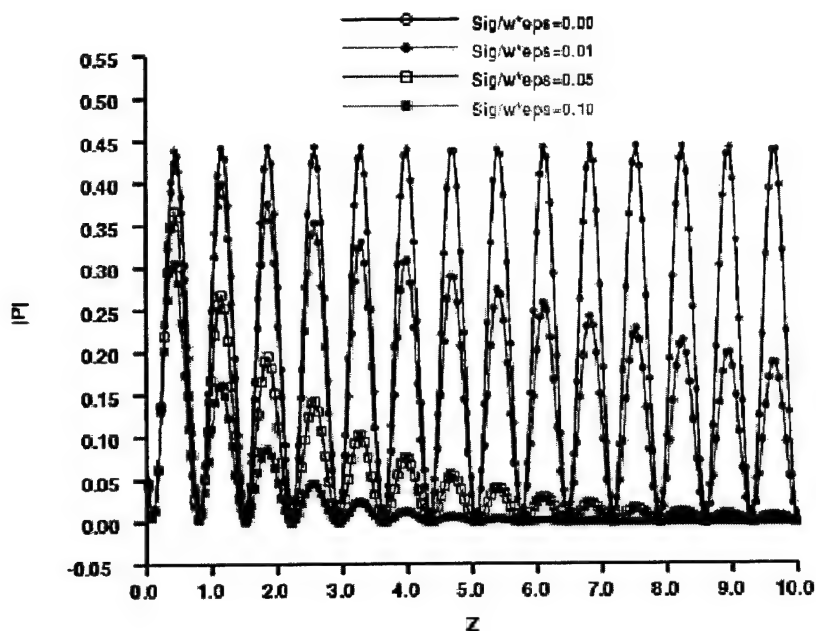


Figure 4. Wave guide simulations validation,  $TE_{1,1}$  waves

A key component for the microwave absorption measurement is the pyramidal horn or the microwave antenna. In Figure 5, only the upper and lower wall of the antenna is given. The electrical field intensity on the surface is depicted, the image on the upper wall describes an attenuating wave pattern and on the lower wall the microwave without any attenuation is recorded.

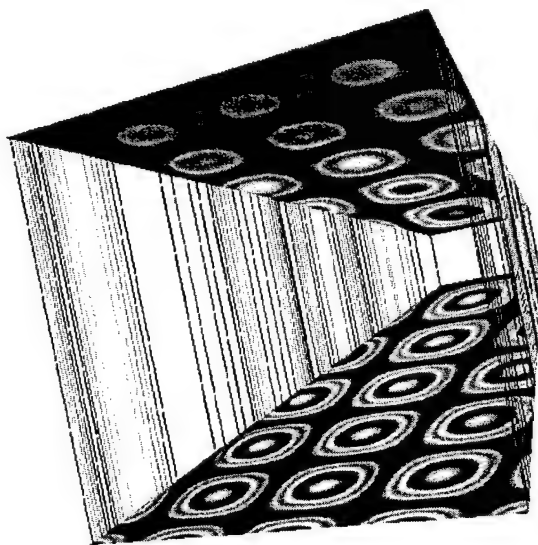


Figure 5. Wave patterns of electrical transverse wave in antenna

The comparison of and theoretical and numerical results of the present research is given in Figure 6. An excellent agreement is observed, the electromagnetic wave in the  $TE_{0,1}$  mode was computed on a  $(73 \times 25 \times 71)$  mesh system. In the present effort only the transverse electric wave was computed, because this wave has the lowest cutoff frequency of any other higher order mode.

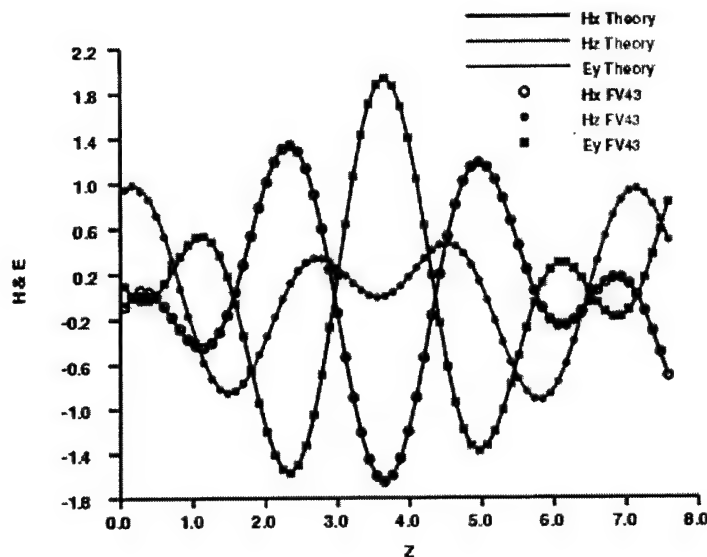


Figure 6. Validating the  $TE_{0,1}$  wave in a pyramidal horn

A third accomplishment in the present effort is the introduction of drift-diffusion theory for glow discharge modeling. This modeling and simulation effort removes the pacing uncertainty for a large group of magneto-aerodynamic computations for hypersonic flow control. Substantial progress has been made as an integrated simulation capability development and provided direct support to the magneto-aerodynamic experimental program at AFRL/VA.

In the coming year, research efforts will concentrate in expanding the application envelope. The validating process will also be sustained via strong coupling with research personnel of the AFRL/VA and AFRL/PR. The simulation capability for plasma transport property, microwave propagation beyond waveguide and antenna will be integrated as a comprehensive computational procedure for plasma diagnostic. This developed and validated modeling simulation tool will be implemented to assess innovative magneto-aerodynamic interaction for high-speed flow control.

Effort will also be exerted to improve substantially the computational efficiency. The Poisson solver for maintaining a consistent electric field was identified as a pacing item for computational magneto-aerodynamics. A high-resolution algorithm based on the alternative direction implicit scheme is anticipated to achieve 25% reduction of data processing rate for the time-dependent, three-dimensional computer program.

The research team published a total of 20 articles on weakly ionized gas and related field during the reporting period. Six of the reported efforts have been released as journal



articles. Meanwhile, interactions have been sustained with the research teams of Dr. D. Gaitonde and Dr. R. Kimmel, as well as, technical consultation provided to Dr. D. Paul and T. Schumacher of AFRL/VA respectively.

#### **Personnel Supported:**

<u>Name</u>	<u>Degree</u>	<u>Discipline</u>	<u>Involvement</u>
Shang, J.S.	PhD	Aerodynamics	75%
Hollenbaugh, Sheila	M.Sc.	Computing Science	5%
Updike, Greg	PhD Candidate	Mechanical Engineering	100%
Surzhikov, Sergey	PhD, D.Sc.	Computational Physics	17%

#### **Publications:**

1. "Spike-tipped Blunt Body in Weakly ionized Hypersonic Stream", J.S. Shang, J.A. Menart, and J.R. Hayes, AIAA 2002-2167, 33<sup>rd</sup> Plasmadynamics and Lasers Conference, Maui HA, 20-23 May 2002.
2. "Plasma Injection for Hypersonic Blunt -Body Drag Reduction", J.S. Shang, AIAA J., Vol. 40, No.6, June 2002, pp. 1178-1186.
3. "Hypersonic Flow Over a Blunt Body with Plasma Injection", J.S. Shang, J.R. Hayes, and J. Menart, J. Spacecraft and Rockets Vol. 39, No. 3, May-June 2002, pp. 367-375.
4. "Computational Electromagnetics", J.S. Shang, Sourcebook of Parallel Computing, Morgan Kaufmann Publishers, Nov. 2002, pp. 224-228.
5. "A Scalable HPF Implementation of a Finite-Volume Computational Electromagnetic Application on a Cray T3E Parallel System", Y. Pan, J.S. Shang, and M. Guo, E-journal Performance Evaluation and Modelling for Computer Systems, 18, 2002, pp. 1-24.
6. "Simulating Microwave Dispersion in Weakly Ionized Air", J.S. Shang, AIAA 2003-0134, 41<sup>st</sup> Aerospace Science Meeting, Reno NV, 6-9 January 2003.
7. "Data Reduction Analysis for Cylindrical, Double Langmuir Probes Operating in Collisionless to Collisional, Quiescent Plasmas", J. Menart and J. Shang, AIAA 2003-0136, 41<sup>st</sup> Aerospace Science Meeting, Reno NV, 6-9 January 2003.
8. "Performance of a Low-Density Hypersonic Magneto-Aerodynamic Facility", J.S. Shang, R. Kimmel, J. Hayes, and Charles Tyler, AIAA 2003-0329, 41<sup>st</sup> Aerospace Science Meeting, Reno NV, 6-9 January 2003.
9. "Glow Discharge in Magnetic Field", Sergey T. Surzhikov and J.S. Shang, AIAA 2003-1054, 41<sup>st</sup> Aerospace Science Meeting, Reno NV, 6-9 January 2003.
10. "Survey of Plasma Generated in a Mach 5 Wind Tunnel", J. Menart, J. S. Shang, S. Henderson, A. Kurpik, R. Kimmel, and J. Hayes, AIAA 2003-1194, 41<sup>st</sup> Aerospace Science Meeting, Reno NV, 6-9 January 2003.

11. "Shared Knowledge in Computational Fluid Dynamics, Electromagnetics, and Magneto-Aerodynamics", J.S. Shang, Progress in Aerospace Sciences Vol. 38, No. 6-7, 2002, pp. 449-467.
12. "Blunt Body in Hypersonic Electromagnetic Flow Field", J.S. Shang, J. Hayes, J., Menart, and J. Miller, J. of Aircraft, Vol. 40, No. 2, 2003, pp. 314-322.
13. "A Scalable HPF Implementation of a Finite-Volume Computational Electromagnetics Application on a CRAY T3E Parallel System", Y. Pan, J.S. Shang, and M. Guo, Concurrency and Computation: Practice and Experience, Vol.15, No. 6, 2003, pp. 607-621.
14. "Computational Electromagnetics for Microwave Attenuation in Weakly Ionized Air", J. S. Shang, AIAA 2003-3621, 34<sup>th</sup> Plasmadynamics and Lasers Conference, Orlando, FL, 23-26 June 2003.
15. "Supersonic Internal Flows with Gas Discharged and External Magnetic Field", S. Surzhikov and J.S. Shang, AIAA 2003-3625, 34<sup>th</sup> Plasmadynamics and Lasers Conference, Orlando, FL, 23-26 June 2003.
16. "Glow Discharge in Magnetic Field with Heating of Neutral Gas", S. Surzhikov and J.S. Shang, AIAA 2003-3654, 34<sup>th</sup> Plasmadynamics and Lasers Conference, Orlando, FL, 23-26 June 2003.
17. "Technique for Making Microwave Absorption Measurements in a Thin Plasma Discharge", A. Kurpik, J. Menart, J. Shang, R. Kimmel, and J. Hayes, AIAA 2003-3748, 34<sup>th</sup> Plasmadynamics and Lasers Conference, Orlando, FL, 23-26 June 2003.
18. "Numerical Simulation of Subsonic Gas Flows with Glow Discharge and Magnetic Field", S. Surzhikov and J. Shang, AIAA 2003-3759, 34<sup>th</sup> Plasmadynamics and Lasers Conference, Orlando, FL, 23-26 June 2003.
19. "Measurements of a Transverse DC Discharge in a Mach 5 Flow", R. Kimmel, J. Hayes, J. Menart, J. Shang, S. Henderson, and A. Kurpik, AIAA 2003-3855, 34<sup>th</sup> Plasmadynamics and Lasers Conference, Orlando, FL, 23-26 June 2003.
20. "Effects of Magnetic Fields on Plasmas Generated in a Mach 5 Wind Tunnel", J. Menart, J. Shang, R. Kimmel, and J. Hayes, AIAA 2003-4165, 34<sup>th</sup> Plasmadynamics and Lasers Conference, Orlando, FL, 23-26 June 2003.

#### **Interactions/Transitions:**

The present effort maintains a very strong interaction with the development of a new Mach 5 low-density plasma tunnel in the Air Vehicles Directorate, Air Force Research Laboratory. In fact, the plasma diagnostic tool development at AFRL leads the nation. Today, the high-speed plasma channel of Air Vehicles Directorate has the Langmuir

probes, microwave absorption measuring system, spectral based diagnostic tools for both the temperatures of internal degree of freedom and plasma transport property. In addition, the concept of electromagnetic actuator for hypersonic flow control has been provided to AFRL/VA, and preliminary experimental data have revealed a promising first-order effect. The interactions with scientific research community have also extended to reach a large sector of aerospace community; collaborating scientists of the present efforts are

Dr. D. Gaitonde, AFRL/VA  
Dr. R. Kimmel, AFRL/VA  
Prof. R. MacCormack, Stanford University  
Prof. D. Gottlieb, Brown University  
Prof. W. Rich, Ohio State University  
Prof. I. Adamovich, Ohio State University  
Prof. W. Bailey, Air Force Institute of Technology  
Prof. J. Menart, Wright State University  
Prof. S.T. Surzhikov, Russian Academy of Science  
Prof. Yu. Kolesnichenko, Russian Academy of Science

#### **Invited Lectures, Presentations, Talks, etc.:**

J. Shang:

- \* 33<sup>rd</sup> AIAA Plasma Dynamics & Laser Conference, 14<sup>th</sup> International Conference on MHD Power Generation and High Temperature Technologies, May 2002
- \* 41<sup>st</sup> AIAA Aerospace Science Meeting, January 2003
- \* Invited Speaker, 6<sup>th</sup> International Nobeyama workshop on the New Century of computing in Fluid Dynamics, April 2003
- \* 34<sup>th</sup> Plasma Dynamics & Laser Conference, June 2003
- \* Keynote Speaker, 4<sup>th</sup> ASME/JSME Joint Fluid Engineering Conference, July 2003
- \* Invited Speaker, 2003 AFOSR Workshop on Advances and Challenges in Time-Integration of PDE's, Brown University, August 2002

#### **Consultative and Advisory Functions:**

The principal investigator of the research project is retained by the AFRL as an emeritus scientist to rejuvenate the aerodynamic experimental programs. He also continued his role as the Chairman of the AIAA Plasmadynamics and Laser Technical Committee until April 2003.

#### **Transitions:**

The newly acquired knowledge in plasmadynamics and developed new simulation capability has been shared with the AFOSR tasks of Computational Hypersonics (2307N403 and 2307N617) and Computational Electromagnetics (2307N400). In specific, the technique of drift-diffusion theory for computing plasma transport property has been introduced to basic research team in AFRL/VAAC. The concept of electromagnetic actuator for hypersonic flow control and its experimental set-up have also been provided to the Mach 5 low-density plasma channel AFRL/VAAA. The electromagnetic actuator built on the principle magneto-aerodynamic interaction indicates break through potential for a wide range flight regimes.

The computer program after fully validated and additional numerical efficiency improvement will transfer to Air Vehicles and Sensor Directorates, Air Force Research Laboratory for possible support to the Uncooperated Signature Identification Program. The dual use applications in plasma diagnostic will also be further developed with universities and aerospace industries.

**New Discoveries, Inventions, or Patent Disclosures:**

The electromagnetic actuator is implemented as embedded electrodes adjacent to the sharp leading edge of a plate. The Joule heating and Lorentz force substantially modify the displacement thickness of the boundary layer with a minute amount of electric energy input (50 mA at 1 kV). Meanwhile the ensuing viscous-inviscid interaction in hypersonic speed substantially accentuates the resultant aerodynamic force. This added physical dimension can be harnessed as flight control mechanism without any moving parts.

**Honor/Awards:**

General Foulois Award, 1979,1985  
Outstanding Scientist/Engineer of Dayton, 1980  
USAF Primus Award, 1983  
USAF Basic Research Award, 1986  
Distinguished Alumnus Award of the Ohio State University, 1992  
Fellow of AIAA, 1993  
Meritorious Civilian Service Award, 1998  
Outstanding Civilian Service Awards, 2001  
Exception Civilian Service Award, 2001  
AIAA Sustained Service Award, 2002